Experimental Measurement of Turbulent Burning Velocity of Premixed Biogas Flame

by

Ahmad Ayache

A Thesis submitted to the faculty of graduate studies of

The University of Manitoba

in partial fulfilment of the requirements of the degree of

MASTER OF SCIENCE

Department of Mechanical Engineering

University of Manitoba

Winnipeg

ABSTRACT

Biogas is a renewable source of energy produced by anaerobic digestion of organic material, and composed mainly of methane (CH_4) and carbon dioxide (CO_2). Despite its lower heating value, biogas can replace fossil fuels for applications such as stationary internal combustion engine, stationary gas turbine and industrial burners. However, comprehensive experimental data of the turbulent burning velocity of biogas (S_t), which is a fundamental property for optimizing combustion applications and validating numerical codes, is still lacking. Therefore, the present study is dedicated to experimentally determine the biogas turbulent burning velocity under normal temperature and pressure conditions. In this study, three different biogas surrogate compositions are investigated. Turbulent premixed biogas flame is centrally ignited in a 29 L fan-stirred spherical combustion chamber of nearly homogeneous and isotropic turbulence with an intensity, u', varying between 0.5 and 1.5 m/s. Outwardly propagating biogas flame is tracked and imaged using Schlieren imaging technique via a high-speed camera, and S_t values are obtained by measuring the flame front area using an in-house developed Matlab code. To verify the experimental methodology, turbulent burning velocity of methane-air mixture is determined and compared with published data. Biogas results show that by increasing turbulence and reducing CH_4%, biogas-air flammability limit reduces from $0.6<\emptyset<1.2$ to $0.7<\emptyset<1.1$. Additionally, the curve fits of the turbulent burning velocity versus the equivalence ratio show two different trends. At fixed u', when more CH_4 is added into the mixture, the peak of the turbulent burning velocity (50 cm/s) shifts away from the nearly-lean equivalence ratio towards the stoichiometric one. On the contrary, when u' is increased from 0.5 to 1.5 for the same biogas compositions, the peak of the turbulent burning velocity shifts away from the stoichiometric equivalence ratio towards the leaner one.

ACKNOWLEDGMENTS

I wish to greatly thank my supervisor Dr. Madjid Birouk for providing me assistance, guidance, and knowledge during my graduate program. I would also acknowledge the financial support received from the University of Manitoba, the Province of Manitoba, and the National Sciences and Engineering Research Council of Canada (NSERC). Additionally, special thanks go to the laboratory technical staff, especially S. Karnaoukh, who provided me with technical guidance and support, and fellow graduate students, Carlos Alberto Gomez Casanova, Cameron Verwey, and Mahmoud Moussa Abdel Azim, for their help and assistance. Finally, I want to express my sincere appreciation to my family, especially my parents, who have always been a provision.

TABLE OF CONTENTS

LIST OF FIGURES

LIST OF TABLES

NOMENCLATURE

A_T	turbulent flame front area [mm^2]
A_0	laminar flame front area [mm^2]
C_p	specific heat capacity at constant pressure [J/k.Kg]
Da	Damkohler number [-]
K	stretch rate [s^{-1}]
Ka	Karlovitz number [-]
L	integral length scale [mm]
L_b	Markstein length [cm]
l_δ	inner layer thickness [mm]
m_f	mass of fuel [kg]
m_a	mass of air [kg]
m_{uo}	mass of the unburned gases outside R_j [kg]
m_{ui}	mass of the unburned gases inside R_j [kg]
m_{bi}	mass of the burned gases inside R_j [kg]
m_{bo}	mass of the burned gases outside R_j [kg]
N	rotational fan speed [RPM]
n	number of moles [mole]
N_i	number of moles of the fuel components [mole]
N_m	number of moles of the mixture [mole]
N_f	number of moles of the fuel [mole]
N_{air}	number of moles of air [mole]
P	pressure [psi]
P_m	mixture partial pressure [psi]
P_i	fuel partial pressure [psi]

r	radius value, reference value [mm]
R	radius [mm]
R_r	root radius [mm]
R_t	tip radius [mm]
R_j	average radius [mm]
R_{Sch}	Schlieren radius [mm]
Re	Reynolds number [-]
Re_L	integral length scale Reynolds number [-]
S_b^o	Non-stretched laminar flame speed [cm/s]
S_b	stretched laminar flame speed [cm/s]
S_t	turbulent burning velocity
S_L	laminar burning velocity [cm/s]
t	time lapse [ms]
t_T	turbulent time scale [ms]
t_c	chemical time scale [ms]
T	temperature [K]
T_u	unburnt gas temperature [K]
T_i	ignition temperature [K]
T_b	burnt gas temperature [K]
T_m	fuel mixture temperature [K]
u	horizontal velocity fluctuations [m/s]
u_{trj}	mass turbulent burning velocity [cm/s]
u_{tr}	turbulent burning velocity [cm/s]
u'	turbulence intensity [m/s]
$\overline{U}$	horizontal mean velocity [m/s]

U_{rms}	horizontal root mean square velocity [cm/s]
$\bar{V}$	vertical mean velocity [m/s]
v	vertical velocity fluctuations [m/s]
V_m	fuel mixture volume [m^3]
V_{rms}	vertical root mean square velocity [cm/s]
V_{ui}	volume of the unburnt gases inside the flame sphere [m^3]
V_{bo}	volume of the burnt gases outside the flame sphere [m^3]
W_f	molecular weight of fuel [kg/mole]
W_{air}	molecular weight of air [kg/mole]
W_o	molecular weight of Oxygen [kg/mole]
W_N	molecular weight of Nitrogen [kg/mole]
W_{rms}	third direction root mean square velocity [cm/s]
x	horizontal direction [-]
y	vertical direction [-]

Greek Symbols

δ_f	flame Thickness [mm]
v^r	radial velocity [cm/s]
ρ_b	burnt gases density ratio [Kg/m^3]
ρ_u	unburnt gases density ratio [Kg/m^3]
λ	Taylor length scale [mm]
ξ or η	Kolmogorov length scale [mm]
λ	thermal conductivity [W/mK]
ϕ	equivalence ratio [-]
α	number of moles of Carbon [mole]

β	number of moles of Hydrogen [mole]
γ	number of moles of oxygen

Acronyms

fps	frames per second
RPM	revolution per minute
PIV	particle imaging velocimetry
LDV	laser Doppler velocimetry
psia	absolute pressure in pounds per square inch
gsia	gauge pressure in pounds per square inch
Sch	Schlieren
rms	root mean square
avg	average

CHAPTER 1 - INTRODUCTION

Increasing concerns about global warming due to greenhouse gases and pollutant emissions have raised awareness towards developing more friendly energy sources that can substitute fossil fuels [1]. Moreover, the rise in human population has consequently boosted fossil fuel consumption due to the increasing demand for transportations and heating applications. This increase in demand does not only increase the emissions of the fossil fuels which endanger the existence of a healthy green environment, but also leads to an increase in energy price [1]. Thus, alternative sources of energy that can produce fewer pollutant emissions at affordable prices should be explored and developed to limit the reliance on fossil fuels [2]. As such, renewable energy sources based on solar, wind and geothermal can play a vital role in replacing fossil fuels as they produce clean energy with zero pollutant emissions [3]. However, although these energy sources are naturally available and widely accessible, their development cost is still relatively expensive in comparison to fossil fuel [4]. Nonetheless, a lot of progress has been made to develop biofuels, such as biogas (composed mainly of CH_4 and CO_2), as a replacement of fossil fuel in several applications [5].

Biogas is produced by anaerobic digestion of organic material found in feedstocks such as agricultural waste, manure, municipal waste and food waste [6]. With methane as a major component (in the range 50-70%), biogas also comprise a large amount of carbon dioxide (50-30%) with small traces of ammonia (0.1-0.5%), nitrogen (0.5-2.5%), and hydrogen sulphide (0.1-0.5%) depending on the source [7]. Thus, despite its lower calorific energy due to the presence of high CO_2 concentrations, the ability of biogas to generate energy with least amount of

pollutants and NO_x emissions has made it one of the most desirable candidates to replace fossil fuels in several combustion applications [7,8]. For instance, biogas can operate light-load applications such as hot water boilers, forced-air furnaces, and direct-fired room heaters [9]. On the other hand, it can also be used as an alternative engine fuel for heavy-load applications such as spark-ignition internal combustion engines, compression-ignition engines with the aid of pilot fuels [10–12], and also for stationary gas turbines [13].

A better understanding of the combustion processes is crucial for achieving the best engine combustion performance with maximum efficiency [14]. This can be achieved by studying the combustion properties such as flammability, stability, laminar and turbulent burning velocity. Thus, to optimize the combustion of biogas for practical applications, comprehensive knowledge of these characteristics/properties is required. Many experimental and numerical investigations were dedicated to investigating the stability and laminar burning velocity of biogas under a wide range of conditions [5,15–35]. On the other hand, only a few studies were conducted to investigate the biogas turbulent burning velocity [36–40]. As combustion occurs in a turbulent environment in most combustion applications (e.g., internal combustion engine and gas turbine), knowledge of the turbulent biogas flame speed under extensive test conditions is important for the optimization of biogas combustion systems. For instance, knowledge of the turbulent burning velocity is crucial for validating numerical design models employed by the commercial engine manufacturers [41]. Furthermore, turbulent burning velocity is an indication of fuel reactivity, which has a significant influence on engine power output, performance, and pollutant emissions [42]. Thus, to optimize biogas combustion systems, knowledge of biogas turbulent burning velocity over extensive range of test conditions is required.

The present study aims at performing an experimental study to determine biogas turbulent burning velocity for several biogas fuel compositions over a wide range of turbulence intensity and equivalence ratio. In this study, outwardly propagating flames were generated at the centre of a spherical combustion chamber where the turbulent burning velocity was measured by tracking the flame propagation using Schlieren imaging technique via a high-speed camera, under normal temperature (298 K) and pressure (atmospheric) conditions.

This thesis is divided into five chapters as follows. Chapter 1, which introduced the present work by addressing the objectives, motivations, applications, and experimental conditions. Chapter 2 describes the experimental methodologies used in this study as well as some basic definitions and backgrounds related to turbulent burning velocity. Chapter 3 overviews literature pertaining to laminar and turbulent burning velocities under standard and elevated temperature and pressure conditions. In chapter 4, a detailed description of the experimental setup and test conditions is provided, while chapter 5 presents the experimental results and their discussion. Chapter 6 reports a summary of main findings and outlines some suggested recommendations for future work and further improvement in the experimental setup. Finally, samples of raw data tables, MATLAB code, experimental techniques and procedures, error analysis, and tabulated summaries of the equipment are given at the end of this thesis in appendices.

CHAPTER 2 – METHODS FOR DETERMINING FLAME SPEED AND DEFINITIONS

Measuring laminar and turbulent burning velocity is important for validating numerical combustion models and hence enable optimizing combustion systems. Experimental methods for determining this property are described below. Before proceeding with these methodologies, it is necessary first to provide an overview about the definition of laminar and turbulent burning velocities.

2.1 Premixed laminar and turbulent burning velocity - Definition

Premixed flames are generated by igniting a well-mixed fuel and oxidizer. Practical applications of such combustion are spark-ignition engines, lean-burn gas turbines, and household burners. After the fuel and oxidizer homogeneously mix and a heat source is applied, the flame front starts propagating outwardly through the unburned mixture. Depending on flow conditions, flame propagation can either be laminar or turbulent. In practical cases, once the spark is initiated, a laminar flame kernel forms at first then rapidly becomes turbulent as it moves towards the unburned mixture. Therefore, understanding of turbulent burning velocity requires a thorough knowledge of laminar combustion as turbulent flame under certain conditions can be treated as an array of laminar flamelets [43]. The one-dimensional laminar burning velocity is a fundamental physio-chemical combustion property of the fuel-air mixture and depends only on the mixture composition, pressure, and temperature. By definition, laminar burning velocity is "the velocity, relative to and normal to the flame front, with which the unburnt gas moves into

the front and is transformed into products under laminar flow conditions" [44]. Figure 2.1 (a) shows a schematic representation of laminar expanding flame with burnt and unburnt gases separated by the flame front. Figure 2.1 (b) shows the corresponding grey-scale laminar flame. In most cases, outwardly-propagating laminar flame has a spherical structure with some wrinkling. This spherical geometry is maintained by a continuous transformation process of the reactants into products with no turbulence affecting the flame propagation. Instead, flame stretch, wall effect, and ignition energy are the only factors that can significantly affect laminar flame propagation and structure.

Moreover, after the formation of the laminar flame kernel at the early stages of the premixed combustion inside the spark-ignition engine, this kernel develops into a turbulent semi-spherical flame. However, under turbulent flow condition, the flame front wrinkles and develops instabilities due to the turbulent motion and the thermodynamic expansion of gases. Figure 2.2 (a) shows a schematic representation of an expanding turbulent flame with the burnt and unburnt gases separated by the flame front. Figure 2.2 (b) shows the corresponding grey-scale turbulent flame. Similarly to laminar flame, turbulent flame is defined as, "the average rate of flame propagation through a turbulent premixed gas mixture relative to the flow field through the action of molecular diffusion of heat and mass" [45]. Therefore, turbulent flame propagation is initially laminar but affected by turbulent field and scales. Nonetheless, the substantial wrinkling of turbulent flame surface can significantly increase the flame front area, which hence boosts flame propagation speed. Thus, turbulent burning velocity, depending on turbulence intensity, can exceed laminar burning velocity several times under the same experimental conditions.

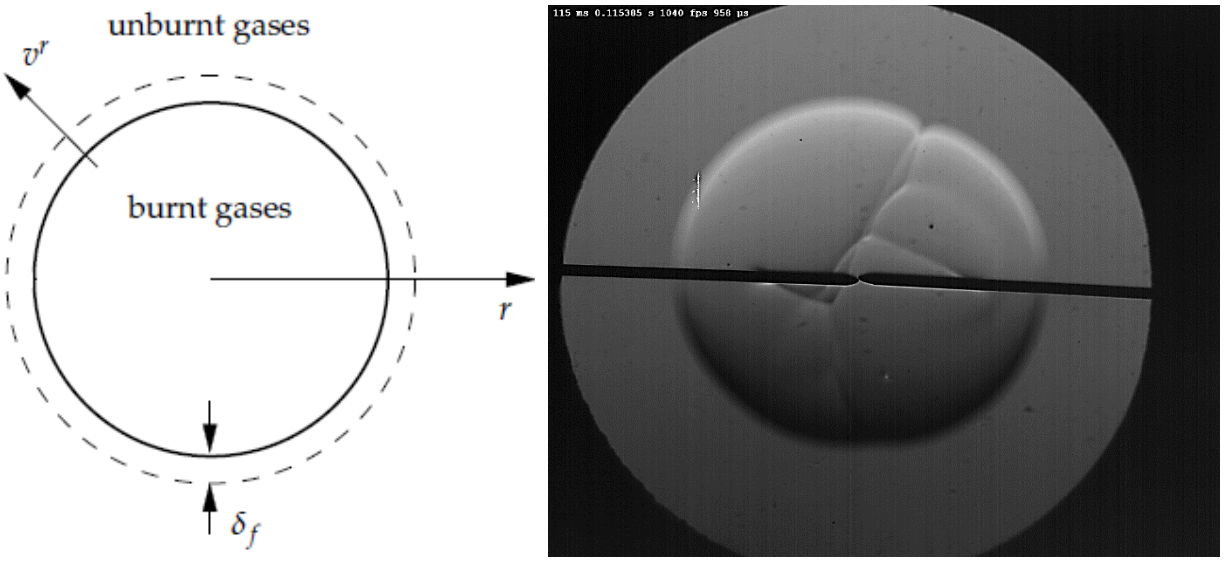

(a) (b)

Figure 2.1. Schematic representation of an expanding laminar premixed flame. The solid line represents reaction layer while the continuous line represents the flame front preheat zone ((a) δ_f and v^r are the flame thickness and radial velocity, respectively, b) Grey-scale laminar flame)

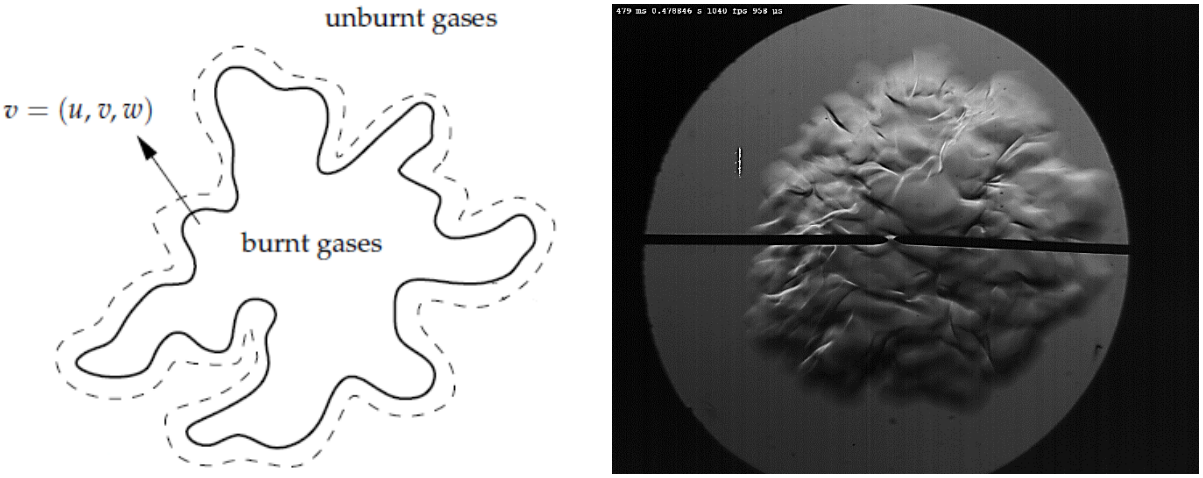

(a) (b)

Figure 2.2. a) Schematic representation of an expanding turbulent premixed flame. a) The solid line represents the reaction layer while the continuous line represents the flame front preheat zone [46]. b) Grey-scale turbulent flame

2.2 Experimental flame configurations and methodologies

Fuel combustion characteristics such as flammability and burning velocity are studied based on five major flame configurations that differ in conditions and structure. These configurations are: outwardly-propagating flames (spherical or cylindrical combustion chamber), conical flames (Bunsen burners), planar flames (planar burner), counter flow jet configuration, and heat flux.

An outwardly-propagating flame (see Fig 2.3 (a)), generated inside a spherical or a cylindrical combustion chamber, is one of the most used configurations in the literature due to its numerous advantages over other flame's configurations. For instance, an outwardly-propagating flame represents realistic conditions of internal combustion engines as it can be generated under elevated temperature and pressure conditions in a constant-volume combustion chamber. Moreover, in a laboratory constant-volume chamber, homogeneous and isotropic turbulence can be generated which allows to develop a homogeneous flame with a spherical geometry. These flames can be visualized by applying several imaging techniques without excessive fuel consumption (e.g., each experiment requires a minimal amount of fuel), while both laminar and turbulent burning velocities can be deduced from the variation of the flame front radius with the time lapse from the onset of ignition. However, despite its vast advantages, this flame configuration has some drawbacks. This includes instabilities and distortions of the flame shape during ignition period and throughout flame propagation, as well as buoyancy and wall effects (especially at high pressures).

Another configuration used in the literature is the planar-shaped flame, which is a straightforward methodology suitable for determining laminar burning velocity by using Laser Doppler Velocimetry (LDV) or Particle Imaging Velocimetry (PIV) without the need to measure the radius evolution or stretch rate (see Fig 2.3 (b)). This methodology is based on the quasi-adiabatic characteristic of flame which eliminates the strain effects and conductive heat loss. Thus, a linear extrapolation can be applied to determine the non-stretched laminar flame speed. However, unlike the outwardly-propagating configuration, this method needs to maintain a steady flow of fuel-air mixture which is very challenging as the planar flames are prone to instabilities. On the other hand, this configuration can hardly operate at high temperatures and pressures, which limits its ability to generate realistic combustion conditions. Moreover, a planar flame (diffusion counter flow flame) can also be obtained by a counter flow burner (see Fig 2.3 (d)). This burner consists of two opposed axisymmetric nozzles by which an oxidizer and a gaseous fuel each flows from an opposed nozzle and form a planar flame embedded between the two potential flows.

Conical-shaped flames (e.g. Bunsen burner, Slot burner, and conical burner, see Fig 2.3 (c)) have also shown to be successful methods for measuring both laminar and turbulent burning velocities due to its simplicity. For instance, this experimental configuration is based on operating a nozzle-type burner with a constant and homogeneous flow of premixed fuel-air mixtures. The imaging technique can track the conical flame shape (using angle method) and hence makes it possible to determine both laminar and turbulent burning velocities. However, this method cannot be used at elevated test conditions.

Moreover, with the least extrapolations or uncertainties, the heat-flux method is a direct measurement of laminar burning velocity at zero-stretch for the one-dimensional planar adiabatic flame (see Fig 2.3 (d)). However, using this method is challenging as the flame should be obtained on the burner plate with a zero-net heat flux due to heat balance between the flame and the plate which can be attained by using a cooling system or perforated plates. Thus, this method is prone to flame instability if a homogeneous fuel-air mixture flow is not well attained.

Nevertheless, with all advantages and disadvantages of the aforementioned experimental configurations, the outwardly-propagating spherical flame, despite its complications, is the most used setup for the measurements of laminar and turbulent burning velocity under realistic test conditions. Therefore, this methodology is adopted in the present study to measure biogas turbulent burning velocity.

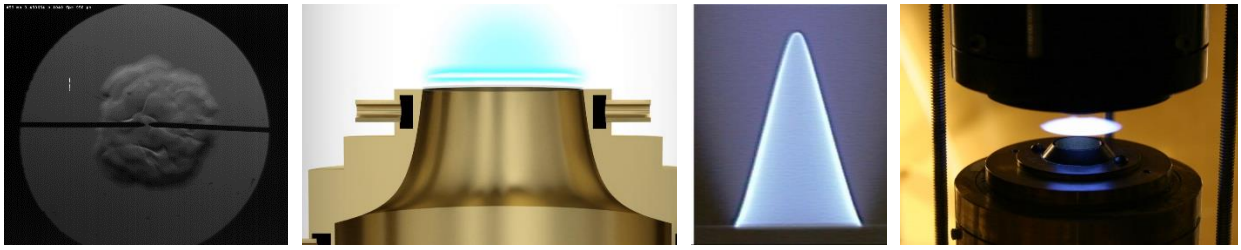

(a) (b) (c) (d)

Figure 2.3. Flames generated from different configurations a) Outwardly-propagating flame b) Planar or Heat Flux flame [47] c) Conical Flame (Bunsen Flame) [48] d) Counter flow Jet configuration [30]

2.3 Outwardly-propagating spherical flames

Measuring laminar and turbulent burning velocity of outwardly-propagating spherical flames in a constant-volume combustion chamber is the most adopted method in the literature [18,19,24,25,34,49]. This popularity of the outwardly-propagating method is because of its accuracy, suitability to produce realistic combustion test conditions under elevated temperatures and pressures, the ability to test fuels at their full flammable range, and the suitability to apply any imaging system due to the chamber's spherical or cylindrical geometry. In this method, the fuel-air mixture is injected into the chamber using a fuel-injection system, and an ignition system is used to start a spark at the centre of the combustion chamber which ignites the fuel and creates an outwardly-propagating flame (Appendix B). The flame propagation speed is measured by applying a Z-type Schlieren optical diagnostic technique (see Fig 2.4) which requires a high-speed camera to capture and track the flame front evolution which can be detected via the density gradient between the burned and the unburned gases. The recognition of the flame front is usually enhanced by using a pinhole or a knife edge which cuts off the dark background light beams and keeps the bright ones. The detected circular edge recorded by a high-speed camera can then be processed to calculate the flame front surface area and consequently the Schlieren flame radius, R_{Sch}, which is then divided by the elapsed time from the ignition start to determine the flame propagation speed dr_{Sch}/dt. Mathematical or empirical formulations are applied to calculate the burning velocity depending on whether the studied flame is laminar or turbulent. A detailed explanation of the Schlieren imaging technique is provided in section 4.6.

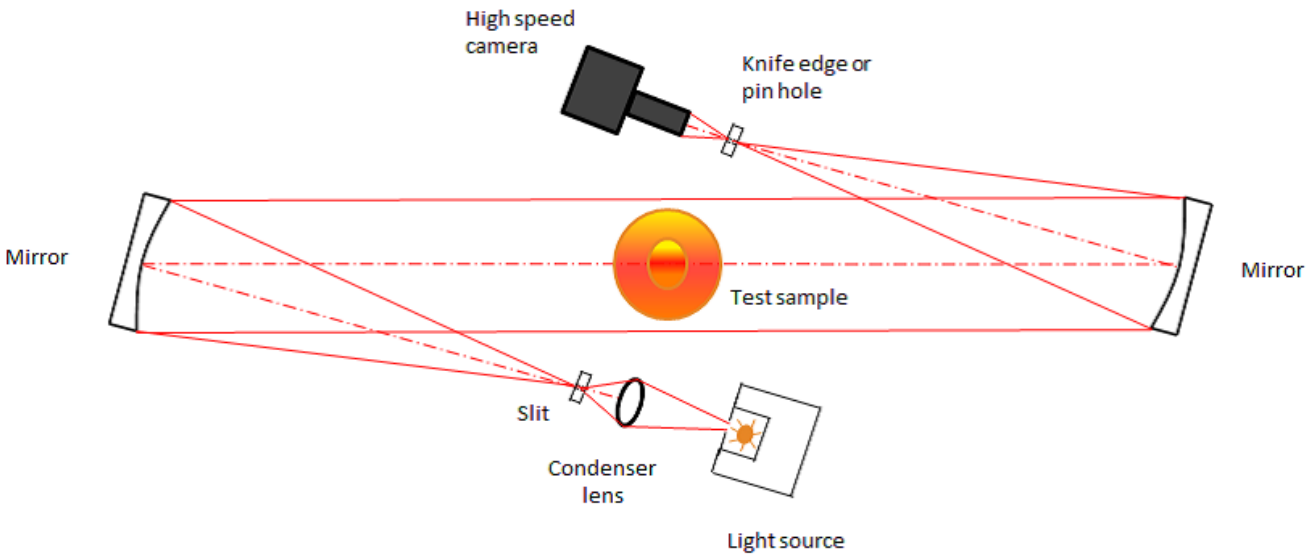

Figure 2.4. Z-type Schlieren arrangement[50]

2.3.1 Laminar burning velocity

Different equations were used to define and calculate laminar burning velocity. Most of these equations are based on the flame propagation speed, $^{dr_{Sch}}/_{dt}$, which is obtained from Schlieren imaging technique or diagnostics. To calculate laminar burning velocity from a constant-volume spherical combustion chamber using Schlieren technique, the stretch rate, K, which characterizes the geometrical expanding effects on the propagation of the flame, is first calculated using the following equation [51]:

$$K = \frac{2}{r_{Sch}} \frac{\partial r_{Sch}}{\partial t} \tag{2.1}$$

Laminar flame speed at zero stretch, S_b^o, is calculated by applying a linear extrapolation (by setting S_b equal zero) of the following equation:

$$S_b = S_b^o - L_b K \tag{2.2}$$

where

L_b: Markstein length, which accounts for thermal effects of the flame

r_{Sch}: spherical flame radius (or Schlieren radius)

S_b^o: non-stretched laminar flame speed

S_b: stretched laminar flame speed (laminar propagation speed, dr_{Sch}/dt)

Laminar burning velocity, S_L, is obtained by multiplying the non-stretched laminar flame speed by the density ratio (see Appendix D) of the burnt and unburnt gases, which is expressed as follows [52]:

$$S_L = \frac{\rho_b}{\rho_u} S_b^o \tag{2.3}$$

2.3.2 Turbulent burning velocity

A universal turbulent burning velocity equation was developed by Bradley et al. [42] using a constant-volume spherical combustion chamber. Experiments were conducted under a uniform and isotropic turbulence at ambient pressure and temperature conditions. Flame imaging and spatial distributions of burnt and unburnt gases were performed and measured via Mie scattering

of tobacco smoke in a thin planar laser sheet, and high-speed Schlieren images were also captured. In their investigation, Bradley et al. [42] assumed that the volume of the unburnt gas (V_{ui}) inside a spherical flame of radius R_j is equal to the volume of the burnt gas (V_{bo}) outside this radius, as indicated in Figure 2.5:

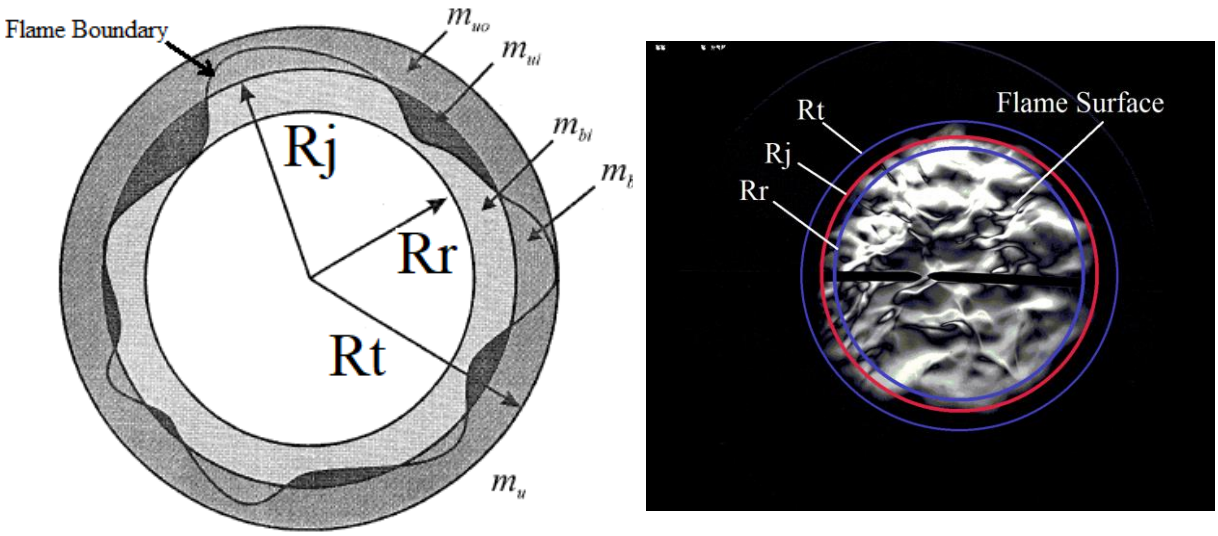

(a) (b)

Figure 2.5. a) Schematic representation of the reference radii and associated masses of burned and unburned gases [42] b) Reference radii of a post-processed turbulent flame

where R_r is the root radius (the smallest radius), R_t is the tip radius (the largest radius, located at the furthest tip of the flame), R_j is the intermediate radius between R_r and R_t, m_{uo} is the mass of the unburned gases outside R_j, m_{ui} is the mass of the unburned gases inside R_j, m_{bi} is the mass of the burned gases inside R_j, and m_{bo} is the mass of the burned gases outside R_j.

Thus, based on the volume assumption ($V_{ui} = V_{bo}$), R_j is equal to the average radius, R_v. By equating the two volumes, a mass conservation is deduced as follows:

$$m_{ui}/\rho_u = m_{bo}/\rho_b \tag{2.4}$$

where ρ_u and ρ_b are the burnt and unburnt gas densities, respectively (see appendix D).

For spherical turbulent flame propagation, the mass rate of burning can be expressed in terms of the spherical surface area $4\pi {R_j}^2$ and the unburned gas density as follows:

$$\frac{d(m_{bi}+ m_{bo})}{dt} = 4\pi {R_j}^2 \rho_u u_{trj} \tag{2.5}$$

where u_{trj} is the mass turbulent burning velocity indicated by the spherical surface area $4\pi {R_j}^2$. The mass burnt within the sphere of radius R_j can be expressed by the product of its volume and density (ρ_b) as:

$$m_{bi} = \left(\frac{4}{3}\pi {R_j}^3 - \frac{m_{ui}}{\rho_u}\right)\rho_b \tag{2.6}$$

Thus, from equations (2.5) and (2.6), we obtain:

$$4\pi {R_j}^2 \rho_u u_{trj} = 4\pi {R_j}^2 \rho_b \frac{dR_j}{dt} - \frac{\rho_b}{\rho_u}\frac{dm_{ui}}{dt} + \frac{dm_{bo}}{dt} \tag{2.7}$$

From the volume assumption, we found:

$$\frac{dm_{ui}}{dt} = \frac{dm_{bo}(\rho_u/\rho_b)}{dt} \tag{2.8}$$

the last two terms of Eq. (2.7) become zero, and hence the turbulent burning velocity at radius R_v is determined as:

$$u_{tr}(R_v) = \frac{\rho_u}{\rho_b}\frac{dR_v}{dt} \tag{2.9}$$

Bradley et al. [42] plotted the turbulent burning velocity obtained from the above equation based on the average radius, R_v, versus turbulent burning velocity calculated by the Schlieren flame radius, as shown in Figure 2.7. Based on the deduced linear relation, a final turbulent burning velocity equation was obtained (Eq. 2.10). The turbulent burning velocity calculated by this equation, either stated by S_t or $u_{tr,}$ is widely used in the literature [53–59]. In this thesis, turbulent burning velocity is expressed as S_t.

$$u_{tr}(R_v) = \left(\frac{1}{1.11}\right)\frac{\rho_b}{\rho_u}\frac{dR_{Sch}}{dt} \tag{2.10}$$

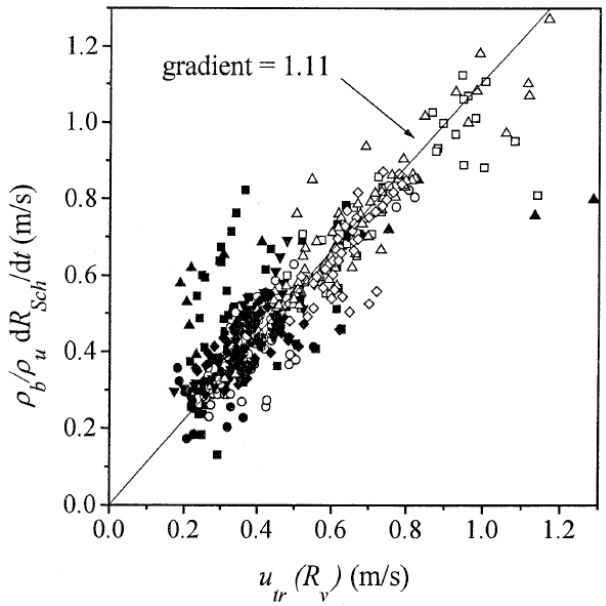

Figure 2.6. Relationship between Schlieren flame radii and turbulent burning velocity $u_{tr}(R_v)$ [42]

2.4 Definitions and background

The objective of this section is to provide a brief background of various parameters and non-dimensional numbers used throughout this thesis such as turbulent length scales, Damköhler number, Karlovitz number, laminar flame thickness, and combustion regimes.

2.4.1 Turbulent length scales

A turbulent flow field contains eddies of different length scales. These eddies transfer energy from the largest scales (integral length scales) to the finest ones (Kolmogorov scales) through the so-called Cascade hypothesis (Fig. 2.8).

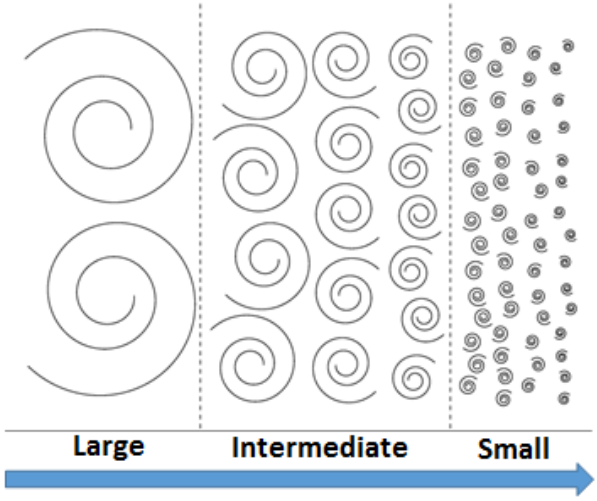

Figure 2.7. Energy Cascade [45]

These scales are defined as follows [60–62]:

2.4.1.1 Integral length scale

It is the largest size eddy in the flow which contains most of the kinetic energy. It is defined as the longest connection or correlation distance between the velocities at two points of the flow field [61]. The integral length scale is calculated by integrating the area under the curve (Eq. 2.11), where the longitudinal and lateral spatial correlation coefficient are, respectively, given by Eqs. 2.13 and 2.14.

$$L = \int_0^\infty f(r)dr \tag{2.11}$$

$$f_x(r) = \frac{\overline{u(x_0,y_0)u(x_0+r,y_0)}}{U_{rms}(x_0,y_0)V_{rms}(x_0+r,y_0)} \tag{2.13}$$

$$f_y(r) = \frac{\overline{v(x_0,y_0)v(x_0,y_0+r)}}{V_{rms}(x_0,y_0)V_{rms}(x_0,y_0+r)} \tag{2.14}$$

2.4.1.2 Taylor length scale (λ)

It is the intermediate scale between the integral length scale and the Kolmogorov length scale (smallest scale). Eddies of this size transfer energy from the large scales to the finest ones. For homogeneous and isotropic turbulence, Taylor microscale λ can be estimated from the longitudinal length scale L and the Reynolds number associated with the integral length scale Re_L [63] as:

$$\frac{\lambda}{L} \sim \sqrt{\frac{15}{Re_L}} \tag{2.15}$$

2.5.1.3 Kolmogorov length scale (ξ)

These scales are the smallest eddies in the flow by which the dissipation of the kinetic energy into heat takes place. Kolmogorov length scale ξ can be estimated from the following relation [61]:

$$\frac{\xi}{L} \sim Re_L^{-3/4} \tag{2.16}$$

2.4.2 Non-dimensional numbers

2.4.2.1 Damköhler number (Da)

Damköhler number, which is defined as the ratio of a characteristic turbulent time scale (t_T) to a characteristic chemical time scale (t_c), determines whether diffusion or reaction rates are more dominant over the length and time scales of interest. Damköhler number is expressed as:

$$Da = \frac{t_T}{\mathrm{tc}} = \frac{S_L\, L}{u'\, \delta_F} \tag{2.17}$$

- For Da $\gg$ 1: very fast chemical reactions (short chemical time) compared to the time for an eddy to turn over. Thus, due to the slow diffusion rate, turbulence does not affect the flame front structure (reaction is assumed to instantaneously in equilibrium).
- For Da $\ll$ 1: turbulent eddies are faster than chemical reactions, which means diffusion reaches an equilibrium well before the chemical reactions. Thus, flame is affected by turbulence scales.

2.4.2.2 Karlovitz number (ka)

Karlovitz number, which is defined as the ratio of chemical time scale (t_c) over turbulent time scale (t_T or Kolmogorov time scale), is expressed as:

$$Ka = \frac{t_c}{t_T} = \frac{{\delta_F}^2}{\eta^2} = \frac{1}{Da} \tag{2.18}$$

- For Ka > 1: turbulent eddies are much faster than chemical reactions, which means small-scale eddies (Kolmogorov) can affect the flame front structure.
- For Ka < 1: chemical reaction rates are faster than small-scale eddies (Kolmogorov) which mean turbulence does not have an effect on the flame front structure.

2.4.3 Premixed flames structure

The structure of a premixed flame, as proposed by Peters [45], consists of three layers (see Fig. 2.8): a preheat layer with little or no chemical reactions, an inner layer by which most of the chemical reactions occur, and an oxidation layer where radicals go through complete oxidation. To describe how the flame front structure reacts to turbulence, Zeldovich has proposed a common definition of the premixed flame thickness as follows [64]:

$$\delta_F = \frac{\lambda}{C_p \rho_u S_L} \tag{2.19}$$

where λ is the thermal conductivity, C_p is the specific heat capacity at constant pressure, ρ_u is the density of the unburned gases, and S_L is the laminar burning velocity. δ_F is a measure of the thickness of the preheat zone where the unburned mixture is heated up to the ignition temperature by the reaction zone which consists of an inner and an oxidation layer. The inner

Layer (l_δ) is also called the fuel consumption layer since it is responsible for keeping the reaction process alive. Under intense turbulent mixing, the entire flame structure is disrupted when small turbulent eddies (Kolmogorov) penetrate the inner layer and hence enhance heat conduction and diffusion of radicals out of it [45]. This leads to separation between chemistry and turbulence as the Kolmogorov eddy size becomes thinner than the inner layer. Measuring this inner layer thickness is very challenging as it requires the measurement of different chemical scales such as chemical time scale, diffusion coefficient, temperature, pressure, and inverse chemical time scale.

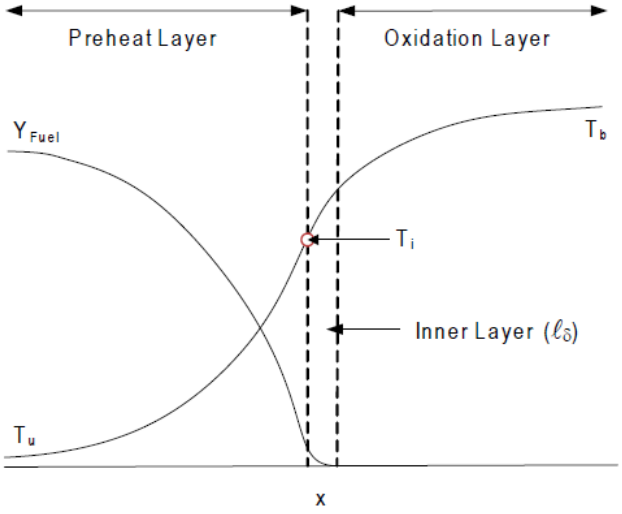

Figure 2.8. Schematic diagram of the typical premixed flame structure [65] where Tu, Ti, and Tb are unburned, ignition, and burned temperatures, respectively.

2.4.4 Combustion regimes

To describe and understand the influence of different turbulence length scales on the flame front, different turbulent flames regimes were proposed. These diagrams (or regimes) are called Borghi and Peters diagrams which are presented in terms of the integral length scale to

laminar flame thickness ($^{L}/_{\delta_F}$), and the ratio of turbulence intensity to laminar burning velocity ($^{u'}/_{S_L}$). These diagrams are divided into four regimes: wrinkled flamelets regime, corrugated flamelets regime, thin reaction zone, and broken reaction zone as depicted in Fig 2.9.

- Wrinkled Flamelets Regime: $\delta_F \leq \eta,\ \frac{u'}{S_L} < 1,\ Re > 1,\ Ka < 1, Da \gg 1$

  In this regime, flame thickness (δ_F) is much smaller than Kolmogorov scales (η) and Damkohler number (Da) is larger than 1. Thus, the turbulent motion can only wrinkle the laminar flamelets and cannot influence the chemical reaction within the flame front, as the chemical time is much faster than that of the turbulent mixing (Figure 2.10 (a)).

- Corrugated Flamelets Regime: $\delta_F \leq \eta,\ \frac{u'}{S_L} > 1,\ Re > 1,\ Ka < 1,\ Da > 1$

  This regime, in combination with the wrinkled flamelets regime, forms together the flamelets zone as they share similar conditions except that turbulent intensity, u', in the corrugated zone is larger than the flame speed (S_L). Thus, due to higher turbulent intensity, the larger eddies move at faster velocity than the flame speed by which these eddies will push the flame front around and cause a significant convolution and consequently pockets of burned and unburned gases will be formed (Figure 2.10 (b)). However, the flame structure will not be perturbed by turbulent fluctuations and remains quasi-steady.

- Thin Reaction Zone: $\delta_F > \eta,\ \frac{u'}{S_L} > 1,\ Re > 1,\ Ka > 1,\ Da \cong 1$

  In this region, turbulence fluctuations are more intense than the smallest scales (Kolmogorov) which become smaller than the flame thickness and hence penetrate the

reactive-diffusive flame structure and increase scalar mixing (Figure 2.10 (c)). However, the small-scale eddies are still larger than the inner layer thickness (l_δ) and therefore cannot penetrate that layer.

- Broken Reaction Zone: $\delta_F > l_\delta > \eta,\ \frac{u'}{S_L} > 1,\ Re > 1,\ Ka > 1,\ Da \ll 1$

  Due to intense turbulence and relatively slow chemical reactions (Da<1), the Kolmogorov scales become smaller than the inner layer thickness. Thus, these scales penetrate the inner layer causing heat loss to the preheat zone followed by temperature decrease and loss of radicals (Figure 2.10 (d)). Eventually, the flame propagates in a disturbed way rather than front propagation, which causes the flame to extinguish.

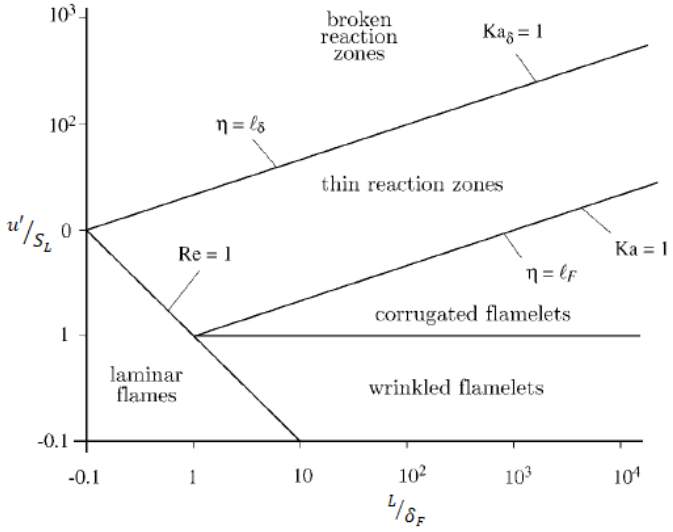

Figure 2.9. Borghi Regime diagrams revised by Peters [45].

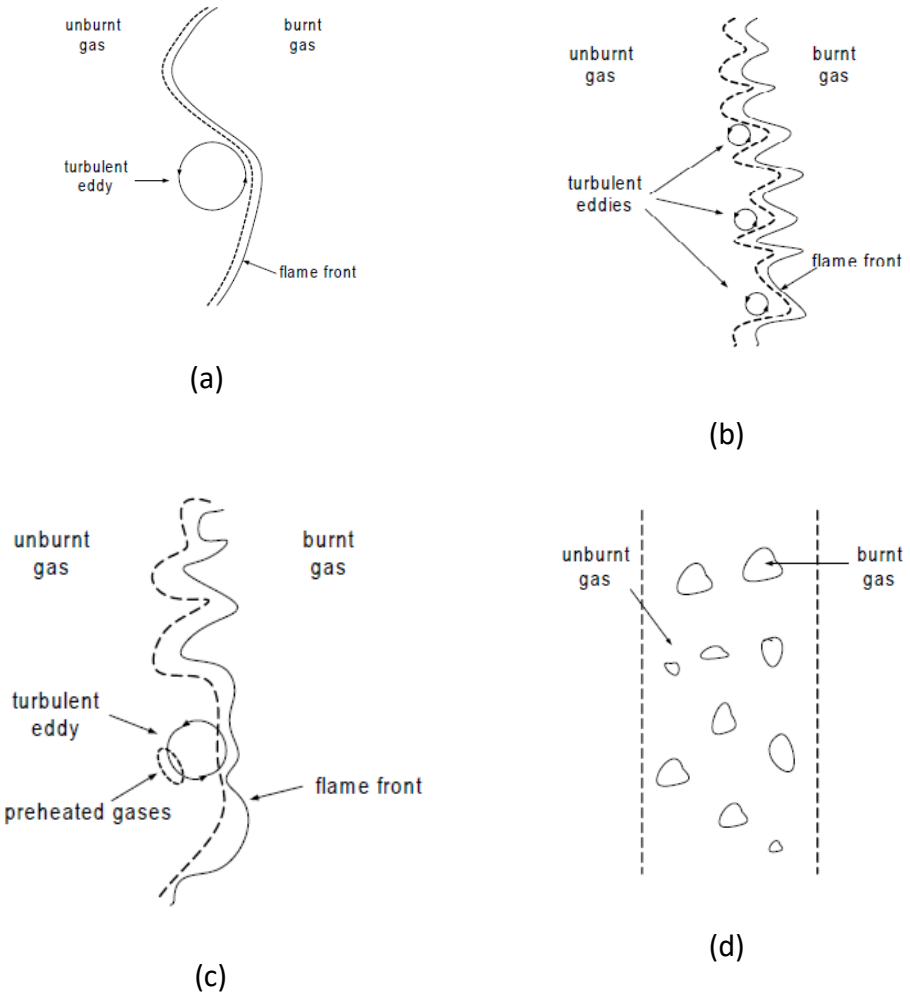

Figure 2.10. Turbulent flames structure[65]: a) Wrinkled b) Corrugated c) Thin reaction zone d)Broken reaction zone.

2.4.5 Reference radius

Turbulent burning velocity of spherical propagating flame is determined at a reference point where its propagation attains a mean radius equal to 1.5 times the integral length scale [54,58,66,67]. Such a smaller radius might result in a flame that is still significantly affected by the ignition energy and subjected only to a smaller portion of the turbulent velocity field, while

a larger radius could be only be achieved beyond the field of view and thus measuring the propagating speed will not be possible. Therefore, the selection of a mean flame radius of 1.5 times the integral length scale was considered a reasonable compromise between these factors [54,58,66,67].

CHAPTER 3 - LITERATURE REVIEW

3.1 Introduction

In this chapter, a literature review of published studies on laminar and the turbulent burning velocity of biogas is presented, respectively, in sections 3.2 and 3.3. At the end of each main section, a summary of the conditions, techniques, and fuel compositions is given in a table.

3.2 Laminar burning velocity

Laminar burning velocity (S_L) is one of the fundamental combustion parameters [68,69]. It is defined as the speed of the combustion wave normal to itself and relative to the unburned gas [45]. Thus, accurately measuring laminar burning velocity is important for enhancing and validating chemical kinetic mechanisms [70].

Many experimental and numerical studies were performed on the laminar burning velocity of biogas under ambient and elevated temperature and pressure conditions over a wide range of equivalence ratios.

3.2.1 Biogas-air mixtures

3.2.1.1 under ambient conditions

Laminar flame speed of biogas-air mixtures was investigated under atmospheric pressure and room temperature by many researchers since late 1980s (e.g., [13, 21]). These studies were performed under ambient temperature and atmospheric pressure using numerical and experimental approaches (counter flow method). Up to 60% Vol of CO_2 was added to methane-

air mixtures for a wide range of equivalence ratios (between 0.4 and 1.8). Reported results showed that when CO_2 was added to methane-air, the laminar burning velocity reduced with the adiabatic flame temperature.

Later on, a new methodology for determining laminar flame speed was developed by Ju et al. [26]. The approach was based on two numerical mechanisms using CHEMKIN-based code [71] to study radiative transport including emission and absorption via narrow-band statistical model with exponential-tailed inverse line strength distribution [71]. The objective was to test the effect of lean mixtures of methane and CO_2 reabsorbing of radiation and consequently calculate laminar flame speed. It was found that as CO_2 concentration increased, heat reabsorption approximately reduced the net heat loss nearly to half. This affected the lower flammability limit and decreased laminar flame speed as well. Nevertheless, this methodology is still limited by several conditions as the nature of the gas radiation is unique for each gas and the differences between spectral characteristics of reactants and products are wide. Also, the temperature broadening of the emissions/absorption spectra is different too. However, the results are relatively in agreement with the previous studies [5,15].

Moreover, a combined numerical and experimental study was performed by Qin et al. [28] to examine the laminar flame speed, flammability limits and other combustion characteristics of Landfill gas (up to 50% CO_2 Vol) over a wide range of equivalence ratio (0.5-2.0) and under standard conditions. In their approach, the author studied the landfill gas (LFG) from different perspectives including thermal radiation, extinction strain rates, detailed flame structures, and NOx emissions, by using a stagnation flow burner and two codes established with CHEMKIN 2 with GRI 2.11 mechanism for the description of the chemical kinetics. Reported

results showed a good agreement with published studies regarding the effect of CO_2 on reducing flame speed and flammability limits. For instance, before CO_2 addition (only methane-air mixtures), laminar flame speed was noticed to peak (41 cm/s) at equivalence ratio 1.1. As CO_2 percentage was increased from 0% to 50%, this peak in the flame speed was significantly reduced (21 cm/s) and the flammability limits were significantly decreased. Qin et al. [27] explained this effect of CO_2 on reducing the burning velocity and flammability limits by a kinetic and/or thermal nature. Using detailed numerical simulations, they noticed that the destruction rate of CO_2, in comparison to the production rate, was very small so that CO_2 was considered as relatively stable species that could be treated as an inert. However, this kinetic effect was considered as minor for small concentrations of CO_2 in the mixture (less than 5% per mole). On the other hand, the thermal effect of CO_2 on the combustion intensity was maintained by two mechanisms. The first one was the reduction of the flame temperature as CO_2 behaved as a heat sink, hence diluting the mixture. The second mechanism was by radiation heat loss which was attributed to the larger specific heat of CO_2.

Nevertheless, similar results were reported by the study of Kishore et al. [23] who experimentally and numerically studied the influence of adding CO_2 (up to 60% Vol) and N_2 (up to 40% Vol) on the laminar burning velocity of methane-air mixtures for equivalence ratios between 0.8 and 1.3. Reported observations showed that in comparison to N_2 addition, CO_2 led to a more significant reduction in the laminar burning velocity of methane-air mixtures and a higher decrease in the adiabatic flame temperature. This behaviour was explained by the stronger impact of CO_2 on flame parameters due to its higher specific heat as opposed to N_2 which caused a faster radiation heat loss [28].

Another comprehensive study was performed by Nonaka et al. [31] to calculate and measure the laminar burning velocity of methane diluted with up to 50% CO_2 Vol using numerical and experimental approaches. In their study, the burning velocity was measured experimentally by the heat flux method, and validated by using five detailed reaction mechanisms under a wide range of equivalence ratio. The reported results showed a good agreement with other experimental data and correlations available in the literature regarding the effect of CO_2 dilution on decreasing the burning velocity and consequently shifting it towards the leaner mixtures. This effect was attributed to the influence of CO_2 in increasing the mixture density and molar heat capacity. This, in return, reduced the reactants concentration and flame temperature causing a decrease in the burning velocity.

3.2.1.2 Under elevated conditions

Determining biogas laminar burning velocity under elevated temperature and pressure conditions is important for optimizing the performance of the internal combustion engines [72,73] and gas turbine engines [74,75]. Hinton et al. [20] and Elia et al. [27] performed two separate experimental studies to measure the laminar burning velocity of biogas by using pressure rise data from constant volume combustion [76] at equivalence ratios between 0.7 and 1.4. In their approaches, Hinton et al. [18] and Elia et al. [26] added, respectively, up to 40% and 14% CO_2 Vol to methane-air mixtures, under similar temperature (up to 247 °C) and pressure (up to 20 atmospheres) conditions. Reported results of both studies showed a good agreement in the behaviour of the laminar burning velocity; that is, as the temperature increased, laminar flame speed increased due to faster release of radicals, while as the pressure increased, laminar flame speed exhibited a decreasing trend as the radicals were released more slowly.

Another experimental study was performed by Anggono et al. [19] to study the combustion performance of biogas (33.4% CO_2 Vol) at reduced pressure (0.5 atmospheres) and room temperature. Experiments were conducted using a high-pressure fan-stirred combustion vessel at various equivalence ratios covering both lower and higher flammable limits. At atmospheric pressure and room temperature, biogas ignited at equivalence ratios ranging between 0.6 and 1.2 with a maximum burning velocity of 25 cm/s at stoichiometry. However, as the pressure was reduced to 0.5 atm, biogas flammability was significantly limited to equivalence ratios ranging between 0.75 and 0.85 but with a lightly higher burning velocity (27 cm/s) at stoichiometry. The reduction in pressure has two conflicting effects on the biogas combustion and flammability. The fuel fraction in the mixture became smaller which hence led to a stronger effect of the mixture diluents (CO_2) in absorbing heat energy and consequently lowering the flammability limits. On the other side, this reduction in the pressure caused the reactants diffusion time to decrease, so the resident time became longer and consequently, the laminar burning velocity enhanced.

3.2.2 Biogas-additive-air mixtures

Combining lower calorific fuels with higher ones is a promising strategy in optimizing and developing alternative fuels that have low burning velocity and weak stability such as biogas. This technique includes the addition of hydrogen, propane, syngas, and oxygen enrichment. In this section, a summary of experimental and numerical investigations on the laminar burning velocity of biogas blended with other fuels is represented.

3.2.2.1 Biogas + H2

Due to the high reactivity and burning velocity of hydrogen, significant improvements in burning velocity, flame stability and flammability [77,78] were reported when adding hydrogen to a wide range of hydrocarbon fuels [79–81]. Hydrogen addition to biogas was studied for examining the performance and emissions of internal combustion engines [82–85]. However, only a fewer experiments were contributed to determining laminar burning velocity and flammability. Zhen et al. [21] investigated the effect of hydrogen addition on biogas stability, laminar burning velocity, emissions, and thermal characteristics, for equivalence ratios between 0.8 and 1.2. The study was implemented using Bunsen burner at room temperature and atmospheric pressure, with hydrogen addition from 10% to 50% Vol to several biogas compositions (60%-40% CH_4 Vol). In their experiments, Zhen et al. [19] found that as CO_2 concentration in biogas increased, the threshold value of hydrogen fraction needed to maintain a stable biogas flame increased as well, and the laminar burning velocity exhibited a monotonic increase at higher hydrogen fractions (up to 47 cm/s for 50% H_2 at ϕ=1.2). Furthermore, the addition of hydrogen also caused an increase in flame temperature, which led to a monotonic decrease in CO as a function of hydrogen addition. The effect of hydrogen addition to biogas-air mixtures was also studied by Wei et al. [32] to investigate the heat transfer characteristics of the laminar flames at different H_2 (up to 50%) and CO_2 (between 25-50%) volumetric fractions. Experiments were performed at an equivalence ratio of ϕ=1.2 using Bunsen burner method to measure heat flux and temperature distributions, while the laminar burning velocity was calculated numerically using PREMIX code of CHEMKIN 2 with the mechanism GRI 3.0 [86]. Reported results showed a significant enhancement in the total heat transfer rate of biogas flame

by up to 50% with optimal hydrogen addition of 30% volume fraction. On the other hand, the existence of CO_2 in biogas suppressed the CO oxidation and reduced the fraction of the combustible fuel, which consequently decreased the flame temperature by confining the heat release due to its larger specific heat capacity. The reported effect of hydrogen addition on the laminar burning velocity confirmed the results obtained previously by Zhen et al. [21]. For instance, when the hydrogen fraction increased from 0% (pure biogas) to 50%, the laminar burning velocity significantly increased from 26 cm/s to 42 cm/s at ϕ=1.2, while at the same conditions, Zhen et al. [19] obtained 46 cm/s which is within the same range. Ji et al. [25] studied the influence of the addition of up to 15% of CO_2 by volume fraction to four stoichiometric natural gas-hydrogen compositions (natural gas at 20-40-60-80% Vol) in a constant volume combustion chamber at pressures varying between 0.08 and 0.2 MPa. Their results showed an acceptable agreement of the laminar burning velocity of the natural gas with the studies mentioned above under the effect of CO_2 and hydrogen addition. As such, increase in the hydrogen fractions has led to a significant increase in the laminar burning velocity; whereas, the more CO_2 was added, the lower the burning velocity was. However, as the pressure was increased from 0.08 MPa to 0.15 MPa, the laminar burning velocity exhibited an increasing trend at first, after which it started decreasing with further pressure increase from 0.15 to 0.2 MPa for all fuel compositions. This observation regarding the behaviour of the laminar burning velocity of biogas under the influence of hydrogen addition and initial pressures was also reported by Zheng et al. [24] at equivalence ratios varying between 0.8 and 1.2. In their experiments, Zheng et al. [24] measured the laminar burning velocity and flame stability of CO_2 (0-15% Vol) diluted natural gas-hydrogen-air mixtures in a constant volume combustion vessel using high-speed Schlieren photography, with hydrogen

fractions varying between 10% Vol and 30%Vol at initial pressures varying between 0.1 and 0.6 MPa. At fixed initial pressure and dilution ratio, laminar burning velocity showed an increasing trend with hydrogen addition while the flame thickness and stability reduced significantly. On the other hand, increasing the initial pressure had a reducing effect on the burning velocity and the flame thickness, while increasing the dilution ratio enhanced the flame stability and Markstein length due to the thermo-diffusivity factor.

3.2.2.2 Biogas + Oxygen enrichment

A numerical study was performed by Hu et al. [17] to study the chemical effect of CO_2 on the laminar flame speed of $CH_4/CO_2/O_2$ mixtures using a kinetic simulation of various oxygen concentrations and equivalence ratios (ϕ between 0.5 and 1.5). They found that CO_2 has a chemical effect on the flame speed which is lower than the thermal effect but much higher than that of the diffusive. On the other hand, the influence of the third body efficiency of CO_2 in the lower oxygen concentrations decreased the laminar flame speed, while at higher oxygen concentrations, the laminar flame speed exhibited an increasing trend. However, this effect of CO_2 was reported to reach a maximum at stoichiometric equivalence ratio. Benedetto et al. [18] studied the explosion behaviour of stoichiometric $CH_4/CO_2/O_2/N_2$ mixtures at different CO_2 contents (20% to 60% Vol) and oxygen enrichment factors (from 0.21 to 0.8 in air). They measured the peak pressure, laminar burning velocity, and the maximum rate of pressure rise using a closed cylindrical vessel. They also performed numerical simulations using CHEMKIN-PREMIX for comparison purposes. They concluded that the peak pressure and maximum rate of pressure rise both experienced an increasing trend as either the CO_2 concentrations decrease in the mixture or as the oxygen enrichment increases. On the other hand, the laminar burning

velocity exhibited an opposite trend as a function of either increasing CO_2 concentrations or decreasing oxygen enrichment. The authors explained this behaviour by the effect of CO_2 on increasing the specific heat of the mixture which consequently lowered the flame temperature and the combustion rate. Another study on the influence of O_2 enrichment and CO_2 dilution on the laminar flame speed was performed by Hu et al. [33]. They investigated experimentally and numerically the variations in the laminar flame speed for equivalence ratios varying between 0.6 and 1.4 with 25% to 35% oxygen enrichment (Vol in air) using Bunsen burner and GRI-Mech.ver 3.0 mechanism from a CHEMKIN package. As it was expected, with increasing O_2 enrichment ratio, the laminar flame speed monotonically increased to reach a maximum (29.6 cm/s) at stoichiometric equivalence ratio. Under the effect of CO_2 addition, both the combustion reactants and products concentrations decreased in the oxygenated methane mixtures which consequently led to a drop in the burning velocity. Such observations were also reported by Xie et al. [16] who performed a similar study but at higher initial pressures and CO_2 dilutions ratios.

Although most of the performed studies investigated the effect of CO_2 and oxygen enrichment on methane-air mixtures using experimental and numerical approaches, yet they did not take into consideration the effect of water vapour on the combustion performance. Thus, to understand the possible influence of water vapour, Mazas et al. [30] studied the effect of H_2O on the laminar burning velocity along with CO_2 and oxygen enrichment. Their experiments were performed using a conical burner at atmospheric pressure and initial temperature of 373 K for equivalence ratios varying between 0.5 and 1.5, while their numerical simulations were conducted using a PREMIX code via detailed kinetic mechanism (GRI-mech. 3.0). They reported that by varying the oxygen enrichment (by mole basis on CO_2 and O_2) from 0.21 to 1.0, the laminar

flame speed experienced an increasing trend as more oxygen was added, which agrees with published studies. However, with increasing the water vapour ratios from 0 to 0.45 (based on mole fractions), the laminar flame speed experienced a quasilinear decrease much more like the effect of CO_2 addition.

3.2.2.3 Biogas + Propane

Comprehensive numerical and experimental studies were performed by Lee et al. [22,34,35] to determine the laminar burning velocity of two blended mixtures of 70% biogas (landfill gas, LFG) + 30% propane (liquefied propane gas, LPG) and 50% LFG + 50% LPG. Their experiments were conducted over a wide range of equivalence ratios and under ambient conditions by using a premixed nozzle type combustor; while their numerical simulations were performed using C3 elementary reaction mechanism by GRI-v2.11 and two reaction mechanisms [49] [71]. With 30% LPG addition to biogas, a significant increase in the laminar burning velocity from 25 cm/s to nearly 38 cm/s was reported, with a shift in the peak burning from stoichiometry to ϕ=1.1. However, when more LPG was added (50%), stronger quenching effect was noticed and the increase in the laminar burning velocity became of less significance. Nonetheless, based on their experimental and numerical results, two numerical correlations were proposed to calculate the laminar burning velocity according to the equivalence ratio for LFG-LPG mixtures.

3.2.2.4 Biogas + Propane-Hydrogen-Oxygen enrichment

A numerical and experimental investigation was performed by Cardona et al. [87] to determine the laminar burning velocity of oxygen-enriched biogas (66% CH_4 - 34% CO_2) and a biogas/propane/hydrogen mixture (50% biogas – 40% propane – 10% hydrogen) at 0.849 bar and

room temperature. Experimental measurements were carried out using a contour slot burner with angle method to determine the burning velocity, while their numerical calculations were performed using the PREMIX code of CHEMKIN-PRO package with two detailed kinetic mechanisms for comparative purposes. Their results showed that the influence of oxygen enrichment or adding propane and hydrogen on boosting the laminar burning velocity of biogas was reasonable. For instance, the maximum burning velocity reached by biogas-air mixture increased from 28 cm/s to 46 cm/s with the addition of propane and hydrogen, while the flammability limit extended significantly. On the other hand, with oxygen enrichment up to 28% and 32% (percentage in air), the laminar burning velocity of biogas-air significantly increased from 28 to 60 cm/s which is higher than that of biogas/propane/hydrogen air-mixtures. With the same oxygen enrichment (28% and 32% in air), the laminar burning velocity of the biogas/propane/hydrogen air-mixture reached an optimal value of 96 cm/s with wider flammability limits ($0.6<\phi<1.6$).

3.2.2.5 Biogas + Helium

The effect of spectral radiation absorption on the laminar burning velocity and flammability limits of [CH_4 – {0.3 O_2 + 0.2 He + 0.5 CO_2}] were experimentally and numerically studied at normal and elevated pressures (up to 5 atm) by Chen et al. [29]. Experimentally, the burning velocity was determined in an outwardly-propagating spherical chamber at elevated pressures and lean mixtures. While numerically, the obtained data were used in validating and developing a radiation model to predict radiation in spherical geometry. Reported results showed that enhancement in radiation absorption due to helium and CO_2 addition played a vital role in

increasing the burning velocity and extending the flammability limits. On the other hand, increasing the pressure had an opposite effect on flammability limits and burning velocity.

3.2.3 Summary

The laminar burning velocity of biogas is well documented in the literature over a variety of test conditions and fuel compositions, using both experimental and numerical approaches. Table 3.1 summarizes published experimental studies along with test conditions and employed technique.

Biogas-air						
Fuel	**Composition**	**P [bar]**	**T [K]**	**ϕ**	**Tech.**	**Ref.**
Biogas	100-40% CH_4 / 0-60% CO_2	1	298	-	Experimental (Counter flow) Numerical	[5]
Biogas	100-40% CH_4 / 0-60% CO_2	0.25-2	298	0.4-1.8	Experimental (Counter flow) Numerical	[15]
Biogas	100-70% CH_4 / 0-30% CO_2	1	298	<0.8	Numerical	[26]
Biogas	100-50% CH_4 / 0-50% CO_2	1-4	300	0.5-2.0	Experimental Numerical	[28]
Biogas	100-40% CH_4 / 0-60% CO_2	1	298	0.8-1.3	Experimental Numerical	[23]
Biogas	100-50% CH_4 / 0-50% CO_2	1	298	0.7-1.4	Experimental (Heat Flux) Numerical	[31]
Biogas	60% CH_4 / 40% CO_2	1-19	298-660	0.7-1.4	Experimental (Constant Volume Combustion)	[20]
Biogas	100-85% CH_4 / 0-15% CO_2	0.75-20	298-550	0.8-1.2	Experimental (Constant Volume Combustion)	[27]
Biogas	66.4% CH_4 / 33.6% CO_2	0.5	298	0.75-1	Experimental (Constant Volume Combustion)	[19]
Biogas + Additives						
Biogas + H_2	60-40% CH_4 / 40-60% CO_2 + 10-50% H_2	1	298	0.8/1.0/1.2	Experimental (Bunsen Burner)	[21]
Biogas + H_2	75-50% CH_4 / 25-50% CO_2 + 10-50% H_2	1	298	1.2	Experimental (Bunsen Burner)	[32]
Biogas + H_2	80-20% CH_4 / 0-30% CO_2 + 80-20% H_2*	1	298	1.0	Experimental	[25]

					(Constant Volume Combustion)	
Biogas + H_2	90-70% CH_4 / 0-15% CO_2 + 10-30% H_2*	1	298	0.8-1.2	Experimental (Constant Volume Combustion)	[24]
Biogas + O_2 Enrichment	CH_4 / CO_2 (not clear) + 25-80% O_2**	1	300	0.5-1.5	Numerical	[17]
Biogas + O_2 Enrichment	80-40% CH_4 / 20-60% CO_2 + 21-80% O_2**	1	298	1.0	Experimental (Constant Volume Combustion) Numerical	[18]
Biogas + O_2 Enrichment	CH4 / CO_2 (not clear) + 25-35% O_2**	1	300	0.6-1.4	Experimental (Bunsen Burner) Numerical	[33]
Biogas + O_2 Enrichment	Z CO_2 = X CO_2/(X CO_2 + XO_2) (0.4-0.7)	1-3	300	0.4-1.6	Experimental (Constant Volume Combustion) Numerical	[16]
Biogas + O_2 Enrichment + H20 (Steam)	CH_4 / CO_2 + 21-100% O_2*** + 0-45%$H_2$0 (in reactive mixture)	1	373	0.5-1.5	Experimental (Conical Burner) Numerical	[30]
Biogas + Propane	27.25-54.5% CH_4 / 18.75-37.5% CO_2 + 0-50% C_3H_8	1	298	0.7-1.6	Experimental (Premixed Nozzle Combustor) Numerical	[35] [22] [34]
Biogas + Propane + H_2 + O_2 Enrichment	66% CH_4 / 34% CO_2 + 0-40% C_3H_8 + 0-10% H_2 + 21-32% O_2**	0.849	298	0.6-1.6	Experimental (Slot Burner) Numerical	[87]
Biogas + He	[CH_4 – {0.3 O_2 + 0.2 He + 0.5 CO_2}] Up to 0.5 CO_2 0.2 He	1-5	298	0.5-1.5	Experimental (Constant Volume Combustion) Numerical	[29]

Table 3.1. Summary of published test conditions adopted for determining the laminar burning velocity of biogas

*Percentage Volume of CH_4 + H_2

**Percentage Volume in air

***O_2/(O_2+CO_2)

3.3 Turbulent burning velocity

Optimizing combustion systems requires knowledge of the turbulent burning velocity of fuel under both ambient and elevated conditions. This section reviews published studies related to the turbulent burning velocity of biogas under ambient and elevated temperature and pressure conditions.

3.3.1 Ambient conditions

3.3.1.1 Biogas-air mixtures

An experimental approach was conducted by Shy et al. [36] to investigate the effect of CO_2 and N_2 addition on the turbulent burning velocity of methane-air mixtures at specific equivalence ratios (ϕ=0.7 and 1.4) under normal conditions. A Cruciform Bomb setup consisted of a long vertical vessel (to provide a sizable downward propagation of the premixed flame) and a large horizontal vessel (to generate intense isotropic turbulence in the central region) was used to measure the turbulent burning velocity by two sets of ion collecting electrodes inside the apparatus. Results showed that CO_2 addition (30-41% Vol of fuel) to methane-air mixtures showed a more significant effect on reducing the turbulent burning velocity than N_2 addition (41-56% Vol of fuel). Shy et al. [36] attributed this effect to the higher tendency of CO_2 to lose heat four times more than N_2 through radiation from soot and emitting species that were found in the burnt gases. Because of these radiation losses, the turbulent burning velocity of both CO_2-methane and N_2-methane mixtures dropped to nearly half at rich equivalence ratio in comparison to lean mixtures.

3.3.1.2 Biogas-H2-air mixtures

In the previous section, Shy and coworkers studied the influence of CO_2 and N_2 addition on the turbulent burning velocity of methane-air mixtures, taking into considerations heat radiation losses at lean and rich equivalence ratios and under ambient conditions. Although this study was not performed to simulate EGR (Exhaust Gas Recirculation) in internal combustion engines, it could play a part in investigating the effect of introducing EGR to methane under turbulent conditions since it examines the influence of CO_2 addition to methane-air mixtures. However, many studies investigated the effect of EGR on methane (or natural gas) laminar flames such as Hu et al. [88,89] and Zhang et al. [90]. Results showed that introducing EGR into internal combustion engines reduced NO_x emissions by decreasing the flame temperature, and increased the combustion duration and cyclic variations of the engine. Nevertheless, very few studies were published on the effect of EGR on turbulent flames with hydrogen addition. To cover this gap, Wang et al. [37] studied the turbulent combustion of CH_4-H_2-air flames under the influence of EGR dilution, where CO_2 was chosen to represent EGR by adding up to 10% CO_2 by total volume of air and up to 20% H_2 by total volume of CH4 + H2 (fuel). In this study, a Bunsen turbulent burner was used to establish the flames and measure the turbulent burning velocity using the angle method technique. The flame characteristics were included in the flamelet regime in Borghi`s diagram, where all characteristic scales of turbulence showed a decreasing trend as turbulence intensity increases.

Without dilution (100% methane-air mixtures), the turbulent burning rate (ST/SL) of methane varied nearly between 1.5 and 3.5. With hydrogen addition (20% H_2), these values shifted upward significantly due to the high reactivity of hydrogen. However, as more EGR was

introduced (hence more CO_2), slower burning rate was obtained. This decrease in the turbulent burning velocity after introducing CO_2 was also noticed in Shy`s experiments and was explained by the effect of heat radiation losses. However, hydrogen was not added to the mixture in their experiments. Nevertheless, Wang et al. explained the possible reasons for this decrease in ST/SL as follows; diluting the CH_4-H_2-air mixtures with CO_2 increased the local flame stretch L_m which led to a stronger flame response to stretch rate. Thus, this caused the local burning velocity (SL) in the turbulent flame regime to reduce which therefore decreased ST/SL. On the other hand, as more CO_2 was added, less wrinkles were created and thus resulted in smaller turbulent flame front area A_T. Thus, according to the equation 3.1 [88], this decrease in A_T caused the turbulent burning rate, ST/SL, to decrease in return.

$$ST/_{SL} = {A_T}/_{A_0} \tag{3.1}$$

Therefore, the turbulent burning velocity is controlled by two factors: wrinkling- which directly affects the turbulent burning rate (ST/SL) by reducing the local flame front area, and the stretch rate which plays a vital role in constraining the tendency of the flame to propagate, especially at higher CO_2 ratios. Thus, the desired enhancement in the turbulent burning velocity of methane-air mixtures reached by the addition of hydrogen could be compromised by the diluting effect of CO_2 addition to the mixture. Thus, as it was noticed in this study, the 20% addition of H_2 to methane-air mixtures increased the turbulent burning rate by almost 25%. However, when EGR was introduced with 5% of CO_2 to the methane-hydrogen-air mixture, the decrease in the turbulent burning rate overcame the advances of hydrogen addition, which led to even lower ST/SL than pure methane-air mixtures.

2.3.2 Elevated conditions

The aforementioned studies of Shy et al. and Wang et al. in the previous section investigated the turbulent burning velocity of CH_4-CO_2-air (biogas) and CH_4-CO_2-H_2-air (biogas + H_2) mixtures under ambient temperature and pressure conditions at two equivalence ratios (ϕ= 0.7 and 1.4). Hence, these studies do not cover all realistic test conditions. The following sections review studies related to turbulent burning velocity under elevated temperatures and pressures.

3.3.2.1 Effect of high pressure

An experimental study was performed by Cohe et al. [91] to investigate the effect of high pressure and CO_2 addition on the turbulent flame structure of methane-air mixtures, including the turbulent burning velocity (S_t), flame surface density, and instantaneous flame front wrinkling parameters. Experiments were performed at a lean equivalence ratio (ϕ = 0.6) and under high pressures (9 bars) using an axisymmetric turbulent Bunsen burner inside a high-pressure combustion chamber. Biogas mixtures were prepared by adding up to 35% of CO_2 to methane-air mixtures based on the mole fraction of the fuel (CH_4 + CO_2). Reported results showed that as more CO_2 was added, larger increase in the turbulent flame brush thickness was noticed with no effect on the distributions of the flame curvatures and the wrinkling characteristics. However, when the pressure was increased, small flame wrinkles of minor curvature radii were generated followed by a significant enlargement in the flame volume. As a result of these flame wrinkles, the burning velocity of the laminar (SL) and turbulent flames (ST) significantly decreased which consequently increased the burning rate. Therefore, by increasing both the CO_2 and pressure, laminar and turbulent burning velocities decreased which in return increase the turbulent

burning rate (ST/SL). However, the growth rate of ST/SL under the effect of pressure is not similar to that of the CO_2. For instance, with 35% CO_2 addition at 0.1 MPa, ST/SL only increased by a factor 2 in comparison to 0% CO_2 which was much similar to the two other cases (at 0.5 MPa and 1 MPa). On the other hand, when the pressure increased from 0.1 to 0.5 MPa, the rise in the turbulent burning rate was more intense for all CO_2 ratios. Thus, this observation showed a dominant effect of the pressure over the CO_2 dilution rate. To explain this behaviour, CO_2 addition, as previously stated, did not have a significant effect on the flame curvature and wrinkling characteristics since it only affected the turbulent flame brush thickness. High pressure, on the other hand, exercised a strong effect on the flame curvature and wrinkling characteristics which hence led to a further decrease in the burning velocity and thus an increase in ST/SL.

3.3.2.2 Effect of high pressure and temperature

In the previous section, the effect of elevated pressure on the turbulence burning velocity of biogas was discussed under ambient temperature. Results showed that the turbulent burning velocity had an inversely proportional relationship with CO_2 addition and pressure increase. However, this behaviour of the turbulent burning rate under elevated pressure acted differently when high temperature was introduced. Like laminar flames, the turbulent burning velocity of biogas is expected to increase under high temperature and decrease under high pressure, as it was shown previously in section 3.2. Nevertheless, to confirm this behaviour, two different studies on biogas turbulent flames were performed by Bagdanavicius et al. [39] and Kobayashi et al. [40] under elevated pressure and temperature conditions using Bunsen burner in a high pressure and temperature combustion chamber. Experimental conditions and fuel compositions of the two studies are shown in Table 3.2. The results of both experiments were not much similar

regarding the influence of the elevated temperature and pressure on the behaviour of the turbulent burning rate, even though the conditions were comparable. For instance, Bagdanavicius et al. reported an inversely proportional relationship between the turbulence burning intensity (ST/SL) and the amount of CO_2 added to the mixture. On the other hand, this was not the case with the results of Kobayashi et al.; the influence of CO_2 addition to methane-air mixtures under the elevated temperature and pressure led to a decreasing trend of the turbulent burning rate. For example, when the CO_2 dilution rate was increased from 0 to 10%, the turbulent burning rate ST/SL decreased significantly from 13 to 8 at the same turbulence intensity (u'/SL=3). However, in the previous studies of Shy et al. and Wang et al., the opposite was reported. Also, the turbulent burning rates of Kobayashi et al. over predicted those of Bagdanavicius et al. at all turbulence intensities.

However, to explain the higher values of ST/SL obtained by Kobayashi et al., Bagdanavicius et al. mentioned several causes for these discrepancies. For instance, the techniques used in these two studies to identify the flame are different as Kobayashi et al. used OH-PLIF laser diagnostic to define the flame front, whereas Bagdanavicius et al. used the more traditional planar laser tomography. Moreover, different image processing methods were employed in both studies as Kobayashi et al. used average-image processing technique, while Bagdanavicius et al. used the single image processing practice. All these reasons can account for the discrepancies in the magnitude but not in the trends. However, Kobayashi et al. explained the unusual behaviour of ST/SL versus u'/SL by the effect of the local flame stretch which reduced the local turbulent burning velocity for the CO_2 diluted flame under high pressure and temperature because of the Markstein number effect. Hence, this led to a further decrease in ST

more than SL and thus normalising the turbulent burning velocity by the laminar velocity caused an increase in ST/SL.

3.3.3 Summary

The performed studies on the turbulent burning velocity of biogas were limited to understanding the influence of CO_2 addition (up to 41% Vol) to methane-air mixtures mostly at lean compositions (ϕ between 0.6 and 0.9) and under elevated temperature and pressure conditions. Thus, the behaviour of the turbulent burning velocity of biogas is still not well covered for a broad range of equivalence ratios, which is needed for the validation of the numerical turbulent combustion models.

The following table summarizes the available literature on the turbulent burning velocity of biogas, including the employed test conditions of pressure, temperature, fuel composition, and equivalence ratio.

Ambient Conditions									
Fuel	**Composition % Vol + Air**			**ϕ**	**T [K]**	**P [bar]**	**u' [m/s]**	**Tech.**	**Ref.**
	CH_4	**CO_2**	**H_2**						
Biogas	70-59	30-41	-	0.7/ 1.4	298	1	Up to 6	Cruciform Bomb	[36]
Biogas + H_2	100/ 80 Of fuel	0-10% of air	0/20 Of fuel	-	298	1	0.5 (not clear)	Bunsen Burner	[37]
Elevated Conditions									
Biogas	100-65	0-35	-	0.6	298	1-9	0.15-0.17	Bunsen Burner	[91]
Biogas	-	0-0.1% Vol of CO_2 +air	-	0.9	573	5/10	U'/SL Up to 5	Bunsen Burner	[39]
Biogas	85-70	15-30	-	0.65 - 1.45	473/673	3/7	1-3	Bunsen Burner in High Pressure Combustion Rig	[40]

Table 3.2. Summary of published test conditions adopted for determining the turbulent burning velocity of biogas

CHAPTER 4 – SPHERICAL COMBUSTION CHAMBER

4.1 Introduction

The experimental setup used in this work, which can withstand high-pressure and high-temperature premixed spherical combustion chamber, is suitable for studying the laminar and turbulent burning velocities. With a high degree of symmetry, this chamber is fitted with four pairs of axial fans to produce a nearly homogeneous and isotropic turbulence. The top view of the complete setup is schematically shown in Figure 4.1, and the front and side view of the actual setup is shown in Fig. 4.2. In this chapter, the experimental configurations, test conditions, Schlieren imaging technique, and turbulence characterization are briefly presented. More details can be found elsewhere [92, 93] as the same experimental configuration was used in these studies.

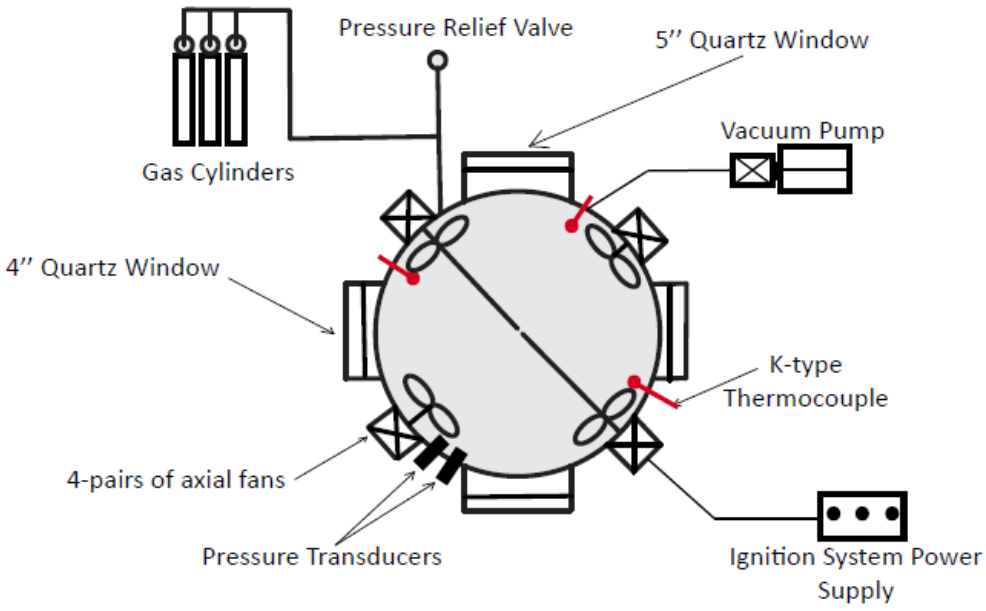

Figure 4.1. Schematic of the top-view of the experimental setup

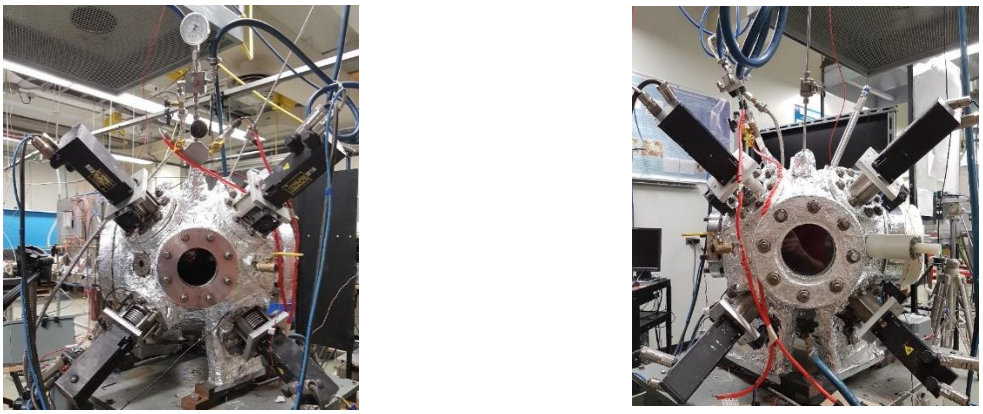

Figure 4.2. Front and side view of the spherical combustion chamber

4.2 The spherical combustion chamber

The spherical chamber (Figures 4.1 and 4.2) was developed in the Energy and Combustion Laboratory (ECL) [92] to generate controlled homogeneous and isotropic turbulence (HIT) under elevated pressure and temperature conditions. The chamber was constructed from two stainless steel hemispheres with an inner and an outer diameter of 380 mm and 405 mm, respectively. The chamber has two pairs of opposed quartz windows positioned 90-degree apart with one pair has a diameter of 125 mm, and the other has a diameter of 100 mm. These four quartz windows enable the access of the optical diagnostic techniques such as PIV, Schlieren technique and other visualization and imaging techniques. The turbulent flow field is generated by four pairs of six-bladed fans which are located at a distance of 200 mm across from one to another inside the spherical chamber. Each fan is driven by an independent servomotor which has a maximum rotational speed of 8000 rpm. In addition, the chamber has ten accessory ports for sensors and probes access such as thermocouples, pressure transducers, ignition electrodes, fuel/air injection and vacuum system. Control of the servomotors, as well as pressure and temperature feedback,

is interfaced through LabView software. Figure 4.3 shows the different ports' arrangements. Detailed description of the chamber is reported elsewhere [92] .

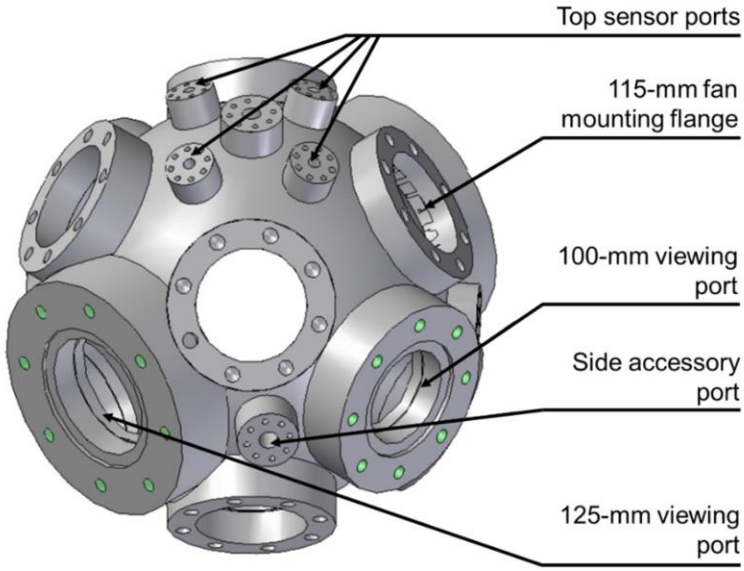

Figure 4.3. Ports' arrangement of the spherical chamber [92]

4.3 Fuel supply system

The combustion chamber is first flushed by injecting fresh air for 10 minutes to remove any residual gases. Afterwards, the chamber is vacuumed up to 6 psig using a vacuum pump. Then, the biogas-air mixture is injected into the chamber separately (e.g., CH_4 and CO_2) using the partial pressure methodology. After conducting the experiment, the whole process is repeated for the next experimental run. Appendix B.3 provides a detailed description of the fuel injection steps.

4.3.1 Partial pressure methodology

In order to inject the correct amount of fuel inside the chamber, the partial pressure methodology was used in this study for its simplicity and accuracy. This method is based on

Dalton's law of partial pressure (equation 4.1) and the ideal gas mixture relation (equation 4.2) as shown below [45]:

$$P_m = \sum_{i=1}^{K} P_i(T_m, V_m) \tag{4.1}$$

$$\frac{P_i}{P_m} = \frac{N_i}{N_m} \tag{4.2}$$

where P_m and P_i are, respectively, the partial pressures of the mixture and the fuel; T_m and V_m are, respectively, the temperature and volume of the mixture, and N_i and N_m are the number of moles of the fuel and the mixture, respectively. Thus, the pressure of the whole fuel-air mixture should be equal to the summation of the partial pressures of fuel and air. However, to calculate the partial pressures of each gas in the fuel-air mixture, the number of moles of each component should be calculated first. The equivalence ratio, ϕ, which is defined as the ratio of fuel to air mixure of actual over theoritical chemical reaction, is expressed as follows:

$$\phi = \frac{(m_f/m_a)_{actual}}{(m_f/m_a)_{stoichiometric}} \tag{4.3}$$

where

$$(m_f/m_a)_{stoichiometric} = \frac{(N_f.W_f)}{W_{air}\left((N_O.W_O)+3.76(N_N.W_N)\right)} \tag{4.4}$$

where m_f and m_a are the mass of fuel and air, W_f and W_{air} are the molecular weight of fuel and air, and W_O and W_N are the molecular weight of oxygen and nitrogen, respectively. Thus, the equivalence ratio is dependent on the number of moles and molecular weight of each mixture

component and it can possess three different conditions based on the ratio between the actual and stoichiometric (theoretical) mass ratios:

- ϕ = 1.0 represents the stoichiometric mixture, which means that the mass of air in the mixture is the amount needed for complete combustion.
- ϕ < 1.0 represents a lean mixture, which means that the mass of air in the mixture is larger than the amount needed for complete combustion.
- ϕ > 1.0 represents a rich mixture, which means that the amount of air in the mixture is lower than the amount needed for complete combustion.

Thus, the ratio of the partial pressure of fuel to the mixture can be given by the following equation:

$$\frac{P_f}{P_m} = \frac{N_i}{N_f + \frac{N_{air}}{\phi}} \tag{4.5}$$

where N_f and N_{air} represent the fuel and air number of moles, respectively. Consequently, to calculate the number of moles of each component, the chemical reaction of the fuel-air mixture should be considered as shown below for the general chemical reaction of oxygenated hydrocarbon:

$$C_\alpha H_\beta O_\gamma + \left(\alpha + \frac{\beta}{4} - \frac{\gamma}{2}\right)(O_2 + 3.76N_2) \rightarrow \alpha CO_2 + \frac{\beta}{2}H_2O + 3.76\left(\alpha + \frac{\beta}{4} - \frac{\gamma}{2}\right)N_2 \tag{4.6}$$

where N_f = 1.0 and N_{air} = $4.76 \times (\alpha + \frac{\beta}{4} - \frac{\gamma}{2})$. Thus, for stoichiometric equivalence ratio ϕ=1.0 and mixture pressure of 14.7 psi (i.e., 1 atm):

$$P_f = 14.7 \times \left[\frac{1}{1+\left(\alpha+\frac{\beta}{4}-\frac{\gamma}{2}\right)4.76}\right] \text{ psi}$$

For methane, $\alpha = 1, \beta = 4, \gamma = 0$

$P_f = 14.7\times \left[\frac{1}{1+(1+1)4.76}\right]$ psi

= 1.39 psi (or 0.095 atm)

For 60% CH_4 – 40% $C0_2$ biogas, the stoichiometric chemical reaction is:

$$nCH_4 + mCO_2 + (2n)(O_2 + 3.76N_2) \rightarrow (n+m)CO_2 + 2nH_2O + 2n\times 4.76N_2 \quad (4.7)$$

At T = 298 K, P = 14.7 psi (1 atm), ϕ = 0.8, n = 0.6 (60% CH_4) and m = 0.4 (40% CO_2):

- Partial pressure of CH_4:

$$\frac{P_{CH4}}{P_{mix}} = \frac{N_{Ch4}}{N_f + {}^{N_{air}}/_{\phi}} = \frac{0.6}{1+\frac{1.2\times 4.76}{0.8}} = 0.0737 \;\; \therefore P_{CH4} = 0.0737\times 14.7 = 1.08\, psi$$

- Partial pressure of CO_2:

$$\frac{P_{CO_2}}{P_{mix}} = \frac{N_{CO_2}}{N_f + {}^{N_{air}}/_{\phi}} = \frac{0.4}{1+\frac{1.2\times 4.76}{0.8}} = 0.049 \;\; \therefore P_{CO_2} = 0.049\times 14.7 = 0.72\, psi$$

- Partial pressure of air:

$$P_{air} = 14.7 - 1.08 - 0.72 = 12.9\, psi$$

Table 4.1 shows a summary of all partial pressures calculated for the tested biogas compositions at atmospheric pressure and room temperature.

	ϕ	n_{CH4} (mole)	n_{CO2} (mole)	P_{CH4} (psi)	P_{CO2} (psi)
50% CH_4 – 50% CO_2	0.5	0.0525	0.0525	0.6987	0.6987
	0.6	0.063	0.063	0.8225	0.8225
	0.7	0.0735	0.0735	0.9423	0.9423
	0.8	0.084	0.084	1.0576	1.0576
	0.9	0.0945	0.0945	1.1687	1.1687
	1	0.105	0.105	1.276	1.276
	1.1	0.1155	0.1155	1.3797	1.3797
	1.2	0.1261	0.1261	1.4799	1.4799
	1.3	0.1366	0.1366	1.5767	1.5767
	1.4	0.1471	0.1471	1.6705	1.6705
	1.5	0.1576	0.1576	1.7612	1.7612
60% CH_4 – 40% CO_2	0.5	0.0525	0.035	0.7099	0.4733
	0.6	0.063	0.042	0.8384	0.5589
	0.7	0.0735	0.049	0.9629	0.6419
	0.8	0.084	0.056	1.0835	0.7224
	0.9	0.0945	0.063	1.2005	0.8004
	1	0.105	0.07	1.3141	0.876
	1.1	0.1155	0.077	1.4243	0.9495
	1.2	0.1261	0.084	1.5313	1.0208
	1.3	0.1366	0.091	1.6352	1.0901
	1.4	0.1471	0.098	1.7362	1.1575
	1.5	0.1576	0.105	1.8344	1.223
70% CH_4 – 30% CO_2	0.5	0.0525	0.0225	0.7182	0.3078
	0.6	0.063	0.027	0.8499	0.3643
	0.7	0.0735	0.0315	0.9781	0.4192
	0.8	0.084	0.036	1.1029	0.4727
	0.9	0.0945	0.0405	1.2244	0.5247
	1	0.105	0.045	1.3426	0.5754
	1.1	0.1155	0.0495	1.4579	0.6248
	1.2	0.1261	0.054	1.5702	0.6729
	1.3	0.1366	0.0585	1.6797	0.7199
	1.4	0.1471	0.063	1.7865	0.7656
	1.5	0.1576	0.0675	1.8906	0.8103

Table 4.1. CH_4 and CO_2 partial pressures of three biogas compositions

4.3.2 Vacuum system

To inject the fuel gases into the chamber according to their partial pressures, the chamber should first be vacuumed. For this purpose, a Busch PB 0004 B vacuum pump (Fig. 4.4) is selected. This pump allows creating a vacuum of maximum 3 psi inside the chamber, which is fairly enough to form accurate equivalence ratio. The main features of the vacuum pump are: 4-4.8 m^3/h nominal suction capacity, 2 mbar ultimate capacity, 1.5 bar maximum allowable pressure, 0.1-0.12 nominal motor rating and 3000-3600 nominal speed.

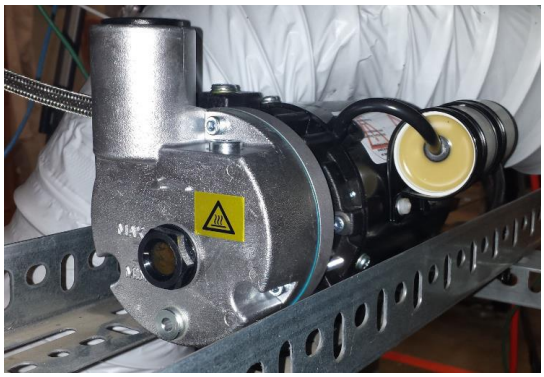

Figure 4.4. Vacuum pump

Before vacuuming, several steps were followed to make sure all vacuum conditions are fulfilled. First, the lubricant oil level inside the vacuum pump should be checked. Then, a pressure test is applied. This is done by pressurizing the chamber up to a certain pressure to make sure all windows and access ports are sealed and properly tightened. Finally, the exhaust of the pump is connected to the ventilation via an exhaust hose. The exhaust hose connects the exhaust port of the pump to the ventilation to prevent the exhaust emissions from leaking into the lab.

Once all the conditions mentioned above are met, the vacuum hose valve is opened, and the pump is turned on until the pressure inside the chamber reaches 6 gpsi. It is worth mentioning

that a 100% vacuum is very hard to achieve inside the spherical chamber as the pressure leakage becomes important at very low vacuum pressures. Moreover, after each combustion experiment, the unburned and burned gases resulted from the ignition are flushed by injecting fresh air for up to 10 minutes. This ensures that when fuel is injected, the partial pressures and hence the equivalence ratios are not influenced by the emissions of the previous combustion experiment. Although when the chamber is vacuumed to 6 gpsi, the remained air is fresh and contains no residual gases. A complete description of the operation of the vacuum pump is provided in the Appendix B.2.1.7.

4.4 Combustion chamber pressure control

As the combustion chamber is used for igniting gaseous fuels, pressure rise inside the chamber is expected to peak at a certain moment during the combustion. Before this time, the burning velocity analysis is assumed to be at a constant pressure or negligible pressure rise. Thus, the pressure rise effect on the flame propagation can be neglected. To monitor the pressure inside the setup, a pressure relief valve was mounted onto the combustion chamber. Adjustment of the valve pressure was made by setting a target pressure at the valve and then pressurize the chamber until the desired pressure is reached. Doing so is monitored by a 0-150 psi pressure transducer. A detailed description of the procedure is mentioned elsewhere [50]. During the experiments, the favourable pressure limit adjusted by the relief valves was 150 psi, that is to make sure that the 0-150 pressure transducer is not exposed to over-limit pressures which can damage its sensitivity. The pressure relief valve used (see Figure 4.5) is HY-LOK model RV1MF-

4N-S316 and has an operating pressure ranging between 10 and 250 gpsi with an orifice of 0.19 in^2 (122.58 mm^2) and a temperature of 204^oC.

Figure 4.5. Pressure relief valve

4.5 Ignition system

Igniting the fuel-air mixture inside the chamber was performed by operating a spark ignition system which consists of two tungsten spark electrodes (each having a diameter of 2 mm and a length of 400 mm separated by a 1-mm gap), an ignition transformer, solid state relay, and 120 VAC power supply which was later replaced by a 10 KV DC high-voltage booster. The full system is schematically shown in Figure 4.6. In order to synchronize the high-speed camera with the ignition, a LabVIEW interface software was used to control the experimental process. That is, the ignition order was initiated by the interface software which in turn triggers the high-speed camera 50 μs before ignition. The trigger provides a 5 VDC control signal from DAQ (Data acquisition system) to the solid-state relay to discharge a 10 000 VDC from a high-voltage booster through the gap between the two electrodes. Note that the electrodes are fixed to the chamber by fully insulated holders (see Appendix E) which are attached at the two lateral ports of the

vessel, as shown in Fig 4.7. The spherical chamber is grounded to discharge any flowing electrical current.

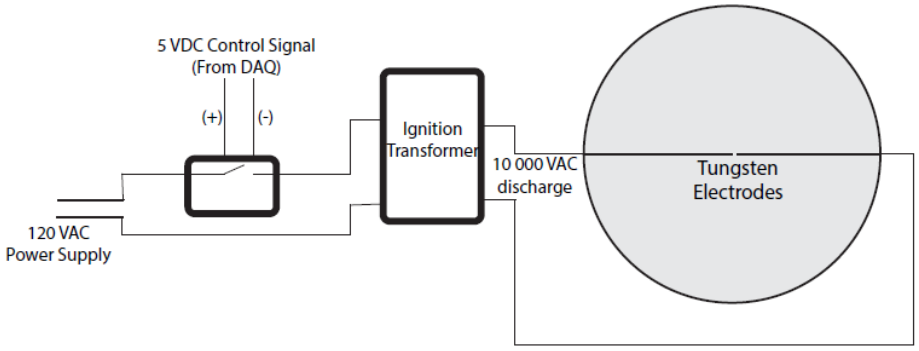

Figure 4.6. A schematic diagram of the ignition system

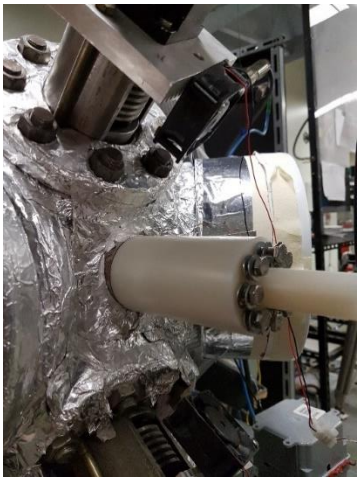

Figure 4.6. Electrode holder

4.6 Flame visualization and image processing

Schlieren photography is an imaging technique that is invented by the German physicist August Toepler in 1864. It is used to photograph the flow of fluids of variable densities by using a single light source which shines on or from behind a target object causing a variation in the

refractive index and hence creating a spatial variation in the light intensity. In a previous section (Section 2.4), the Schlieren imaging technique was briefly introduced. In this section, more details are provided regarding Z-type Schlieren setup, system configurations, and image processing.

4.6.1 Schlieren imaging setup and configuration

Several Schlieren configurations were used in the literature depending on many factors such as the experimental setup, the space availability, and the objective of the imaging technique. However, the majority of these configurations adopted Z-type Schlieren setup. Thus, due to its simplicity and ease of use, this configuration (Z-type) was employed in this thesis for tracking and recording the flame evolution. The Schlieren setup (see Figure 4.8) consists of a Nanosence MKIII high-speed CCD camera, a pair of spherical mirrors, a LED light source, and a knife edge. These parts are described in detail as follows [50]:

- A single LED spotlight source of 1.8 mW/cm^2. It is an advanced Illumination model SL4301-WHIIC providing white light with UV compatibility (Figure 4.9).
- Two aluminized spherical mirrors of 6” (152.4 mm) diameter, 60” (1.524 m) focal point and λ/8 high surface accuracy (a measurement of the deviation between the actual and the intended shape of the optical surface) (Figure 4.10).
- A CMOS high-speed camera Nanosense MKIII capable of up to 1040 fps at a full resolution of 1280 pixels x 1080 pixels (Figure 4.11).
- A sharp blade Knife edge (Figure 4.12).

In this configuration, the LED light source emits white light beams that travel towards the first spherical mirror which is located 45 inches apart on the same line. The reflected light beams from the first spherical mirror travel through the spherical chamber towards the second spherical mirror. At the focal point of the second mirror, the reflected light from the second mirror converges until it reaches the knife edge which cuts off the dark background light while the rest of the light continues towards the high-speed camera.

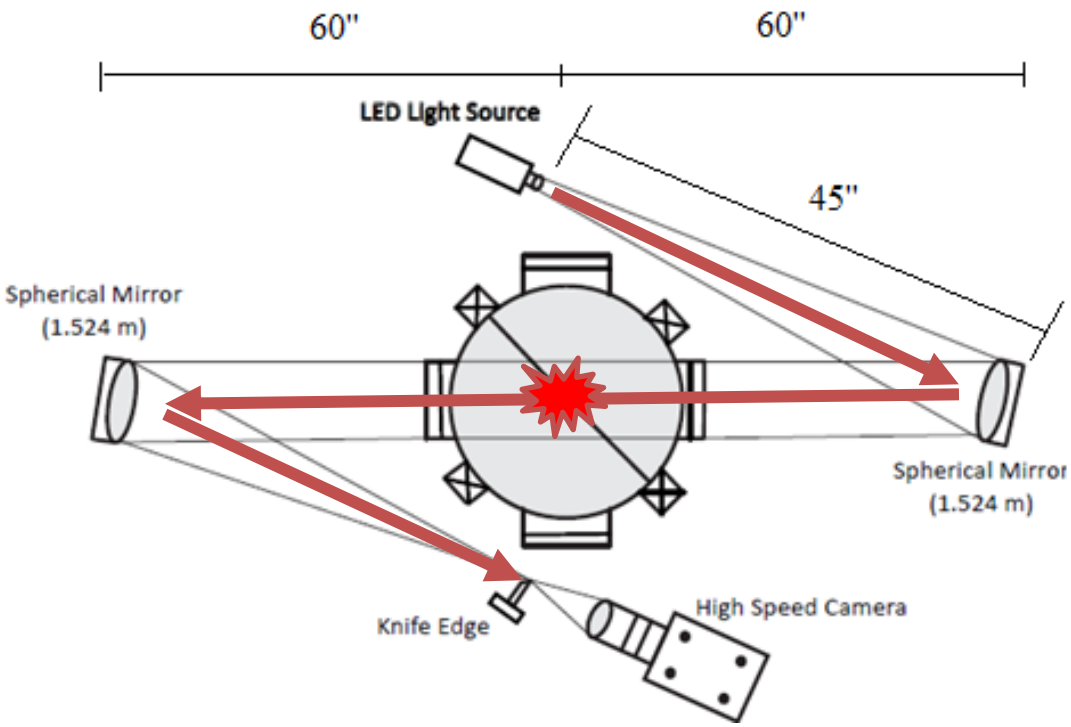

Figure 4.8. Schematic of the Z-type Schlieren imaging technique

Figure 4.7. LED light source

Figure 4.8. Spherical mirror

Figure 4.9. High-speed camera

Figure 4.10. Knife edge

Although using Schlieren imaging is relatively easier than applying other imaging techniques (Such as PIV), still many challenges were faced while setting up the system in the present thesis. For instance, both spherical mirrors, the LED light source, and the camera should all be on the same plane with the spark electrodes. On the other hand, the reflected parallel light beam from the first spherical mirror to the second one should coincide the circular surface of the second spherical mirror with the same diameter. Otherwise, the recorded image on the camera or the screen will show a non-circular field of view (elliptical). Moreover, the light beam coming from the second mirror through the knife edge and then the camera should be horizontally straight towards the camera lens centre, not deviated or tilted (should not reach the lens at an angle).

4.6.2 Image processing

The captured images by the high-speed camera are grey-scale with a maximum resolution of 1280 x 1024 $pixel^2$, and pixel intensity ranging between 0 (black) and 255 (white). Figure 4.13 shows some sequences of the recorded flame evolution captured by the high-speed camera from the time of ignition until the flame reaches the borders of the field of view.

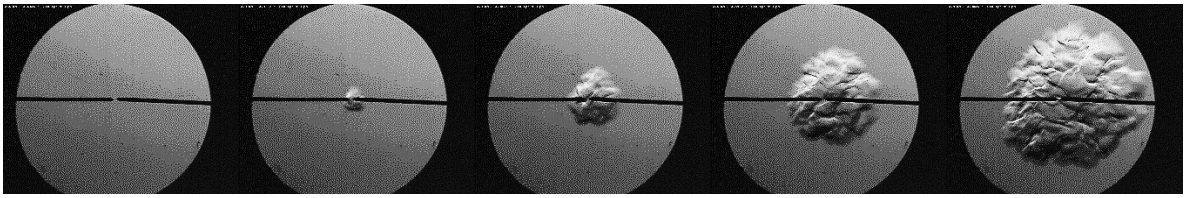

0 ms 4 ms 7 ms 10 ms 13 ms

Figure 4.11. Grey-scale images of the turbulent flame evolution recorded by the high-speed camera

Note that the high-speed camera can reach a higher frame per second (up to 2300 fps) but at a reduced image resolution (240 × 240). This can increase the number of captured images in each experiment. However, these images will be of low quality and hence can impair the accuracy of image processing especially when the flame is ignited at high turbulence levels. Thus, to avoid this issue, the high-speed camera configuration was setup for 1040 fps at a maximum resolution of 1280 x 1024 $pixel^2$. This camera configuration narrowed the explored test conditions in terms of turbulence intensity (i.e., up to 1.5 m/s)

The first step in measuring the turbulent burning velocity is to process the recorded propagating flames. This is accomplished using an in-house image processing MATLAB code (see Appendix A for details). The objective of this code is to measure the average radius of a circle equivalent to the flame front area following the method proposed by Bradley et al. [42]. This is achieved by determining the flame front area enclosed in the flame edge by turning it into a white region (white pixels, indicating the flame front area) backgrounded by dark pixels (indicating the unburned gases) as shown in Figure 4.14.

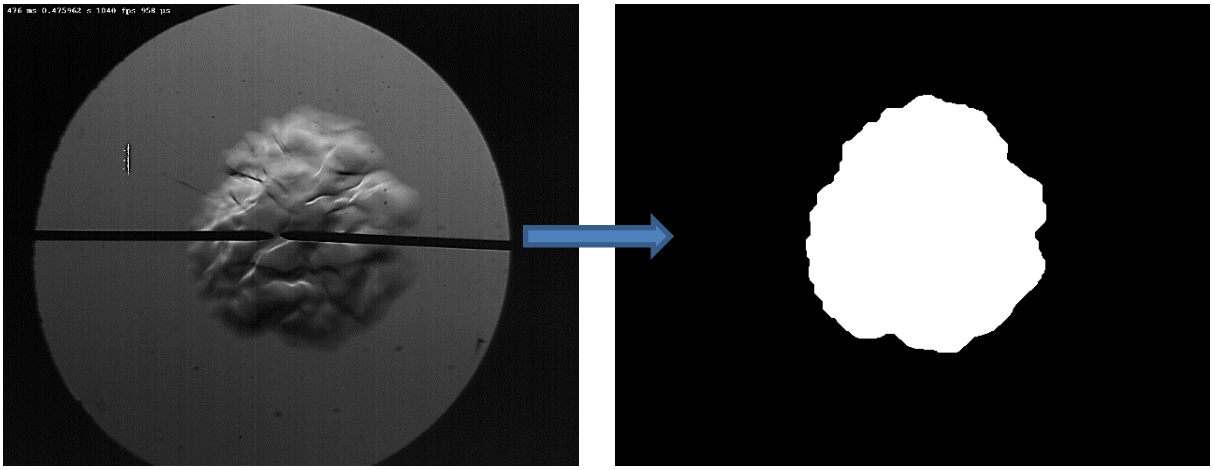

Original grey scale image Flame front after image processing

Figure 4.12. A grey-scale turbulent flame image and the finalized image with a white flame front

Detailed MATLAB image processing procedure is as follows:

- As previously mentioned, the objective of the knife edge was to cut off the dark background light contained in the light beam coming from the flame region. This led to highlighting the flame edge through expressing the density gradient between the burned and unburned gases. However, as the horizontal knife has a straight edge, the cut from the dark background occurred on the side that the light beam is blocked by the knife edge, which is the lower side of the flame kernel. On the upper side of the flame kernel, the opposite happens. This allowed the brighter light beams to access through the knife edge.
- To start image processing, the captured grey-scale flame images were first subtracted from the background reference image (without the presence of flame; Fig. 4.15 (a)). The same reference image (Fig. 4.15 (a)) was also subtracted from the flame image (Fig. 4.15 (b)), thus creating two grey scale images, each representing one-half of the detected

flame. Afterwards, the two images were superimposed by applying a Union function (Fig. 4.15 (c)) which then transformed the grey-scale into black and white image scale by applying a threshold as shown in Fig. 4.15 (d).

- The resulted image (Fig. 4.15 (d)) was filtered from noise and parasite, while the gaps inside the flame front were filled and recovered by applying 'Filling' and other morphological functions (Fig. 4.15 (e)).
- Finally, more morphological and filtering functions were applied to the recovered flame image (Fig. 4.15 (e)) without affecting or modifying the geometry of the flame front. Figure 4.15 (f) shows the finalized image with a clear and well edge-detected turbulent flame front coloured in white pixels. A good agreement between the detected flame edge and the initial grey scale image can be observed.
- Figure 4.16 shows four selected flames of different shapes with finalized white-coloured images and their corresponding flame edge, each highlighted with a superimposed solid white line on the original raw image. All raw images and their corresponding white-coloured and flame edge images are observed from left to right. This shows that the image processing code accurately detected the flame front edge of each flame despite the complications or the structure of each flame. This confirms the methodology used in image processing of the captured turbulent flames.
- The MATLAB code measures the flame front area in $pixel^2$ by counting the number of white pixels. From this area, the flame radius is deduced (R_{sch}) in mm by applying a scale factor, which is then divided by the time elapsed from the onset of ignition. Thus, a turbulent flame displacement speed $^{d_{R_{sch}}}/_{dt}$ is obtained. Note that the scale factor is

calculated based on the actual electrode diameter (2.3876 mm) and the number of pixels corresponding to this diameter measured from the captured Schlieren image (which is equal to 17 pixels – this number varies according to each Schlieren setup and the distances between its components, camera focus magnitude, and the position of the light source with the camera); that is by dividing the electrode width measured in pixels over the real electrode width in mm.

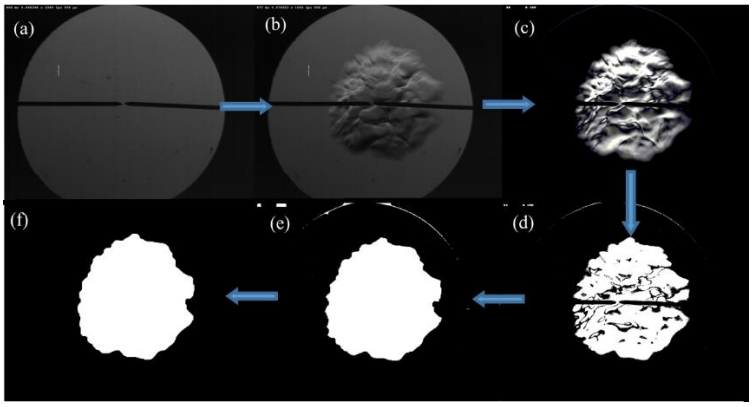

Figure 4.13. Image processing steps from a) raw grey-scale image to d) finalized flame front

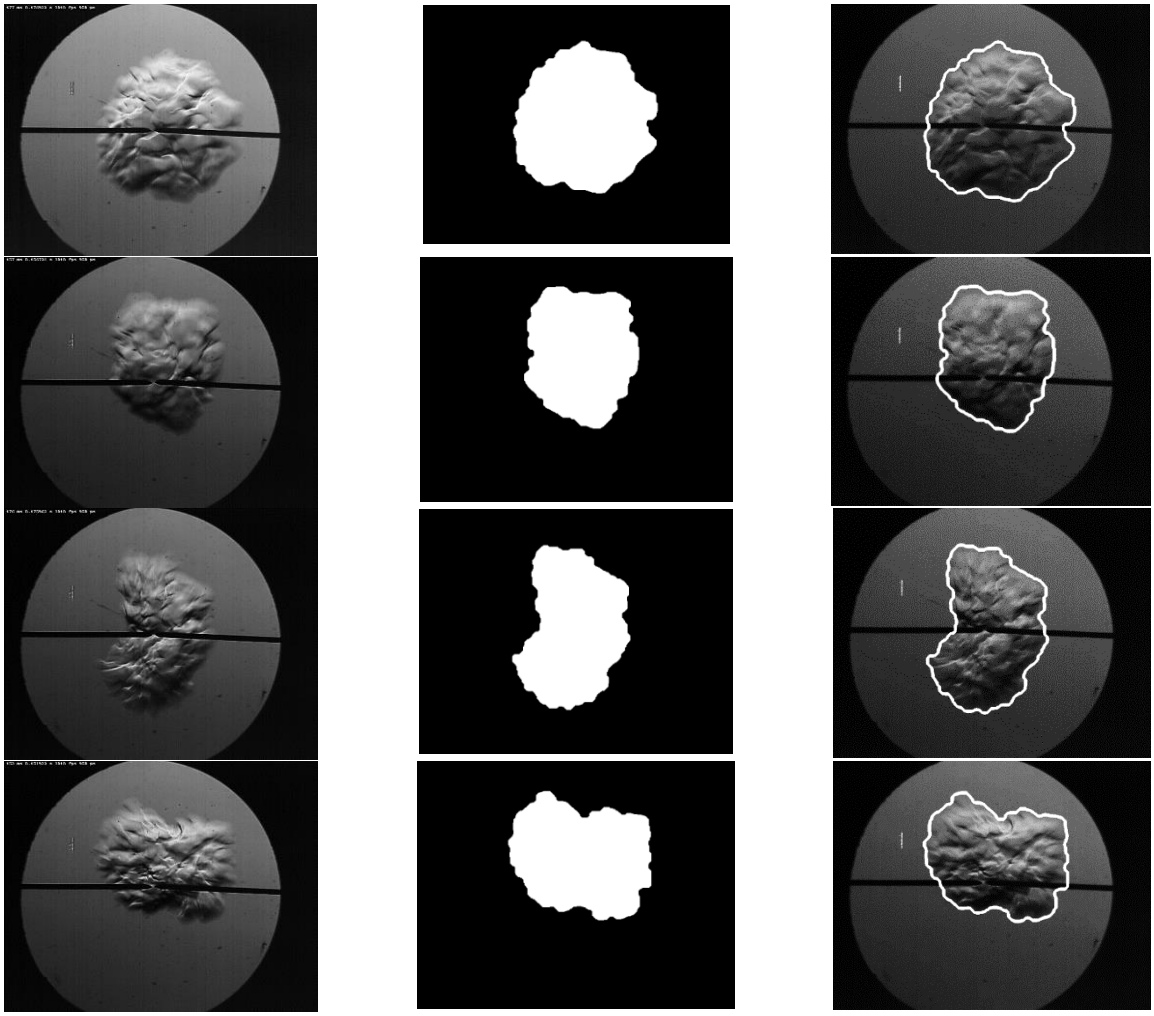

Figure 4.16 Grey-scale turbulent flame images with their corresponding finalized and edge detected images

4.7 Particle imaging velocimetry

A two-dimensional Dantec Dynamics PIV system was used for characterizing the turbulent flow field generated inside the central volume (with a diameter of ~ 80 mm) of the chamber. The system consists of a Dual Power 135-15 Nd: YAG laser and a FlowSense EO 4M camera capable of 15 frames per second at full resolution of 2048 X 2048 $pixel^2$. The laser repetition rate was 10 Hz for all runs. About 3000 pairs of images were found to be sufficient to provide satisfactory

convergence of turbulent statistics for the studied region, as the results were further validated by performing PIV measurements at 90 degrees with respect to the original layout. Olive oil particles of an average diameter of around 1 microns were used as seeding particles. Sufficient time was given between seeding and image capture to allow for dissipation of any transient flow effects caused by the influx of the seeding particle. An interrogation area of 32 pixels x 32 pixels with 50% window overlap was used for procesing of PIV pars of images. Further details are reported elsewhere [93].

CHAPTER 5 - RESULTS AND DISCUSSION

5.1 Introduction

Measurements of the biogas turbulent burning velocity are presented in this chapter. Investigated test conditions such as equivalence ratio, fuel composition, and turbulence intensity are given in Table 5.1. The results and discussion presented in this chapter are categorized into five sub-sections: turbulence characterization, validation of the methodology, biogas turbulent flames and their corresponding combustion regimes, development of the biogas flame radius and shape, and the behaviour of the turbulent burning velocity under the effect of fuel composition and turbulence intensity.

		Turbulence Intensity, u' [m/s]				
	Biogas	0.5	1.0	1.5	T [C]	P [psi]
Ø	50% CH_4 - 50 CO_2	0.6 - 1.1	0.6 - 1.1	0.7 - 1.1	24	14.7
	60% CH_4 - 40 CO_2	0.6 - 1.2	0.6 - 1.2	0.6 - 1.1	24	14.7
	70% CH_4 - 30 CO_2	0.6 - 1.2	0.6 - 1.2	0.6 - 1.2	24	14.7

Table 5.1. Fuel compositions and experimental conditions investigated in this work

5.2 Turbulence characterization

Characterization of the turbulent flow field at the centre of the spherical chamber at normal and elevated temperature and pressure conditions was reported elsewhere [92–94]. In this thesis, further PIV experiments were conducted at room temperature and atmospheric pressure to confirm previous turbulence characterization [92–94]. Figures 5.1 and 5.2 illustrate the magnitude of the 2D mean horizontal velocity field, $\overline{U}$ (which is nearly equal to the mean

vertical velocity, $\bar{V}$), at 500 RPM and 3000 RPM, respectively. The mean velocities, $\bar{U}\ and\ \bar{V}$, were subtracted from the instantaneous velocities U and V to determine the velocity fluctuations, u = U - $\bar{U}$ and v = V - $\bar{V}$, by which the root-mean-square values, U_{rms} and V_{rms}, were computed. As it was expected, the mean velocity, observed in Figs. 5.1 and 5.2, is almost quasi-zero in the central area of the chamber, while the highest speed values are found near the fans. However, one can also see that the lower fan rotational speed produced the smallest mean velocities, while as the fan speed was increased, the magnitude of the mean velocities became relatively larger. This increase in the mean velocities with the rotational fan speed is clearly illustrated in Figure 5.3. The same figure shows also a linear relationship between the turbulence intensity and the rotational fan speed. The turbulent intensity u', which is calculated as $u' = \sqrt{(2U_{rms} + V_{rms})/3}$ or $u' = \sqrt{(U_{rms} + 2V_{rms})/3}$ [56], represents the strength of the turbulent field inside the chamber. Since this turbulence was previously confirmed to be homogenous and isotropic [92–94], and because of the lack of data in the third dimension, it is assumed that $U_{rms} \approx V_{rms} \approx W_{rms}$. Thus, the use of the two equations mentioned above to calculate the turbulence intensity is reasonable. This was further confirmed by comparing the values of the two formulas where a good agreement was observed. Furthermore, the plotted relationship in Fig. 5.3 between the turbulence intensity and the rotational fan speed, N, showed a linear best-fit equation expressed as $u' = 0.000451 \times N$. This relationship is plotted for a radius of $35\ mm$ in the centre of the spherical chamber, which is enough for the turbulent burning velocity to propagate before exceeding the Schlieren high-speed camera field of view.

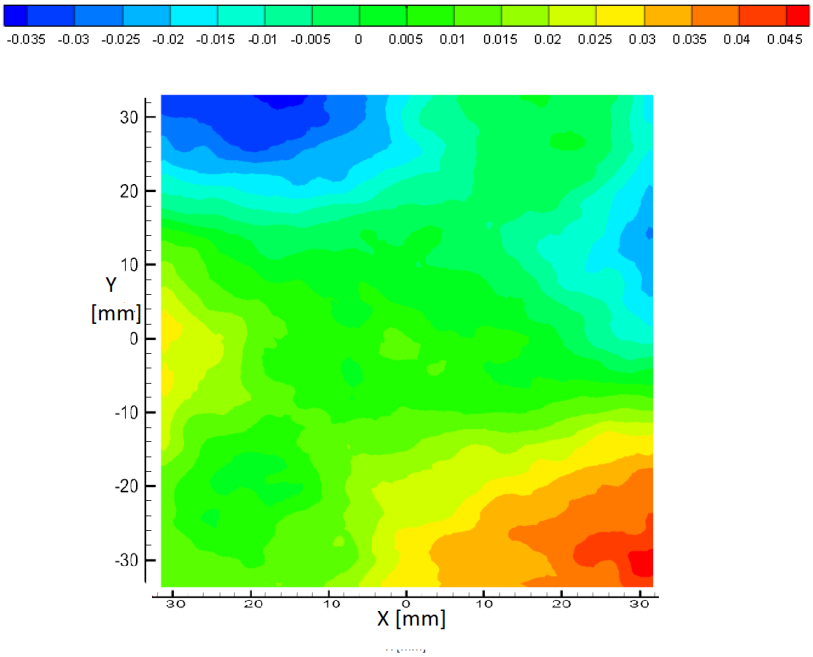

Figure 5.1. Mean velocity at 500 RPM within a field of view of 70 mm ×70 mm

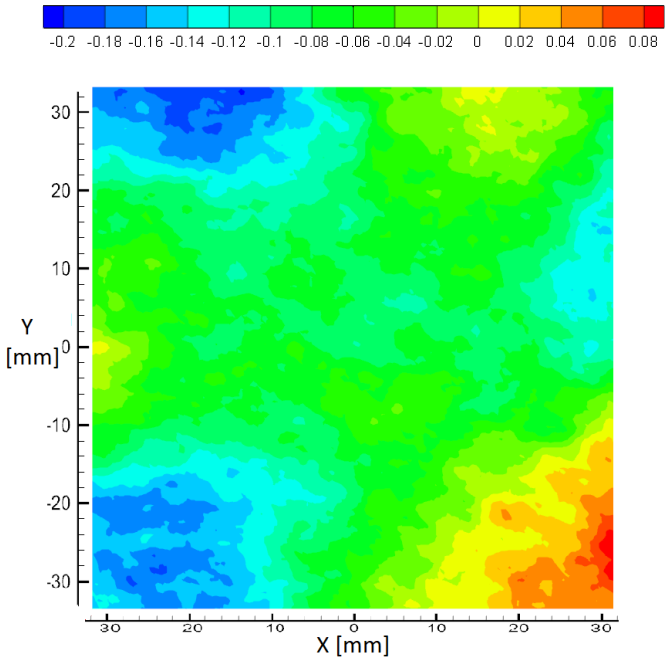

Figure 5.2. Mean velocity at 3000 RPM within a field of view

of 70 mm ×70 mm.

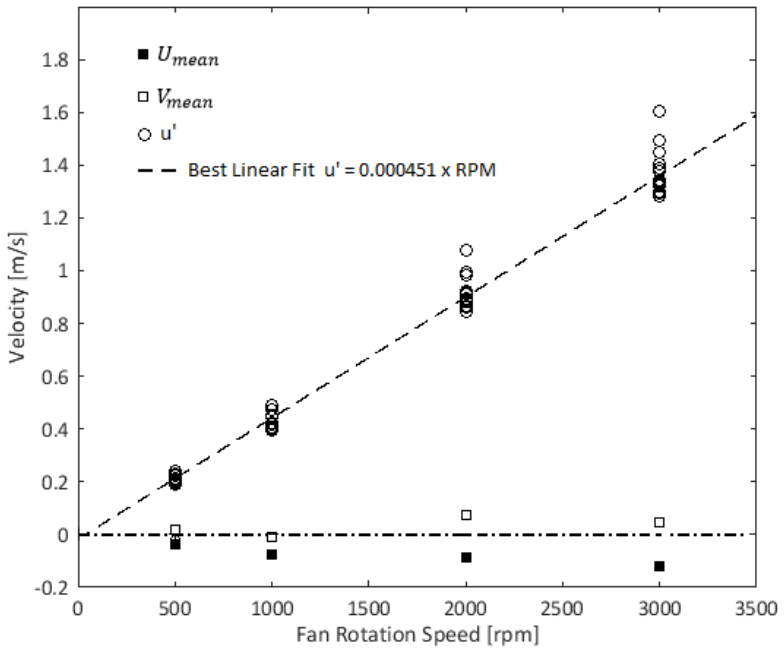

Figure 5.3. Variation of turbulent intensity, u', and the corresponding mean velocities (U_{mean} and V_{mean}) as a function of the fan rotational speed (rpm)

The homogeneity ratio defined as u'/u'_{avg}, and the isotropy ratio, defined as U_{rms}/V_{rms}, are plotted in Fig. 5.4. The horizontal lines 1.1 and 0.9 (10% unity) represent the range of the accepted ranges for turbulence to be considered nearly homogeneous and isotropic [95,96]. As can be seen, the turbulence inside the chamber is more isotropic at higher fan rotational speeds than at the lower ones. On the other hand, the homogeneity level is consistently within the 10% of the unity region especially for the right side of the horizontal axis. Therefore, the nearly isotropy and homogeneity levels inside the chamber can well cover the development of the turbulent flames for a spherical radius of 35 mm from the centre of the chamber.

The integral length scale L was obtained by integrating the two-point velocity correlation curves (section 2.4.1). However, the longitudinal and lateral correlation functions did not reach zero within the PIV imaging field of view. Therefore, we adopted the method of Ravi et al. [97], who used a decaying exponential function to extrapolate the correlation curve to zero, as shown in Figure 5.5 (Correlation curves for 500 and 3000 rpm, respectively). The average values of the calculated integral length scales are shown in Table 5.2. One can notice that these values (an average value, L ≅ 22 mm) showed independency on the fan speed.

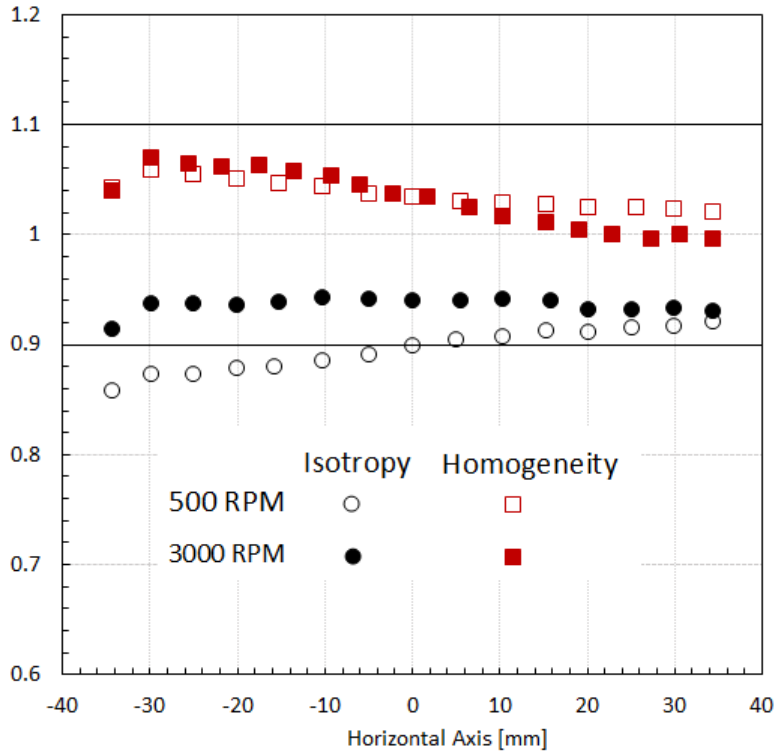

Figure 5.4. Variation of the isotropic and homogeneity ratio along the radial distance from the centre of the vessel at various fan speeds (rpm)

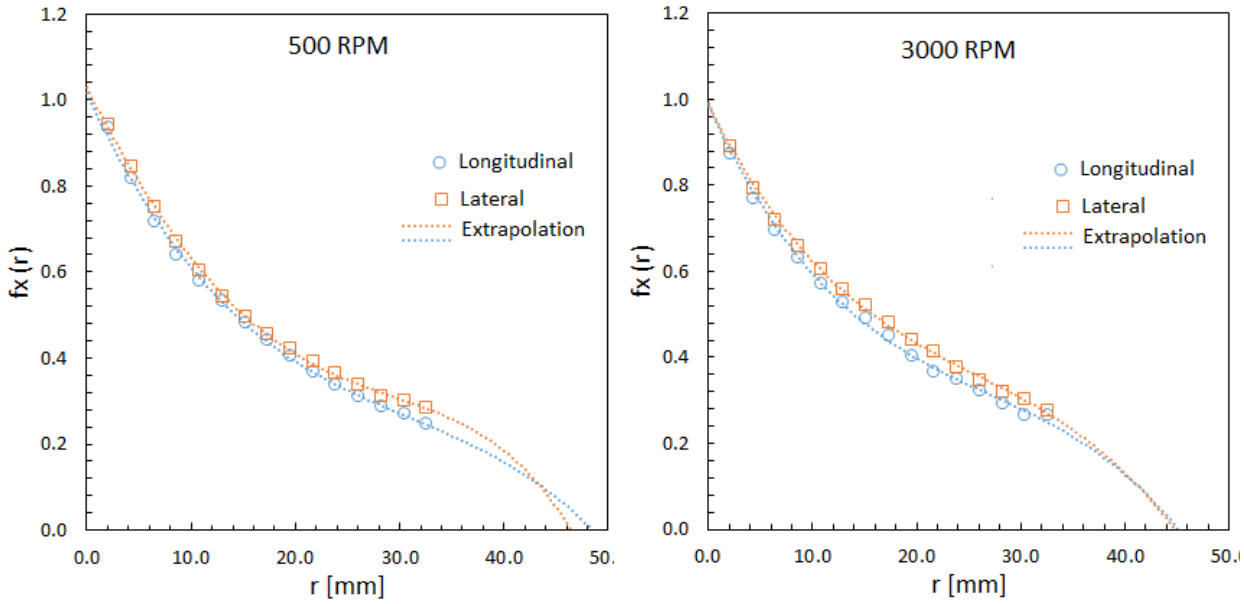

Figure 5.5. Correlation curves for fan speed 500 and 3000 rpm, respectively

Fan speed [rpm]	500	1000	2000	3000
L [mm]	21.83	22.37	20.4	22.14

Table 5.2. Integral length scale at different fan speed (at 298 K, 1 atm)

5.3 Validation of the experimental methodology

Since the turbulent burning velocity of biogas at standard temperature and pressure conditions is not covered in the literature, the experimental methodology was validated by burning methane-air mixture at stoichiometric equivalence ratio under standard pressure and temperature conditions over a wide range of turbulent intensity. Partial pressure methodology was used to determine the amount of fuel injected into the spherical chamber as described in section 4.3.1. The test conditions are summarized in Table 5.3. The measured values were compared with published experimental data measured by using similar experimental spherical

chambers [39,66,98,99], as shown in Figure 5.6. As one can see, the present measured burning velocities are in good agreement with published data except at turbulence intensity 1.25 m/s. This is due to the chaotic nature of turbulence where shot-to-shot variations in the obtained turbulent burning velocity prevail. That is, for each experiment, a different burning velocity can be determined but the difference remains within a narrow range. The discrepancies in the results from one study to another can also be due to the difference between the methodologies used in measuring the turbulent burning velocity (e.g., imaging techniques). For instance, Fairweather et al. [55] and Ravi et al. [59] used Schlieren imaging to obtain the turbulent burning velocity, while Bradley et al. [42] used Cine imaging technique. On the other hand, Tanoue et al. [100] measured the turbulent burning velocity using the pressure-rise technique. Therefore, despite the similarity of the experimental setups used in these studies, the different methodologies adopted for measuring the burning velocity might also contribute to some variation in the results.

u' [m/s]	**Fuel**	**Temperature [K]**	**Pressure [atm]**	∅
0.5	Methane	298	1.0	1.0
1	Methane	298	1.0	1.0
1.2	Methane	298	1.0	1.0
1.5	Methane	298	1.0	1.0

Table 5.3. Test conditions for methane-air mixture

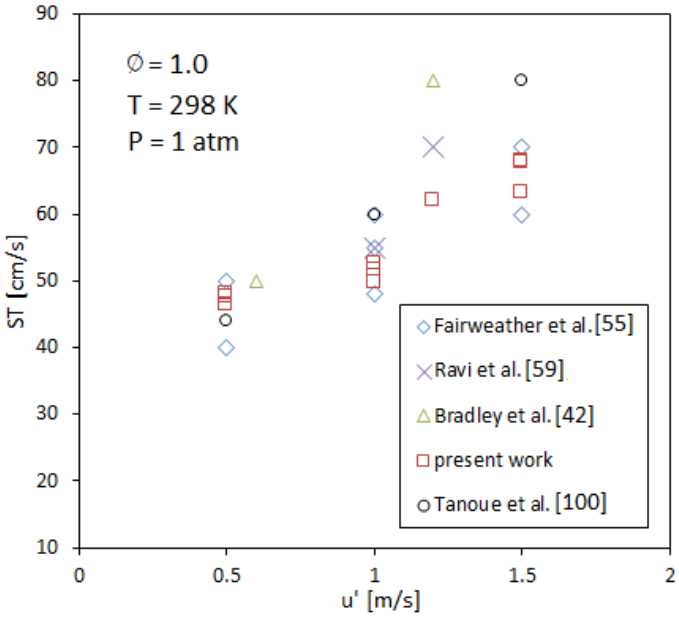

Figure 5.6. Turbulent burning velocity of methane-air mixture

5.4 Turbulent flames

5.4.1 Flame shape and combustion regimes

Two examples of turbulent biogas flames captured by the high-speed camera with the corresponding Borghi-Peters diagram for all tested equivalence ratios, fuel compositions, and turbulence intensities are plotted in Figures 5.7, 5.8, and 5.9 at a reference radius, R_{sch} = 35 mm (±4 mm). Flames with high convolution or convection, which did not reach the reference radius within the field of view, were shown with radii noted in the figure. At each condition, an average of three experiments was used depending on the quality of the captured flame. At some lean or rich mixture conditions, flame propagations were not successful which necessitated redoing the experiment five times. In other cases (especially at stoichiometric mixtures), as the generated

flames were consistent/repeatable, conducting two experiments was enough. Figure 5.10 shows the variation of the Da with equivalence ratio for all studied flames.

The corresponding Borghi-Peters diagram of each set of biogas flame conditions under three different turbulence intensities showed a consistent behaviour. All these points are located either in the flamelet Zone (Corrugated) or in the thin Reaction Zone (further explanation of the Borghi-Peters diagrams is presented in section 2.4.4). Thus, the inner flame structure was not affected by the turbulent fluctuations and remained quasi-steady with no influence on the chemical reactions or loss in radicals. However, under these turbulent conditions, the flame surface was affected by the small-scale eddies (Kolmogorov) which could penetrate the reactive-diffusive flame structure and wrinkle the flame surface. Moreover, as the turbulence intensity increased, Da decreased, which caused the flame conditions for the three biogas compositions to shift more towards the thin reaction zone (Borghi-Peters diagrams in Fig. 5.7-5.9). For instance, at low turbulence intensity (u' = 0.5 m/s), less wrinkled flames were observed for the three biogas compositions at stoichiometric mixtures (flames located on the far-left column in Figs. 5.7 to 5.9) with some other cases located in the lean and rich mixture conditions. When turbulence intensity increased (u' > 0.5 m/s), the flames became more wrinkled. This wrinkling was very significant for flames propagating under a turbulence intensity of 1.5 m/s for 50% CH_4 biogas composition (flames A16 to A23 in Fig. 5.7).

Nevertheless, despite the surface wrinkling, biogas flame kernels seen in Figures 5.7 - 5.9 experienced four different structures according to their equivalence ratio, turbulence intensity, and fuel composition. These structures are spherical, convected, local extinction, and quenched, all with less/more wrinkling at slower/faster fans speed.

Flames with a spherical appearance were mostly created at stoichiometric and near-rich equivalence ratios (i.e. $0.9 \leq \emptyset \leq 1.1$) for the three examined biogas compositions with some differences at high turbulence intensity. Examples of these flames can be seen in Fig. 5.7 (A6, A12); Fig 5.8 (B5, B24); and Fig. 5.9 (C6, C14). This spherical flame appearance confirmed Borghi-Peters diagram as the plotted conditions of the rich (star symbol) and stoichiometric mixtures (square symbol) were located within the corrugated flamelets where Da is much greater than 1. That is, the reaction time was relatively much smaller than the diffusion (section 2.4.4). However, other spherical flames could also be noticed at lean equivalence ratios ($\emptyset < 0.8$) for turbulence intensity of 0.5 m/s (e.g. Fig. 5.8, A1).

At leaner and richer mixtures, up to $\emptyset \leq 0.6$ and $\emptyset > 1.1$, respectively, most flames become either randomly convected or shifted away from the ignition centre which prevented the flame from developing more spherically. These flames could not reach the reference radius as they continued to develop outside the high-speed camera field of view. Examples of these flames are

shown in Fig. 5.7 (A10, A15), Fig. 5.8 (B8, B16), and Fig. 5.9 (C9, C18, and C21). Figure 5.11 (a) shows a typical enlarged shifted (convected) flame. Although these flames were experienced at both lean and rich conditions, local extinction of flames was mostly encountered at lean mixtures (Fig. 5.7, A9; Fig. 5.8, B19; and Fig. 5.9, C17) rather than rich (except for Fig. 5.8, B7). An enlarged image of the local extinction flame is shown in Figure 5.11 (b). The red circle shows the extinction region where two separated kernels seem to be weakly connected, suggesting that a re-ignition was occurred in this area due to unburned hot fuel/air pockets. Additionally, it was also noticed that all flames experiencing local extinction were convected away from the ignition centre. The occurrence of such flames, either convected or experienced local extinction, could be the results of two factors. First, at extreme equivalence ratios ($\emptyset < 0.8 \text{ and } \emptyset > 1.1$), the local flame propagation was significantly slower than the turbulent flow which caused the flame to move in the direction of the strongest flow. Secondly, as it was shown in Figure 5.10, Damkohler number exhibited a dramatic decrease as the fuel equivalence ratio shifted away from $0.9 < \emptyset < 1.1$ into lean mixtures, and reaching the minimum value (i.e. Da = 2.8) at an equivalence ratio of 0.6 for 50% CH_4 biogas composition. This implies that, at these conditions (lean rather than rich mixtures), the effect of turbulence (hence diffusion) was dominant over the chemical reactions which consequently caused the diffusion to reach an equilibrium well before the combustion (or chemical reaction).

Furthermore, 50-70% CH_4 biogas compositions at extreme lean (Ø<0.6) and rich (Ø>1.1) mixtures were very challenging to burn. Some of the flames experienced successful outwardly-propagation, while others quenched after a certain radius (did not reach the critical ignition radius). An example of the quenched flame is shown in Figure 5.11 (C). Figure 5.11 (d) shows a typical laminar flame (no turbulence) with least wrinkling, no extinction, and completely spherical. This flame shows how much difference the turbulence can make in the flame structure.

Note that flames which have non quasi-spherical shape (e.g., those in Fig. 5.7 (A2, A9, A10), Fig. 5.8 (B7, B8, B19), and Fig. 5.9 (C9, C10, C22)) were not used for determining turbulent burning velocity. The reason for the omission of such flames is that they do not obey the volume assumption, which states that turbulent propagating flame should be of spherical or semi-spherical structure despite/shape even when convected or convoluted.

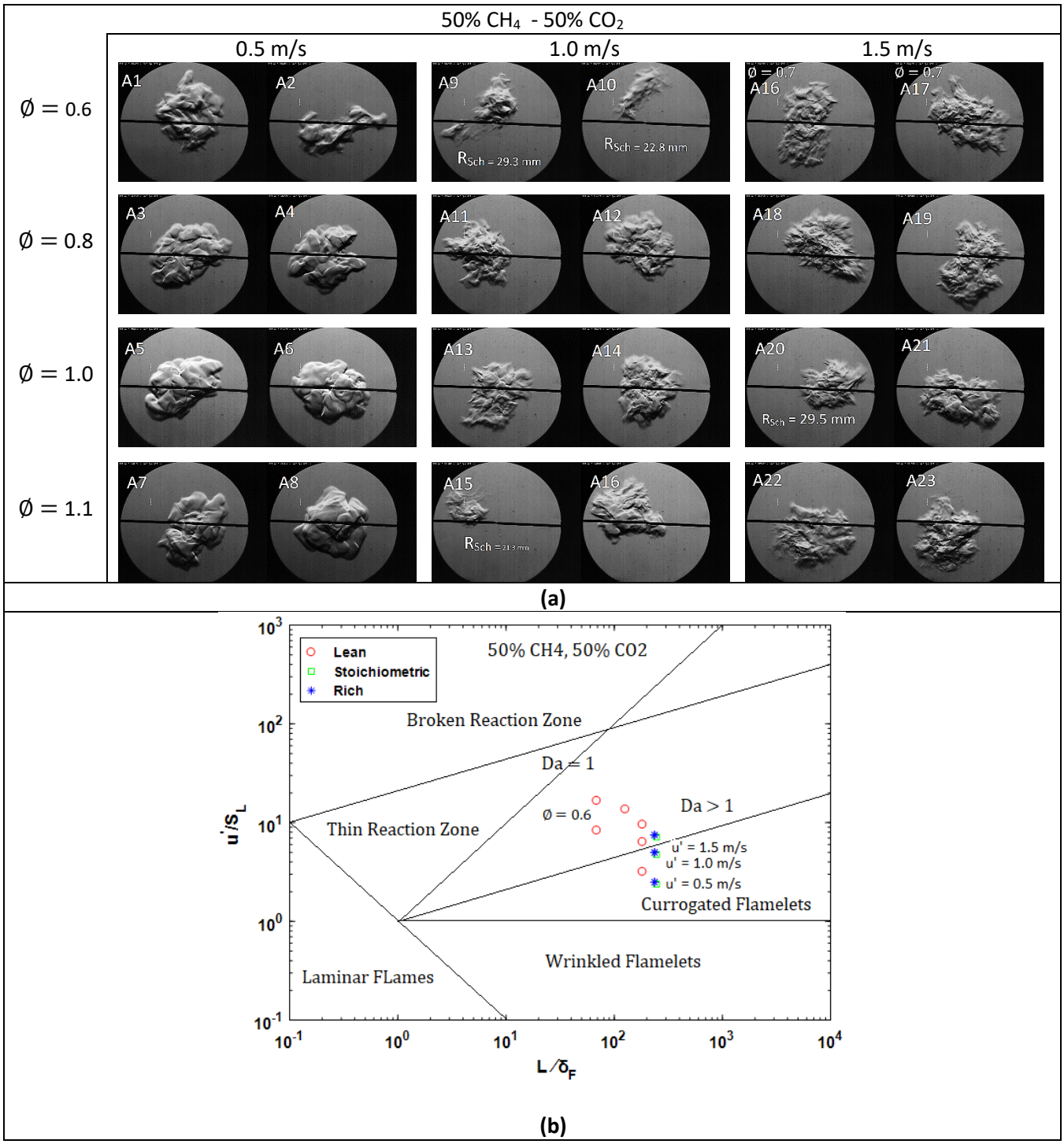

Figure 5.7. (a) Turbulent flame kernels and (b) Borghi-Peters diagram at R_{sch} = 35 mm ($\mp$ 4 mm) of the 50% CH_4 biogas composition over a range of equivalence ratios and turbulent intensities at standard pressure and temperature conditions.

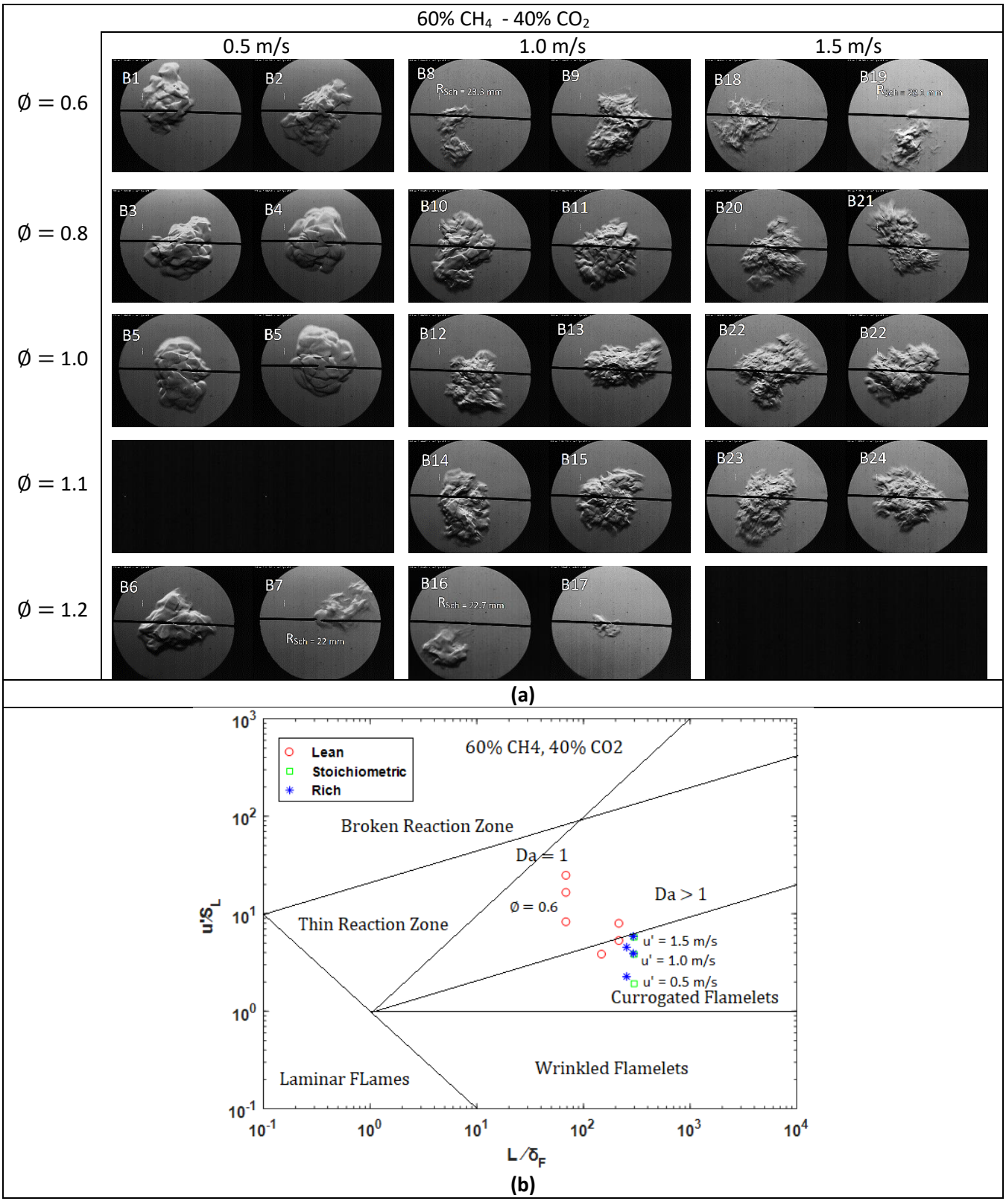

Figure 5.8. (a) Turbulent flame kernels and (b) Borghi-Peters diagram at R_{sch} = 35 mm (∓ 4 mm) of 60% CH_4 biogas composition over a range of equivalence ratios and turbulent intensities at standard pressure and temperature conditions.

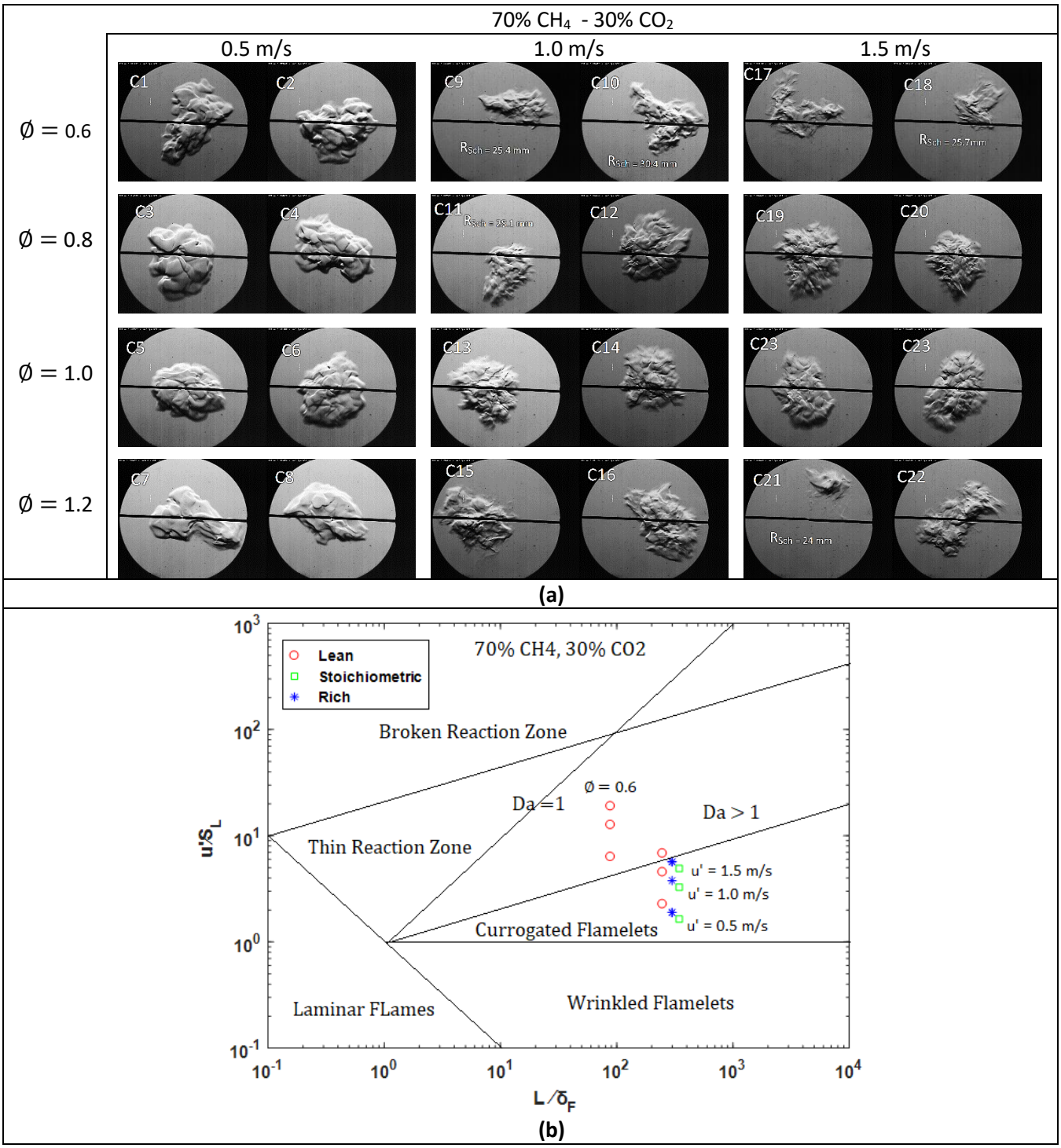

Figure 5.9. (a) Turbulent flame kernels and (b) Borghi-Peters diagram at R_{sch} = 35 mm ($\mp$ 4 mm) of 70% CH_4 biogas composition over a range of equivalence ratios and turbulent intensities at standard pressure and temperature conditions.

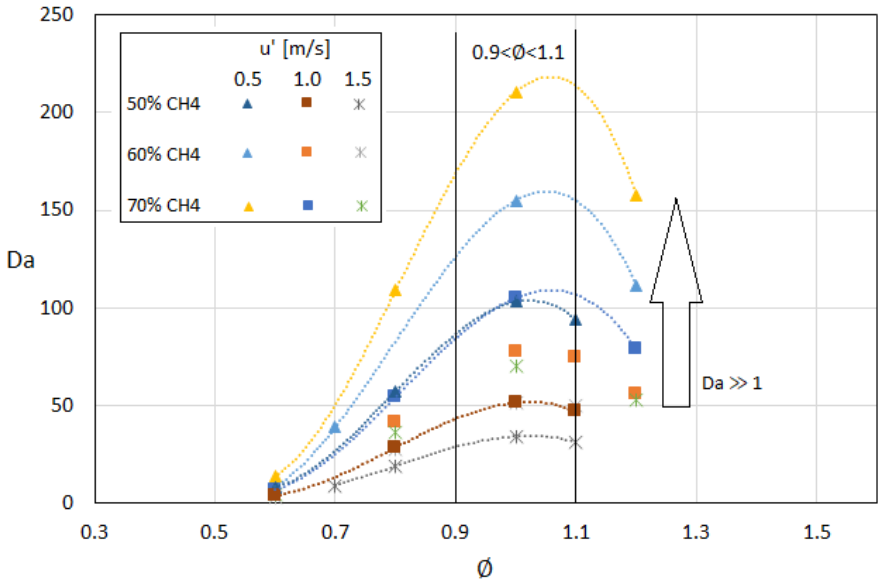

Figure 5.10. Evolution of Damkohler Number of biogas flame as a function of equivalence ratio.

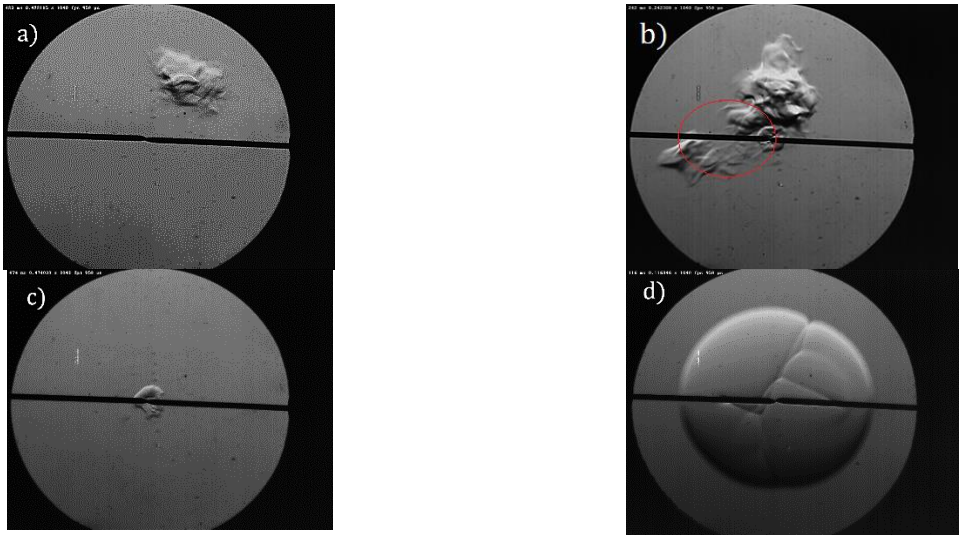

Figure 5.11. a) Convected flame b) Local extinction flame c) Quenched flame d) Laminar flame

5.4.2 Development of turbulent flames

Biogas turbulent flames tracked by the Schlieren high-speed camera were processed and the obtained instantaneous average flame radius was plotted versus time lapse from 2 ms after the ignition start time. Results are shown in Figure 5.12. As one can see, the variation of the flame radius with time exhibited an increasing slope for all studied cases, especially when u' was increased or when more methane was added.

The variation of the radius with time for the three biogas mixtures (50, 60, and 70% CH_4) at the stoichiometric equivalence ratio (Ø = 1.0) showed a larger slope than that of Ø = 0.8. As u' increased from 0.5 m/s to 1.5 m/s, slopes of the flame radius versus time for equivalence ratios of 1.0 and 0.8 became similar. By observing the slopes of the lean and rich mixtures (Ø = 0.6 and Ø $\geq$ 1.1, respectively) of both 50% and 70% CH_4 biogas compositions, the difference between the two slopes decreased as u' increased. For 60% CH_4 biogas composition, as u' increased, the two slopes of the rich ($\emptyset = 1.2$) and lean ($\emptyset = 0.6$) mixtures diverged. As the fuel mixture changed from stoichiometric to rich or lean, the relation of the flame radius with time became less linear.

Additionally, the turbulent burning velocities of the three tested biogas compositions and equivalence ratios are plotted in Figure 5.13 versus the flame radius. As the flame kernels are subjected to ignition effects, a bend-over in the measured turbulent burning velocity was observed for a radius up to 12 mm. Thus, all measured turbulent velocities prior to this radius were ignored, and only those of radius greater than 12 mm were considered.

Figure 5.13 shows a slight increase in the turbulent burning velocity for the three biogas mixtures (50-70% CH_4 biogas) at a turbulent intensity of 0.5 m/s, while a much greater increase

was observed at u' of 1.5 m/s for equivalence ratios of 0.8 and 1.0. At these two equivalence ratios, the derived turbulent burning velocities grew in a consistent and similar manner especially for 70% CH_4 biogas with a fastest burning velocity of around 55 cm/s (see Fig. 5.13, (i)). However, at u' = 0.5 m/s (see Fig. 5.13, (a), (d), and (g)), the more CH_4 was added to the fuel composition, the larger gap was observed between the two turbulent burning velocities within the range of equivalence ratio of 0.8 and 1.0, with the highest value at the stoichiometric mixtures ($\emptyset = 1.0$).

At lean mixtures, for 50% CH_4 biogas at turbulence intensities of 0.5 m/s and 1.0 m/s (Fig. 5.13 (a) and (b), respectively), the slowest turbulent burning velocity occurred at an equivalence ratio of 0.6. In all other cases, the burning velocity of rich mixtures ($\emptyset \geq 1.1$) exhibited the lowest rate compared to the 60%CH_4 biogas at u' = 1.5 m/s. The plots in Figures 5.13 f, h, and i correspond to the lean and rich mixtures ($\emptyset = 0.6 \text{ and } 1.2$) of the 60% CH_4 biogas at u' = 1.5 m/s, 70% CH_4 biogas at u' = 1.0 m/s, and 70% CH_4 biogas at u' = 1.5 m/s, respectively, did not only propagate at a constant rate but also decelerated during flame propagation. This decelaration in the flame propagation of the lean and rich mixtures is due to the influence of turbulence on slowing down the fuel chemistry. For instance, at the very lean and rich mixtures (see Fig. 5.10), Da becomes smaller and closer to unity. As explained in section 2.4.2, the smaller Da refers to the longer chemical time scales and consequently slower chemical reactions. Thus, as the flame propagation is promoted by the action of molecular diffusion of heat and mass, slow chemical reactions reduced flame propagation speed.

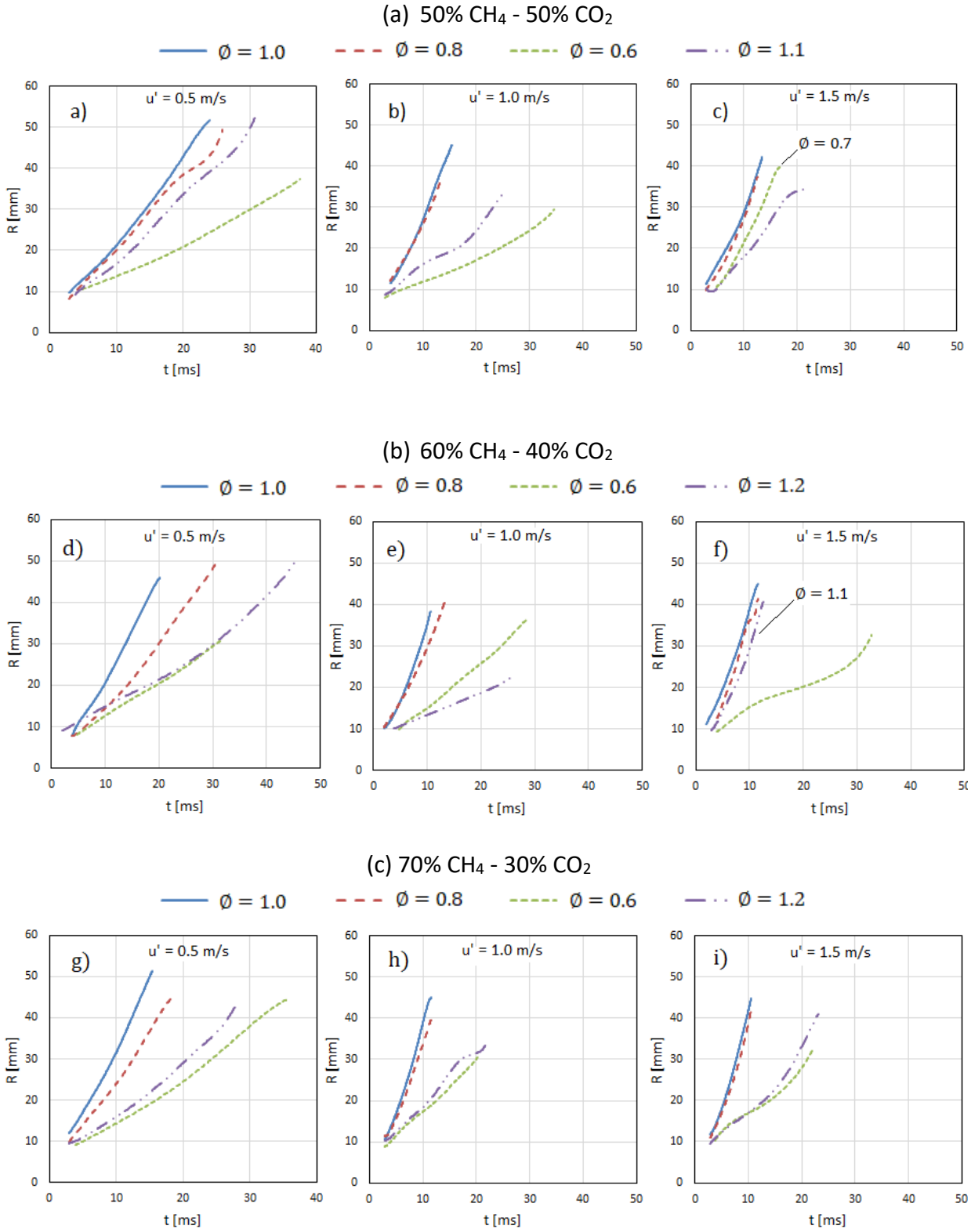

Figure 5.12. Variation of Schlieren flame radius of turbulent biogas flames versus time for different equivalence ratios, turbulent intensities and fuel compositions.

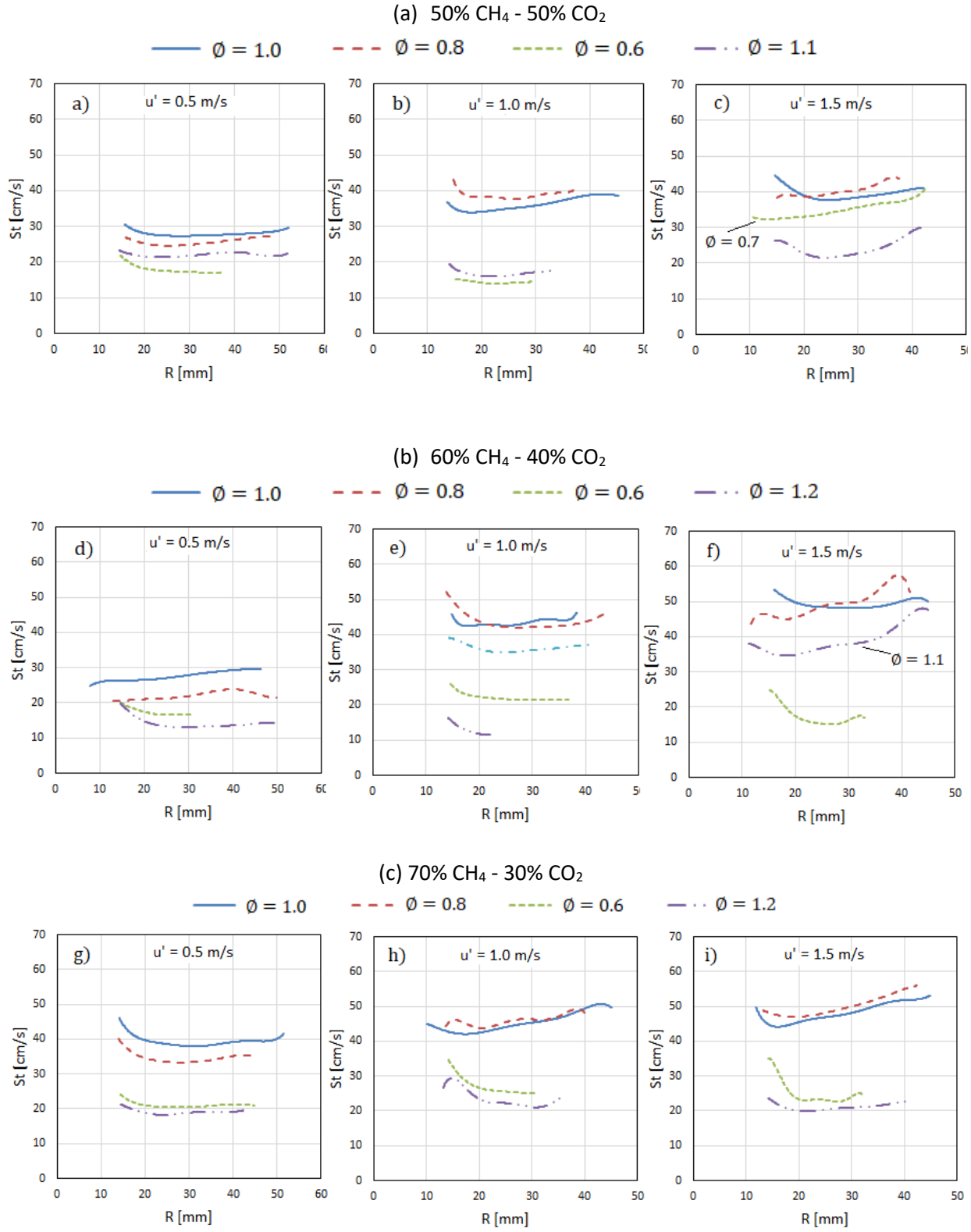

Figure 5.13. Turbulent burning velocities versus flame propagation radius for three different biogas compositions at different turbulent intensities and equivalence ratios.

5.5 Turbulent burning velocity

Results of biogas turbulent burning velocity for 50-70% CH_4 compositions under three turbulent intensities of 0.5, 1.0, and 1.5 m/s are presented and discussed in this section at a reference radius equal to 1.5 times the integral length scale (around 35 mm). The third order least square fits were used to generate the curves through each set of experimental data with a maximum standard deviation of ±4 cm/s. All experiments were conducted under standard ambient temperature and atmospheric pressure conditions. An average error of ±2.74% in the measured turbulent burning velocity was reported in Appendix C.

5.5.1 Effect of fuel composition

Figures 5.14, 5.15 and 5.16 show the biogas turbulent burning velocity for three biogas compositions at fixed turbulence intensity. For all compositions, the curve fits of the experimental data are "bell-shaped" with the burning velocity peaking at some equivalence ratios and diminishing at lower and higher ones.

At u' = 0.5 m/s (Figure 5.14), the 50% CH_4 biogas flame showed the slowest turbulent burning velocity, with a peak of 27.5 cm/s at Ø = 0.9. As more CH_4 was added, this peak in the burning velocity shifted slowly towards the stoichiometric equivalence ratio, reaching a burning velocity of 39 cm/s at Ø = 0.98 for 70% CH_4. Moreover, farther away from the peak, the burning velocity fits of both 50% and 60% CH_4 mixtures intersected at equivalence ratios of 0.7 and 1.1. For 70% CH_4, the lean and rich turbulent flames propagated faster than those of the 50% and 60% CH_4 by 5 cm/s.

For u’ = 1.0 m/s (Figure 5.15), besides the large increase in S_t for the three biogas compositions, the peak of the burning velocity also shifted (similarly to u’ = 0.5 m/s) from Ø = 0.9 for 50% CH_4 to Ø = 0.97 and 0.94 for both 60% CH_4 and 70% CH_4, respectively. On the other hand, the burning velocity curve fit of the 60% CH_4 was shifted away from that of the 50% CH_4 and became closer to that of the 70% CH_4. However, no much significant increase in the burning velocity was observed at both lean and rich equivalence ratios compared to biogas turbulent flames at u’ = 0.5 m/s.

In Figure 5.16, as u’ increased from 1.0 to 1.5 m/s, St recorded an average increase of 5 cm/s for the three biogas compositions. In addition, the turbulent burning velocity of the 50%, 60%, and 70% CH_4 compositions peaked, respectively, at Ø of 0.85, 0.88 and 0.9, compared to Ø of 0.9, 0.94 and 0.98 for the same compositions at u’ = 0.5 m/s. Moreover, the curve fit of the 60% CH_4 burning velocity nearly coincided the St curve fit of the 70% CH_4 composition showing a very similar burning velocity. On the other hand, the flammability limit of both 50% CH_4 and 60% CH_4 biogas compositions was reduced, respectively, to $0.7<Ø<1.1$ and $0.6<Ø<1.1$. Therefore, it was noticed that by adding more CO_2 (or reducing CH_4) to biogas surrogate, the turbulent burning velocity was decreased and the flammability limit was narrowed. This decrease in S_t and flammability limit was due to the dilution effect of CO_2, which has a higher heat capacity than methane [19,101]. Thus, an increase in CO_2 leads to more heat absorbed from the combustion reaction which reduces the adiabatic flame temperature [19,101]. Consequently, the chemical reaction produces fewer radicals which in return leads to lower burning velocity.

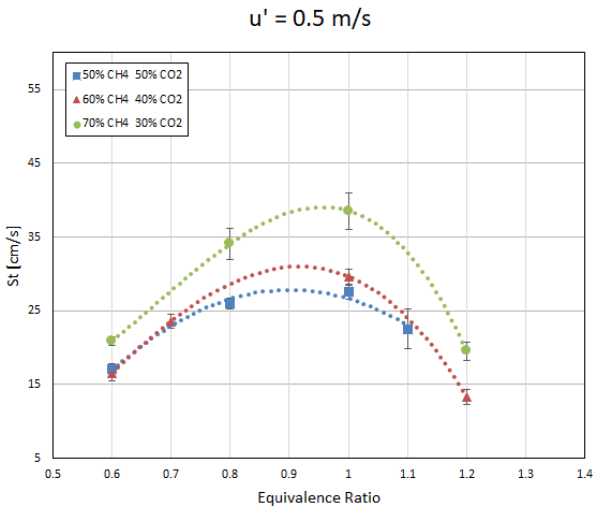

Figure 5.14. Biogas turbulent burning velocity versus equivalence ratio at u’ = 0.5 m/s

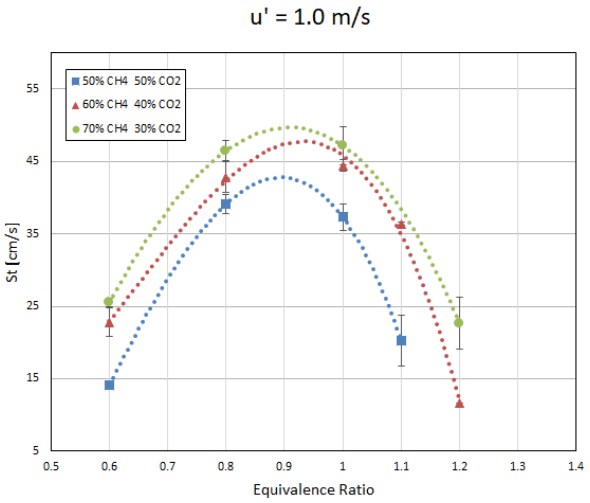

Figure 5.15. Biogas turbulent burning velocity versus equivalence ratio at u’ = 1.0 m/s

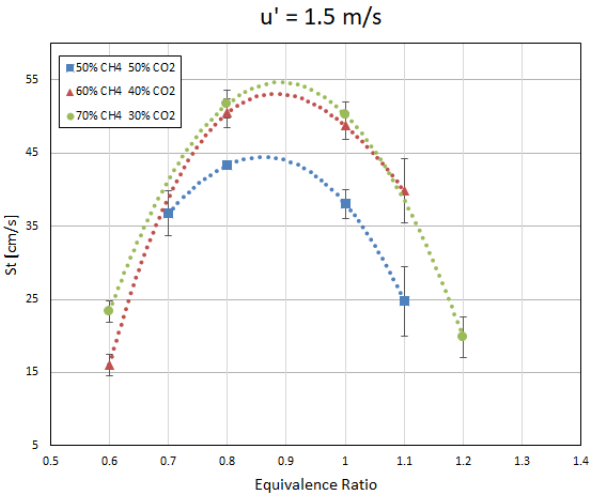

Figure 5.16. Biogas turbulent burning velocity versus equivalence ratio at u’ = 1.5 m/s

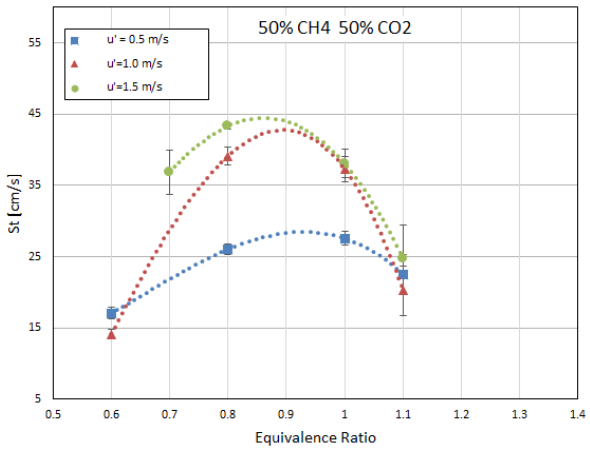

Figure 5.17. Biogas turbulent burning velocity versus equivalence ratio for 50% CH_4 – 50% CO_2

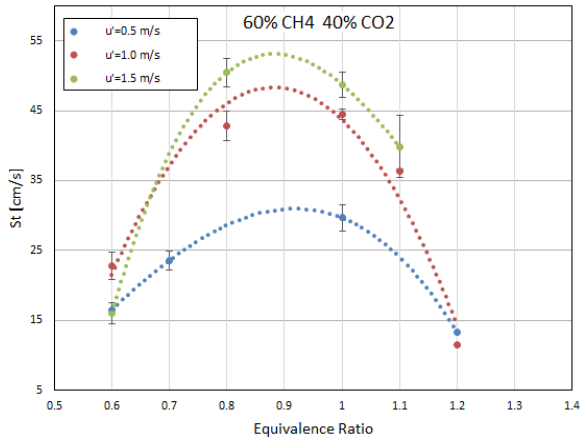

Figure 5.18. Biogas turbulent burning velocity versus equivalence ratio for 60% CH_4 – 40%CO_2

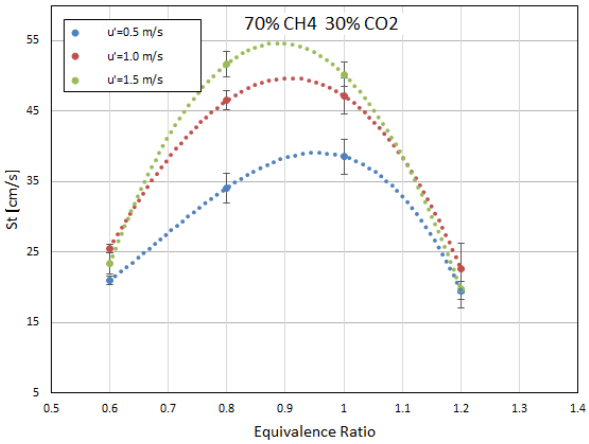

Figure 5.19. Biogas turbulent burning velocity versus equivalence ratio for *70% CH_4 – 30%CO_2*

5.5.2 Effect of turbulence intensity

Figures 5.17, 5.18, and 5.19 show the biogas turbulent burning velocity as a function of equivalence ratio for each biogas surrogate composition at three turbulent intensities 0.5, 1.0, and 1.5 m/s. As previously observed, the curve fits to the data were seen to be "bell-shaped" with the burning velocity peaking at some equivalence ratios and then falling as the fuel became leaner or richer.

As one can see from the 50% CH_4 biogas plot in Figure 5.17 that the slowest burning velocity was reached by the flames burning at the weakest turbulence intensity (0.5 m/s) with a maximum of 27 cm/s at Ø = 0.94. For the higher turbulence intensity (1.0 m/s), the burning velocity significantly increased by more than 15 cm/s for 0.8<Ø<1, peaking at Ø = 0.90 rather than Ø = 0.94 as for the 0.5 m/s turbulence intensity. However, the S_t values was decreased by 3 cm/s

for both the lean and rich mixtures. With further increase in the turbulence intensity from 1.0 m/s to 1.5 m/s, the flame burning velocity was not much affected for Ø>0.9. Whereas for Ø<0.9, an average increase of 5 cm/s was obsrved. The peak in the turbulent burning velocity continued to shift to the leaner side until reaching Ø = 0.85.

As more CH_4 was added (Figure 5.18), a noticeable enhancement in the burning velocity and flammability limit for the biogas mixture was observed particularly with the highest two turbulence intensities (1.0 m/s and 1.5 m/s). However, at these intensities, a large gap between the two burning velocity curve fits can be observed except at the very lean and rich equivalence ratios. Moreover, the peak in the turbulent burning velocity for turbulence intensities of 0.5, 1.0, and 1.5 m/s shifted, respectively, from Ø = 0.94 to Ø = 0.9 and then Ø = 0.88, exhibiting a similar behaviour to the S_t values of the 50% CH_4 biogas composition.

For the 70% CH_4 biogas (Figure 5.19), although the flammability limit for the mixture under the three turbulent intensities exhibited the widest range compared to the 60% and 50% CH_4 biogas compositions, where the enhancement in the turbulent burning velocity did not exceed 3 cm/s. Furthermore, the leaner and richer turbulent flames of the three biogas compositions propagated at similar burning velocities with a difference of ±5 cm/s between the fastest and the slowest ones. Additionally, the peak in the turbulent burning velocity for the turbulence intensities 0.5, 1.0, and 1.5 m/s occurred, respectively, at Ø = 0.97, 0.93, and 0.9. For the 50% CH_4 biogas composition, the same peaks took place at Ø = 0.94, 0.9, and 0.88. Thus, an increase in the turbulence intensity resulted in a shift in the burning velocity peak from the stoichiometric mixtures to the leaner ones. On the contrary, an increase in CH_4 in the biogas

composition resulted in a shift in the burning velocity peak from the leaner equivalence ratios to the stoichiometric.

5.5.3 Normalized turbulent burning velocity

Figure 5.20 presents the normalized turbulent burning velocity as a function of normalized turbulence intensity (both normalized by the laminar burning velocity). Because the available data of biogas turbulent burning velocity in the literature is quite scarce especially under standard room temperature and atmospheric pressure, biogas turbulent burning velocity data under elevated pressure and temperature [39,40] was also plotted in this figure for comparison purposes. Wang et al. [37] determined biogas turbulent burning velocity under conditions similar to the present thesis but by using a different fuel injection methodology. Nonetheless, all these studies used Bunsen burner, whereas the present study is conducted by using a spherical combustion chamber. Thus, discrepancies between the results of the present thesis and the literature can be expected. Moreover, as the turbulence intensity of the present study varied between 0.5 and 1.5 m/s, the available methane-air turbulent studies in the literature were mostly conducted for turbulence intensities between 1.5 m/s and 6 m/s. Due to the lack overlap in turbulence intensity, performing a direct comparison between the present biogas results and published methane-air was not considered.

Figure 5.20 shows an interesting behaviour of the normalized biogas burning velocity over the normalized turbulence intensity. As one can see, for biogas equivalence ratios between 0.8

and 1.1, most of the data is located in the same region where the turbulent burning velocity is about 1.5 to 3 times the laminar burning velocity for normalized turbulence intensities (u'/SL) below 10. As Wang et al. [37] conducted their experiments at similar equivalence ratios, an agreement in the normalized burning velocity can be noticed. However, due to the difference in the turbulence characterization of the experimental setups used in Wang et al.'s study and the present work, the normalized turbulence intensity of the present thesis exhibited a wider range than that of Wang et al. [37]. On the other hand, although the experiments of Bagdanavicius et al. [39] were conducted under elevated pressure and temperature conditions for lean and rich mixtures, their results showed a good agreement with the normalized burning velocity of the present thesis. Despite the difference in the methodologies used, Bagdanavicius et al. explained this behaviour by the competing influence of the pressure and temperature on both turbulent and laminar burning velocities. As the pressure increases, the local flame propagation decreases as well which causes both the laminar and turbulent burning velocities to decrease. On the Contrary, increasing the initial temperature causes the release of more radicals during the chemical reaction which increases the local flame propagation speed. Thus, combining both effects could lead to a weak improvement in the normalized burning velocity. It is worth to mention that the experiments of Bagdanavicius et al. are conducted at very lean and rich conditions, which might also be a reason for having low normalized burning velocity. This explanation is backed up by the results of Kobayashi et al. [40], as they conducted their experiments under similar conditions to those of Bagdanavicius et al. but at larger equivalence ratio ($\emptyset = 0.9$).

Furthermore, at leaner mixtures ($\emptyset < 0.7$), one can notice that the data is significantly shifted away from the near-stoichiometric mixtures ($0.8 < \emptyset < 1.1$) towards larger normalized burning velocities and turbulence intensities. As previously explained in the literature review (chapter 3), this behaviour at the lean biogas mixtures was due to the difference in the decrease rate of both laminar and turbulent burning velocities. Since biogas turbulent flames were significantly wrinkled by the small length scales, the area of these wrinkled flames compared to those of the laminar ones under the same equivalence ratio were much larger. This is clearly seen in equation (5.1) which relates St/SL to the effect of turbulence on the wrinkling of flame front area [88]:

$$St/SL = At/A_o \quad (5.1)$$

where A_t and A_o are the wrinkled and unwrinkled flame area, respectively. Therefore, as a decrease in the unwrinkled flame front area is much larger than that of the wrinkled one, the ratio of turbulent burning velocity to the laminar burning velocity becomes larger.

On the contrary, the rich biogas mixtures yielded the lowest normalized burning velocities with values below unity. At the same time, the normalized turbulence intensity was much lower than that of the very lean but more similar to the near-stoichiometric ones ($0.8 < \emptyset < 1.1$). To explain these low values, both laminar and turbulent burning velocity of biogas compositions were plotted in Figure 5.21. As it can be seen, the turbulent burning velocities of lean mixtures were much faster than those of the laminar ones for the same equivalence ratios ($\emptyset = 0.6$), confirming the relationship in equation 5.1. Furthermore, the turbulent burning velocities at the rich mixtures were either equal or smaller than those of the laminar ones, which explain the low

values of the normalized burning velocity for rich mixtures. However, at rich equivalence ratios, the laminar flames propagated at faster speeds than lean equivalence ratios. On the contrary, the turbulent flames propagated at similar speeds for both the rich and the lean equivalence ratios. This is explained by the effect of turbulence, and the CO_2 heat capacity. For instance, as the laminar flames experience no turbulence, the burning velocity at rich mixtures is only affected by the large amounts of CO_2 which absorb some of the heat from the combustion [19]. Nonetheless, biogas turbulent flames are affected by both CO_2 heat-absorbing and small turbulent scales [102]. Therefore, the turbulent burning velocity propagates at slower rates at rich conditions rather than at lean ones.

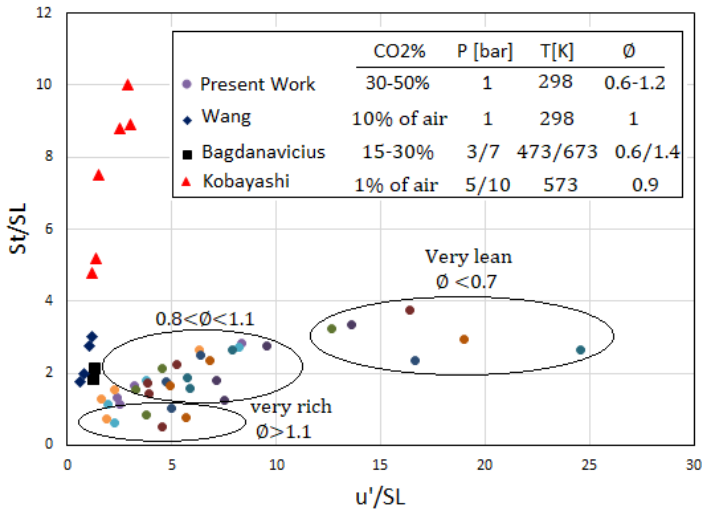

Figure 5.20. Relationship between turbulence burning velocity (St) and turbulence intensity (u') normalized with laminar burning velocity (SL)

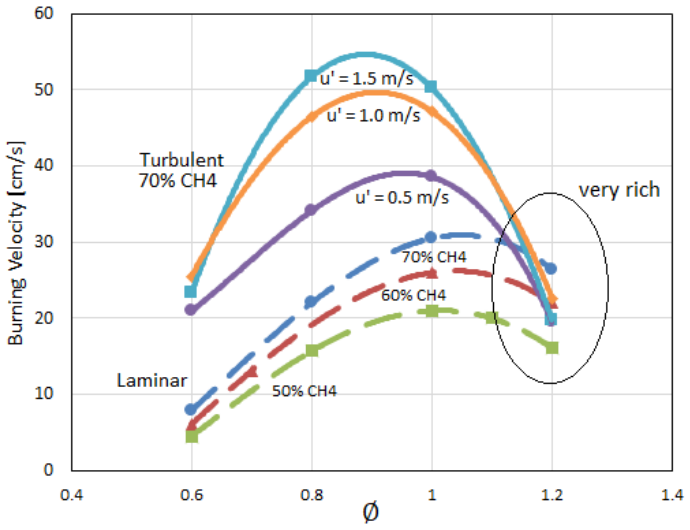

Figure 5.21. Turbulent and laminar burning velocity of biogas versus equivalence ratio

CHAPTER 6 - CONCLUSIONS AND RECOMMENDATIONS

6.1 Summary of findings and concluding remarks

The turbulent burning velocity of three biogas compositions (50%, 60%, and 70% CH_4 by volume) under the influence of various turbulence intensities (0.5 – 1.5 m/s) at standard room temperature and atmospheric pressure was investigated experimentally. Experiments were conducted using a fan-stirred spherical combustion chamber over an extended equivalence ratio in the range between the lower and the upper flammability limits. Schlieren imaging technique was employed to track the outwardly-propagating flames using a high-speed camera. An in-house developed MATLAB image processing code was developed to measure the flame front area and hence the turbulent burning velocity. A quasi-zero mean velocity with a good level of homogeneity and isotropy was characterized using a Particle Imaging Velocimetry (PIV) technique. An average of three tests of biogas turbulent flame at each test condition was conducted, with a total of 200 runs for the entire study. Each biogas surrogate mixture was injected into the chamber using the partial pressure methodology. All determined turbulent burning velocities in this study were taken at a reference radius of R_{sch} = 1.5 times the integral length scale. The main observations and findings of this study are presented as follows:

1. The nearly isotropic and homogeneous turbulence developed inside the chamber in a central spherical volume of a radius of about 40 mm is characterized as u’ = 0.000451×N. The integral length scale, based on two-point velocity correlation, was found approximately 22 mm.

2. The validation of the experimental setup and methodology was achieved by burning methane-air mixtures at stoichiometric equivalence ratio under standard pressure and temperature conditions over a wide range of turbulence intensity. A comparison with published data showed a good agreement except at turbulence intensity of 1.25 m/s.
3. The turbulent biogas flames plotted on Borghi-Peters diagram were either located in the flamelet region or the thin reaction zone, showing that the inner structure of the flames was not affected by the turbulent fluctuations and that the chemical reactions were not influenced. Moreover, increasing the turbulence intensity led to a further shift in the turbulent flame conditions towards the thin reaction zone, causing Damköhler number to decrease, and hence biogas flames become significantly wrinkled.
4. Biogas turbulent flames experienced four different structures based on equivalence ratio, turbulence intensity, and fuel composition. The first one is spherical, and it was mostly created at $0.9<Ø<1.1$ and a turbulence intensity of 0.5 m/s ($Da>>1$). The second flame structure is convected (shifted); and was created at lean and rich mixtures and mostly at high turbulence intensities for $Ø = 0.6$ and $Ø > 1.1$ ($1<Da<10$). The third flame structure, so-called “local extension”; was created at lean mixtures with some convection as well. The fourth flame structure is quenched; and the flame could not propagate at both very lean and rich mixtures.
5. The instantaneous average flame radius plotted against the time-lapse from the start of ignition showed an increasing slope for all studied cases especially when more methane was added or when the turbulence intensity was increased. Moreover, the largest slopes were observed for stoichiometric flames, while the slowest slopes were seen at lean

mixtures (Ø<0.7). Also, as the fuel composition shifted away from stoichiometric towards rich or lean, the variation of the flame radius with time became less linear.

6. The relation of the derived turbulent burning velocity with radius for 0.7<Ø<1.2 showed a monotonic increase with both turbulence intensity and methane addition. However, for the extreme lean and rich mixtures (Ø=0.6 and Ø=1.2, respectively), a deceleration in the burning velocity with radius was observed.
7. Third-order least square fits with a standard deviation of 4 cm/s were used to generate bell-shaped turbulent burning velocity curves plotted against the equivalence ratio. At the peak of the generated curve fits, the minimum burning velocity (27.5 cm/s) was obtained for the 50% CH_4 biogas composition under the weakest turbulence intensity. The fastest turbulent burning velocity (50 cm/s), on the other hand, was achieved for the 70% CH_4 biogas composition at u' = 1.5 m/s. Furthermore, at a fixed turbulence intensity, when more CH_4 was added to the mixture, the peak in the turbulent burning velocity shifted towards the stoichiometric equivalence ratio. On the contrary, when u' was increased from 0.5 to 1.5 m/s for the same biogas composition, the peak in the turbulent burning velocity shifted away from the stoichiometric equivalence ratio towards the leaner ones.
8. The turbulent burning velocity of biogas compositions for 0.8<Ø<1.1 was 1.5 to 3 times greater than the laminar velocity for normalized turbulence intensities lower than 10. On the other hand, the turbulent burning velocity of the rich mixtures (Ø>1.1) did not exceed its laminar counterpart.

6.2 Recommendations for future work

Further improvements in the methodologies used in this study and the experimental apparatus are suggested in this section. Although some of these suggestions are costly, studying the turbulent burning velocity of biogas over a wider range of turbulence intensities and elevated temperature and pressure conditions is required especially for validating numerical codes. These recommendations are summarized as follows:

6.2.1 Improvements in the experimental apparatus

- Despite the nearly homogeneous and isotropic turbulence generated at the centre of the spherical chamber, it was noticed that, by a simple visual inspection, the alignment of the symmetrically opposed-fans requires further improvement. This is believed to improve turbulence isotropy over an extended radius of the chamber.
- Although the leakage from the chamber was relatively meagre, further reduction in this leakage could lead to less uncertainty in the amount of the injected fuels into the chamber and hence improving the accuracy of the equivalence ratio.
- One of the most challenging issues we faced during this study was developing a proper ignition system. The previously developed system [50,103] used was a 10KV AC diesel ignition coil, which caused critical problems due to electrical current leakage and surge shocks. Although this system was successfully modified during the course of this thesis, it can further be improved. For instance, a high voltage pulse generator should be implemented, which can generate an ignition pulse in a minimal time period on the order

of nanoseconds. Thus, with such a short pulse, the early stages of the flame development will not be affected by the ignition energy.

- Interference of the electromagnetic field with the DAQ system has caused the system to stop working properly for some periods of time. In order to solve this issue, the DAQ and transducers wires should be shielded to eliminate the interference of the electrical and magnetic noise with the signals coming from the DAQ.
- At high turbulence intensities (over 1.5 m/s), the current high-speed camera could only capture a small number of flame images. Most of the captured images were blurred and not clear. Therefore, using a much higher frames-per-second (at least 3500 fps at full resolution) camera is necessary to investigate the turbulent burning velocity of biogas at higher turbulence intensities.
- During experiments, it was noticed that the chamber was not properly grounded. An advanced grounding system would make the system safer and more reliable.

6.2.2 Recommendations for further research

- Internal combustion engines operating at engine speeds larger than 1200 RPM can generate intense turbulence intensities of about 5 m/s [104]. to the best knowledge of the author, there is no data available in the literature about biogas turbulent burning velocity at this range of turbulence intensity. Therefore, biogas turbulent burning velocity should be investigated at high turbulent intensity.
- Although the turbulent burning velocity of biogas was investigated in the literature under elevated temperature and pressure conditions, the experimental setup used in these studies was Bunsen burner. This experimental setup, in contrary to the spherical

combustion chamber, does not have the ability to replicate realistic conditions of internal combustion engines. Therefore, a comprehensive investigation of the turbulent burning velocity of biogas under elevated temperature and pressure should be performed.

- Further investigation of the biogas turbulent flame structure and the effect of small turbulence scales on penetrating the flame internal layer is needed to understand the nature of the convected and locally extinguished flames.

REFERENCES

[1] A. Demirbas, *Progress and recent trends in biofuels*, Prog. Energy Combust. Sci. 33 (2007), pp. 1–18.

[2] *U.S Energy Information Administration, International energy outlook, DOE/EIA-0484(2017)*. Available at https://www.eia.gov/outlooks/ieo/pdf/0484(2017).pdf.

[3] N.L. Panwar, S.C. Kaushik and S. Kothari, *Role of renewable energy sources in environmental protection: A review*, Renew. Sustain. Energy Rev. 15 (2011), pp. 1513–1524.

[4] A. Evans, V. Strezov and T.J. Evans, *Assessment of sustainability indicators for renewable energy technologies*, Renew. Sustain. Energy Rev. 13 (2009), pp. 1082–1088.

[5] J.L. Walsh, C.C. Ross, M.S. Smith and S.R. Harper, *Utilization of biogas*, Biomass 20 (1989), pp. 277–290.

[6] *NNFCC Renewable Fuels and Energy Factsheet Anaerobic Digestion Nov 11 | Anaerobic Digestion | Biogas*. Available at https://www.scribd.com/document/252403062/NNFCC-Renewable-Fuels-and-Energy-Factsheet-Anaerobic-Digestion-Nov-11.

[7] R. Arthur, M.F. Baidoo and E. Antwi, *Biogas as a potential renewable energy source: A Ghanaian case study*, Renew. Energy 36 (2011), pp. 1510–1516.

[8] Z.A. Adnan, *Renewable power generation costs in 2012: An Overview*, IRENE REPORT/2013.

[9] T.B. Johansson and L. Burnham, *Renewable Energy: Sources for Fuels and Electricity*, Island press, 1993.

[10] B.J. Bora and U.K. Saha, *Comparative assessment of a biogas run dual fuel diesel engine with rice bran oil methyl ester, pongamia oil methyl ester and palm oil methyl ester as pilot fuels*, Renew. Energy 81 (2015), pp. 490–498.

[11] I.D. Bedoya, S. Saxena, F.J. Cadavid, R.W. Dibble and M. Wissink, *Experimental evaluation of strategies to increase the operating range of a biogas-fueled HCCI engine for power generation*, Appl. Energy 97 (2012), pp. 618–629.

[12] K. Sudheesh and J.M. Mallikarjuna, *Diethyl ether as an ignition improver for biogas homogeneous charge compression ignition (HCCI) operation - An experimental investigation*, Energy 35 (2010), pp. 3614–3622.

[13] A. Wellinger, J.D. Murphy and D. Baxter, *The Biogas Handbook: Science, Production and Applications*, Elsevier, 2013.

[14] S. McAllister, J.-Y. Chen and A.C. Fernandez-Pello, *Fundamentals of Combustion Processes*,

Springer, 2011.

[15] D.L. Zhu, F.N. Egolfopoulos and C.K. Law, *Experimental and numerical determination of laminar flame speeds of methane/(Ar, N2, CO2)-air mixtures as function of stoichiometry, pressure, and flame temperature*, Symp. Combust. 22 (1989), pp. 1537–1545.

[16] Y. Xie, J. Wang, M. Zhang, J. Gong, W. Jin and Z. Huang, *Experimental and numerical study on laminar flame characteristics of methane oxy-fuel mixtures highly diluted with CO2*, Energy and Fuels 27 (2013), pp. 6231–6237.

[17] X. Hu, Q. Yu and J. Liu, *ScienceDirect Chemical effect of CO 2 on the laminar flame speeds of oxy-methane mixtures in the condition of various equivalence ratios and oxygen concentrations*, Int. J. Hydrogen Energy 41 (2016), pp. 1–10.

[18] A. Di Benedetto, V. Di Sarli, E. Salzano, F. Cammarota, G. Russo, F. Ii et al., *Explosion behavior of CH 4 / O 2 / N 2 / CO 2 and H 2 / O 2 / N 2 / CO 2 mixtures*, Int. J. Hydrogen Energy 34 (2009), pp. 6970–6978.

[19] W. Anggono, I. Wardana, K.-J. Hughes, S. Wahyudi and N. Hamidi, *Laminar burning velocity and flammability characteristics of biogas in spark ignitied premix combustion at reduced pressure*, Appl. Mech. Mater. 376 (2013), pp. 79–85.

[20] N. Hinton and R. Stone, *Laminar burning velocity measurements of methane and carbon dioxide mixtures (biogas) over wide ranging temperatures and pressures*, Fuel 116 (2014), pp. 743–750.

[21] H.S. Zhen, C.W. Leung, C.S. Cheung and Z.H. Huang, *Characterization of biogas-hydrogen premixed flames using Bunsen burner*, Int. J. Hydrogen Energy 39 (2014), pp. 13292–13299.

[22] C.E. Lee, C.H. Hwang and H.Y. Lee, *A study on the interchangeability of LFG-LPG mixed fuels with LFG quality in domestic combustion appliances*, Fuel 87 (2008), pp. 297–303.

[23] V. Ratna Kishore, N. Duhan, M.R. Ravi and A. Ray, *Measurement of adiabatic burning velocity in natural gas-like mixtures*, Exp. Therm. Fluid Sci. 33 (2008), pp. 10–16.

[24] S. Zheng, X. Zhang, J. Xu and B. Jin, *Effects of initial pressure and hydrogen concentration on laminar combustion characteristics of diluted natural gas-hydrogen-air mixture*, Int. J. Hydrogen Energy 37 (2012), pp. 12852–12859.

[25] M. Ji, H. Miao, Q. Jiao, Q. Huang and Z. Huang, *Flame propagation speed of CO2 diluted hydrogen-enriched natural gas and air mixtures*, Energy & Fuels 23 (2009), pp. 4957–4965.

[26] Y. Ju, G. Masuya and P.D. Ronney, *Effects of radiative emission and absorption on the propagation and extinction of premixed gas flames*, Symp. Combust. 27 (1998), pp. 2619–2626.

[27] M. Elia, M. Ulinski and M. Metghalchi, *Laminar burning velocity of methane–air–diluent mixtures*, J. Eng. Gas Turbines Power 123 (2001), pp. 190.

[28] W. Qin, F.N. Egolfopoulos and T.T. Tsotsis, *Fundamental and environmental aspects of landfill gas utilization for power generation*, Chem. Eng. J. 82 (2001), pp. 157–172.

[29] Z. Chen, X. Qin, B. Xu, Y. Ju and F. Liu, *Studies of radiation absorption on flame speed and flammability limit of CO2 diluted methane flames at elevated pressures*, Proc. Combust. Inst. 31 II (2007), pp. 2693–2700.

[30] A.N. Mazas, D.A. Lacoste and T. Schuller, *Experimental and numerical investigation on the laminar flame speed of CH4/O2 mixtures diluted with CO2 and H2O*, ASME Turbo Expo 30 (2010), pp. 411–421.

[31] H.O.B. Nonaka and F.M. Pereira, *Experimental and numerical study of CO2 content effects on the laminar burning velocity of biogas*, Fuel 182 (2016), pp. 382–390.

[32] Z.L. Wei, C.W. Leung, C.S. Cheung and Z.H. Huang, *Effects of H2 and CO2 addition on the heat transfer characteristics of laminar premixed biogas–hydrogen Bunsen flame*, Int. J. Heat Mass Transf. 98 (2016), pp. 359–366.

[33] X. Hu, Q. Yu, J. Liu and N. Sun, *Investigation of laminar flame speeds of CH4/O2/CO2 mixtures at ordinary pressure and kinetic simulation*, Energy 70 (2014), pp. 626–634.

[34] C. Eon-Lee, C. BoOh, I.S. Jung and J. Park, *A Study on the determination of burning velocities of LFG and LFG-mixed fuels*, Fuel 81 (2002), pp. 1679–1686.

[35] C.E. Lee and C.H. Hwang, *An experimental study on the flame stability of LFG and LFG-mixed fuels*, Fuel 86 (2007), pp. 649–655.

[36] S.S. Shy, S.I. Yang, W.J. Lin and R.C. Su, *Turbulent burning velocities of premixed CH4/diluent/air flames in intense isotropic turbulence with consideration of radiation losses*, Combust. Flame 143 (2005), pp. 106–118.

[37] J. Wang, S. Yu, Y. Nie, W. Jin and Z. Huang, *Measurement on turbulent premixed flame structure of CH 4 / H 2 / air mixtures with CO 2 dilution*, SAE Technical Paper, 2015.

[38] S.S. Shy, Y.C. Chen, C.H. Yang, C.C. Liu and C.M. Huang, *Effects of H2 or CO2 addition, equivalence ratio, and turbulent straining on turbulent burning velocities for lean premixed methane combustion*, Combust. Flame 153 (2008), pp. 510–524.

[39] A. Bagdanavicius, P.J. Bowen, N. Syred, P. Kay, A. Crayford, G. Sims et al., *Burning velocities of alternative gaseous fuels at elevated temperature and pressure*, AIAA J. 48 (2010), pp. 317–329.

[40] H. Kobayashi, H. Hagiwara, H. Kaneko and Y. Ogami, *Effects of CO2 dilution on turbulent*

premixed flames at high pressure and high temperature, Proc. Combust. Inst. 31 I (2007), pp. 1451–1458.

[41] M. Fischer and X. Jiang, *An investigation of the chemical kinetics of biogas combustion*, Fuel 150 (2015), pp. 711–720.

[42] D. Bradley, M.Z. Haq, R. a. Hicks, T. Kitagawa, M. Lawes, C.G.W. Sheppard et al., *Turbulent burning velocity, burned gas distribution, and associated flame surface definition*, Combust. Flame 133 (2003), pp. 415–430.

[43] A.K.C.L. Au, D. Bradley and M. Lawes, *I Flame stretch rate as a determinant of turbulent burning velocity*, Phil. Trans. R. Soc. Lond. A 338 (1992), pp. 359–387.

[44] J.B. Heywood, *Internal Combustion Engine Fundamentals*, Mcgraw-hill, New York, 1988.

[45] N. Peters, *Turbulent Combustion*, Cambridge University Press, Cambridge, 2000.

[46] G.R.A. Groot, *Modelling of Propagating Spherical and Cylindrical Premixed Flames*, Technische Universiteit Eindhoven, 2003.

[47] K.J. Bosschaart, *Analysis of the Heat Flux Method for Measuring Burning Velocities*, Eindhoven, The Netherlands: Technische Universiteit Eindhoven, 2002.

[48] *Stephen Tse Research*. Available at http://coewww.rutgers.edu/~sdytse/research.html.

[49] C.J. Sung, B. Li, H. Wang and C.K. Law, *Structure and sooting limits in counterflow methane/air and propane/air diffusion flames from 1 to 5 atmospheres*, Symp. Combust. 27 (1998), pp. 1523–1529.

[50] C.A.G. Casanova, *Experimental Measurement of Laminar Flame Speed of a Novel Liquid biofuel 1-3 Dimethoxyoctane*, University of Manitoba (Canada), 2015.

[51] Z. Chen, M.P. Burke and Y. Ju, *Effects of Lewis number and ignition energy on the determination of laminar flame speed using propagating spherical flames*, Proc. Combust. Inst. 32 I (2009), pp. 1253–1260.

[52] S.Y. Liao, D.M. Jiang and Q. Cheng, *Determination of laminar burning velocities for natural gas*, Fuel 83 (2004), pp. 1247–1250.

[53] S. Zheng, X. Zhang, T. Wang and J. Liu, *An experimental study on premixed laminar and turbulent combustion of synthesized coalbed methane*, Energy 92 (2015), pp. 355–364.

[54] C. Mandilas, M.P. Ormsby, C.G.W. Sheppard and R. Woolley, *Effects of hydrogen addition on laminar and turbulent premixed methane and iso-octane-air flames*, Proc. Combust. Inst. 31 I (2007), pp. 1443–1450.

[55] M. Fairweather, M.P. Ormsby, C.G.W. Sheppard and R. Woolley, *Turbulent burning rates of methane and methane-hydrogen mixtures*, Combust. Flame 156 (2009), pp. 780–790.

[56] A. Hayakawa, Y. Miki, Y. Nagano and T. Kitagawa, *Analysis of turbulent burning velocity of spherically propagating premixed flame with effective turbulence intensity*, J. Therm. Sci. Technol. 7 (2012), pp. 507–521.

[57] A. Smallbone, K. Tsuneyoshi and T. Kitagawa, *Turbulent and stable/unstable laminar burning velocity measurements from outwardly propagating spherical hydrogen-air flames at elevated pressures*, J. Therm. Sci. Technol. 1 (2006), pp. 31–41.

[58] M. Lawes, M.P. Ormsby, C.G.W. Sheppard and R. Woolley, *Variation of turbulent burning rate of methane, methanol, and Iso-Octane air mixtures with equivalence ratio at elevated pressure*, Combust. Sci. Technol. 177 (2005), pp. 1273–1289.

[59] S. Ravi, A. Morones, E.L. Petersen and F. Güthe, *Effects of hydrogen addition on the flame speeds of natural gas blends under uniform turbulent conditions*, Vol. 4A Combust. Fuels Emiss. (2015), pp. V04AT04A066.

[60] O. Gulder, *Contribution of small scale turbulence to burning velocity of flamelets in the thin reaction zone regime*, Proc. Combust. Inst. 31 I (2007), pp. 1369–1375.

[61] F. Uriel, *Turbulence : The Legacy of AN Kolmogorov*, Cambridge University Press, 1995.

[62] D.C. Wilcox, *Turbulence Modeling for CFD*, Vol. 2, CA:DCW industries, 1998.

[63] J.O. Hinze, *Turbulence*, McGraw-Hill, 1975.

[64] J. Jarosinski, *The thickness of laminar flames*, Combust. Flame 56 (1984), pp. 337–342.

[65] F.T.C. Yuen, *Experimental Investigation of the Dynamics and Structure of Lean-Premixed Turbulent Combustion*, 2009.

[66] M. Fairweather, M.P. Ormsby, C.G.W. Sheppard and R. Woolley, *Turbulent burning rates of methane and methane-hydrogen mixtures*, Combust. Flame 156 (2009), pp. 780–790.

[67] T. Kitagawa, T. Nakahara, K. Maruyama, K. Kado, A. Hayakawa and S. Kobayashi, *Turbulent burning velocity of hydrogen-air premixed propagating flames at elevated pressures*, Int. J. Hydrogen Energy 33 (2008), pp. 5842–5849.

[68] S. Ravi, T.G. Sikes, A. Morones, C.L. Keesee and E.L. Petersen, *Comparative study on the laminar flame speed enhancement of methane with ethane and ethylene addition*, Proc. Combust. Inst. 35 (2015), pp. 679–686.

[69] L. Pizzuti, F. a Torres, R.W. Ferreira, L.R. Santos, P.T. Lacava and C. a Martins, *Laminar burning velocity and flammability limits in biogas : a atate of the art*, 10th Int. Conf. Heat

Transf. Fluid Mech. Thermodyn. (2014), pp. 98–107.

[70] K.T. Aung, M.I. Hassan and G.M. Faeth, *Effects of pressure and nitrogen dilution on flame/stretch interactions of laminar premixed H2/O2/N2 flames*, Combust. Flame 112 (1998), pp. 1–15.

[71] R.J. Kee, G. Dixon-Lewis, J. Warnatz, M.E. Coltrin and J.A. Miller, *A Fortran computer code package for the evaluation of gas-phase multicomponent transport properties*, Sandia Natl. Lab. Rep. SAND86-8246 13 (1986), pp. 80401–81887.

[72] A.K. Agarwal, *Biofuels (alcohols and biodiesel) applications as fuels for internal combustion engines*, Prog. Energy Combust. Sci. 33 (2007), pp. 233–271.

[73] G.H. Abd-Alla, *Using exhaust gas recirculation in internal combustion engines: a review*, Energy Convers. Manag. 43 (2002), pp. 1027–1042.

[74] R. Cited, O. City and R.U.-A. Data, *(12) United States Patent*, 1 (2003), pp. 0–4.

[75] R. Carroni, T. Griffin, J. Mantzaras and M. Reinke, *High-pressure experiments and modeling of methane/air catalytic combustion for power-generation applications*, Catal. Today 83 (2003), pp. 157–170.

[76] R. Stone, *Correlations for the laminar burning velocity of methane diluent air mixtures obtained in free-fall experiments*, Combust. Flame 114 (1998), pp. 546–555.

[77] C. Dong, Q. Zhou, X. Zhang, Q. Zhao, T. Xu and S. Hui, *Experimental study on the laminar flame speed of hydrogen/natural gas/air mixtures*, Front. Chem. Eng. China 4 (2010), pp. 417–422.

[78] E.C. Okafor, A. Hayakawa, Y. Nagano and T. Kitagawa, *Effects of hydrogen concentration on premixed laminar flames of hydrogen-methane-air*, Int. J. Hydrogen Energy 39 (2014), pp. 2409–2417.

[79] H. Miao, Q. Jiao, Z. Huang and D. Jiang, *Effect of initial pressure on laminar combustion characteristics of hydrogen enriched natural gas*, Int. J. Hydrogen Energy 33 (2008), pp. 3876–3885.

[80] X. Hui, C. Zhang, M. Xia and C.J. Sung, *Effects of hydrogen addition on combustion characteristics of n-decane/air mixtures*, Combust. Flame 161 (2014), pp. 2252–2262.

[81] C. Tang, Z. Huang, C. Jin, J. He, J. Wang, X. Wang et al., *Laminar burning velocities and combustion characteristics of propane-hydrogen-air premixed flames*, Int. J. Hydrogen Energy 33 (2008), pp. 4906–4914.

[82] J.P. Gómez-Montoya, K.P. Cacua-Madero, L. Iral-Galeano and A.A. Amell-Arrieta, *Effect of biogas enriched with hydrogen on the operation and performance of a diesel-biogas dual*

engine, CTyF - Ciencia, Tecnol. y Futur. 5 (2013), pp. 61–72.

[83] C. Jeong, T. Kim, K. Lee, S. Song and K.M. Chun, *Generating efficiency and emissions of a spark-ignition gas engine generator fuelled with biogas-hydrogen blends*, Int. J. Hydrogen Energy 34 (2009), pp. 9620–9627.

[84] K. Lee, T. Kim, H. Cha, S. Song and K.M. Chun, *Generating efficiency and NOx emissions of a gas engine generator fueled with a biogas-hydrogen blend and using an exhaust gas recirculation system*, Int. J. Hydrogen Energy 35 (2010), pp. 5723–5730.

[85] Z. Xin, X. Jian, Z. Shizhuo, H. Xiaosen and L. Jianhua, *The experimental study on cyclic variation in a spark ignited engine fueled with biogas and hydrogen blends*, Int. J. Hydrogen Energy 38 (2013), pp. 11164–11168.

[86] R. Kee, J. Grcar, M. Smooke, J. Miller and E. Meeks, *PREMIX : A FORTRAN program for modeling steady laminar one-dimensional*, SANDIA Natl. Lab. (1985), pp. 1–87.

[87] C. a. Cardona and A. a. Amell, *Laminar burning velocity and interchangeability analysis of biogas/C 3H8/H2 with normal and oxygen-enriched air*, Int. J. Hydrogen Energy 38 (2013), pp. 7994–8001.

[88] E. Hu, Z. Huang, B. Liu, J. Zheng and X. Gu, *Experimental study on combustion characteristics of a spark-ignition engine fueled with natural gas-hydrogen blends combining with EGR*, Int. J. Hydrogen Energy 34 (2009), pp. 1035–1044.

[89] E. Hu, Z. Huang, J. He, C. Jin and J. Zheng, *Experimental and numerical study on laminar burning characteristics of premixed methane-hydrogen-air flames*, Int. J. Hydrogen Energy 34 (2009), pp. 4876–4888.

[90] Y.J. Zhang, Z.H. Huang, L.J. Wei and S.D. Niu, *Experimental and kinetic study on ignition delay times of methane/hydrogen/oxygen/nitrogen mixtures by shock tube*, Chinese Sci. Bull. 56 (2011), pp. 2853–2861.

[91] C. Cohé, C. Chauveau, I. Gökalp and D.F. Kurtuluş, *CO2 addition and pressure effects on laminar and turbulent lean premixed CH4 air flames*, Proc. Combust. Inst. 32 II (2009), pp. 1803–1810.

[92] S. Fabbro, *An experimental test facility for studying the effects of turbulence on the evaporation of fuel droplets at elevated pressure and temperature conditions*, University of Manitoba (Canada), 2012.

[93] C.M. Verwey, *An experimental investigation of the effect of fuel droplet size on the vaporization process in a turbulent environment at elevated temperature and pressure*, University of Manitoba (Canada), 2017.

[94] S. Toth, *Experimental study of droplet vaporization and combustion of diesel, biodiesel and*

their blends in a turbulent environment at elevated pressure and temperature, University of Manitoba (Canada), 2014.

[95] J. Goulier, N. Chaumeix, F. Halter, N. Meynet and A. Bentaïb, *Experimental study of laminar and turbulent flame speed of a spherical flame in a fan-stirred closed vessel for hydrogen safety application*, Nucl. Eng. Des. 312 (2017), pp. 214–227.

[96] B. Galmiche, N. Mazellier, F. Halter and F. Foucher, *Turbulence characterization of a high-pressure high-temperature fan-stirred combustion vessel using LDV, PIV and TR-PIV measurements*, Exp. Fluids 55 (2014), pp. 1636.

[97] S. Ravi, S.J. Peltier and E.L. Petersen, *Analysis of the impact of impeller geometry on the turbulent statistics inside a fan-stirred, cylindrical flame speed vessel using PIV*, Exp. Fluids 54 (2013), .

[98] G. Tian, R. Daniel, H. Li, H. Xu, S. Shuai and P. Richards, *Laminar burning velocities of 2,5-dimethylfuran compared with ethanol and gasoline*, Energy and Fuels 24 (2010), pp. 3898–3905.

[99] J. Vancoillie, G. Sharpe, M. Lawes and S. Verhelst, *The turbulent burning velocity of methanol-air mixtures*, Fuel 130 (2014), pp. 76–91.

[100] K. Tanoue, H. Kido, T. Hamatake and F. Shimada, *Improving the turbulent combustion performance of lean methane mixture by hydrogen addition*, Seoul 2000 FISITA World Automot. Congr. (2000), pp. 1–6.

[101] D.A. Wilson and K.M. Lyons, *Effects of dilution and co-flow on the stability of lifted non-premixed biogas-like flames*, Fuel 87 (2008), pp. 405–413.

[102] D. Bradley, P.H. Gaskell, X.J. Gu and a. Sedaghat, *Premixed flamelet modelling: Factors influencing the turbulent heat release rate source term and the turbulent burning velocity*, Combust. Flame 143 (2005), pp. 227–245.

[103] C.A. Gomez Casanova, E. Othen, J.L. Sorensen, D.B. Levin and M. Birouk, *Measurement of laminar flame speed and flammability limits of a biodiesel surrogate*, Energy & Fuels 30 (2016), pp. 8737–8745.

[104] P.G. Hill and D. Zhang, *The effects of swirl and tumble on combustion in spark-ignition engines*, Prog. Energy Combust. Sci. 20 (1994), pp. 373–429.

[105] H.W. Coleman, W.G. Steele and H.W. Coleman, *Experimentation, Validation, and Uncertainty Analysis for Engineers*, John Wiley & Sons, 2009.

[106] R.J. Moffat, *Describing the uncertainties in experimental results*, Exp. Therm. Fluid Sci. 1 (1988), pp. 3–17.

[107] C. Morley, *Gaseq: a chemical equilibrium program for Windows*, Ver. 0.79/2005.

Appendix A – Image processing code

A.1. Introduction

An in-house MATLAB code was developed to process the recorded Schlieren outwardly propagating flames. This code is used for Schlieren images that are of reduced contrast because of the knife edge cut-off. This code can be easily modified to fulfil the modifications in the Schlieren system such as replacing the knife edge with a pin hole, changing the high-speed camera contrast, brightness, and or changing the image resolution. However, the threshold value should be carefully selected. For better performance, the captured Schlieren images should be of homogenous intensities.

A.2. MATLAB code

This MATLAB code is used for measuring the turbulent burning velocity by thresholding Schlieren grey-scale raw images. Inputs to this code include threshold values, electrode scale, electrode width (in mm), and the Schlieren images numbers as an array from the first image to the last one. After running this code, an array of the average turbulent flame radius should be displayed. By dividing the resulted flame radius array by the lapse time from the ignition start and then multiplying the result by the density ratio (Eq. (2.10)), the turbulent burning velocity can be deduced. Detailed image processing steps are mentioned in section 4.7.2.

```
clc
clear all
close all

%%%%%%%%%%%%%%%%%%                Initial Parameters                %%%%%%%%%%%%%%%%%%%%

  First_pic = 527 ;                  %%%% First processed image
  Last_pic  = 555 ;                  %%%% Last processed image
  thr1 = 6;                          %%%% thr = 5 for the lower half (typical threshold)
  thr2 = 6;                          %%%% the = 5 for the upper half (typical threshold)
  electrode_scale = 17;              %%%% Pixels for electrode width -sizing (17 is the typical value)
  electrode_width = 2.0363;          %%%% Real electrode width in mm
  sf = (electrode_scale/electrode_width).^2;   %%%% Electrode scale [pixel^2/mm^2]


%%%%%%%%%%%%%%%%%%              Background Image File              %%%%%%%%%%%%%%%%%%%%

  c =
imread('C:\Users\Public\Documents\IDT\MotionStudio\Images\TestSession\TestSession_534\Cam_1306060055_000522.tif');
  %imshow(c)

%%%%%%%%%%%%%%%%%%              Starting the code                  %%%%%%%%%%%%%%%%%%%%


    for k = First_pic:1:Last_pic          %%%% Starting loop for reading file
    kk = num2str(k);


filename =
strcat('C:\Users\Public\Documents\IDT\MotionStudio\Images\TestSession\TestSession_534\Cam_1306060055_000',kk,'.tif');
f = imread(filename);                  %%%% File Read from Destination



 %%%%%%%%%%%%%%%%%%    Subtracting the images and the background from each other    %%%%%%%%%%%%

  %imshow(f)
  d = c-f;                       %%%% Subtract background from flame image
  b = f-c;                       %%%% Subtract the flame image from the background
  %figure,imshow(d)
  %figure,imshow(b)              %%%% for knife edge


%%%%%%%%%%%%%%%%%%              Applying threshold                 %%%%%%%%%%%%%%%%%%%%
for i = 1:1024

  for j = 1:1280

    if d(i,j) > thr1
       d(i,j) = 255;
    else d(i,j) = 0;
    end
```

```
   end
end


for i = 1:1024                  % This part for the images obtained using knife edge

   for j = 1:1280

      if b(i,j) > thr2
         b(i,j) = 255;
      else b(i,j) = 0;
      end
   end
end


u = b | d;                      %%%% Union the two resulted images
%figure, imshow(u)

bw = im2bw(u,0.5);              %%%% Transform the grey scale image into BW
%figure,imshow(bw)


%%%%%%%%%%%%%%%%%%%%          An attempt to fill the gap resulted from the two electrodes          %%%%%%%%


for i = 490:540

   for j = 1:1280

      if bw(i,j)==1 && bw(i,j+1)==1 && bw(i,j+2)==1 && bw(i,j+3)==1 && bw(i,j+4)==1 && bw(i,j+5)==1 && bw(i+1,j)==0
&& bw(i+1,j+1)==0 && bw(i+1,j+2)==0 && bw(i+1,j+3)==0
         bw(i:520,j:567)=1;

         break
      end
   end
end


for i = 490:540

   for j = 1280:-1:1

      if bw(i,j)==1 && bw(i,j-1)==1 && bw(i,j-2)==1 && bw(i,j-3)==1 && bw(i,j-4)==1 && bw(i+1,j)==0 && bw(i+1,j-1)==0
&& bw(i+1,j-2)==0 && bw(i+1,j-3)==0 && bw(i+1,j-4)==0
         bw(i:540,j-10:-1:604)=1;

         break
      else
         continue
      end
   end
end


%%%%%%%%%%%%%%%%%%%%          Image Processing and Segmentation          %%%%%%%%%%%%%
```

```
    IMg1=imfill(bw,'holes');              %%%% first attempt to fill the holes and gaps
    %figure,imshow(IMg1)


    se = strel('disk',14);                %%%% filtering and smoothing
    imc = imclose(IMg1,se);
    %figure, imshow(imc)

    IMg2 = imfill(imc,'holes');           %%%% Second attempt to fill the holes and gaps
    %figure,imshow(IMg2)

    se2 = strel('disk',20);               %%%% filtering and smoothing
    imo = imopen(IMg2,se2);
    %figure,imshow(imo)

    final = imo(24:end,1:end);            %%%% crop
    %figure,imshow(final)

    final = imclearborder(final);         %%%% clear the image borders from any parasite
    figure,imshow(final)


%%%%%%%%%%%%%%%%%%              Flame area and radius calculations             %%%%%%%%%%%%%%%


    kkk = k - First_pic +1 ;
    Tot(kkk) = sum(sum(final));
    Area = Tot;                             %%%% Flame front area
    radius = (Area/(pi*sf)).^(0.5);         %%%% Flame front radius

    bw = bw(24:end,1:end);
    %figure, imshow(bw)

    %figure,imshow(bw | final)

    end

   Radius = radius'                         %%%% Flame front radius array
```

Appendix B – Procedure of operations

B.1. List of components

The following is the list of the configured components used for the turbulent burning velocity experiments:

- A spherical Combustion Chamber with 12 port accesses, four windows, and eight fan-ports
- Fuel supply system for gaseous fuels (e.g. gas cylinders, control valves, ball control valves, needle valves, gas hoses)
- Eight axial fans including the main control box, cooling fans, computer control panel
- Two pressure transducers (0-150 psi and 0-15 gpsi)
- 3 K-type thermocouples
- A data acquisition system DAQ (NI cDAQ 9172) including several devices and modules (I/O modules and a signal conditioner)
- An ignition system including two tungsten electrodes, a 120 VAC power supply, 10KV DC ignition coil, and high voltage cables
- Schlieren imaging techniques composed of two spherical mirrors, one LED light source, high-speed camera, and a knife edge
- Vacuum pump with high-temperature hose and a needle valve connected to the chamber

B.2 Pre-experimental procedures

B.2.1.1 Computer and DAQ

1. Turn on the control computer
2. Turn on the variable power supply to activate the 5 VCD supply for the high-pressure transducer (0-150 psi) and the 12 VCD for the ignition system`s solid state relay
3. Turn on the NI cDAQ 9172 data acquisition main module. A message should show up on the control computer desktop allowing the access to the LabVIEW software.

B.2.1.2 Ignition system

1. Set up the two spark electrodes to the chamber horizontally through the electrode holders. A gap of 1 mm should be kept between the two electrodes.
2. Make sure the two electrodes are completely insulated from the chamber. This means that the two electrodes should not be in contact or close to any metallic part of the chamber at the flanges or inside the chamber.
3. Make sure the chamber is grounded
4. Connect the electrodes to the ignition coil and then connect the coil to the power supply. Keep the power supply turned off unless for running experiments.
5. Test the spark generation by activating the ignition system from the LabVIEW.

B.2.1.3 Combustion chamber – general check

1. Check the inside of the spherical chamber to ensure that no metallic chips or dirt are left inside. Cleanup and flush the chamber using the high-pressure air supply system.

2. Perform a visual inspection of the quartz windows to verify if they are clean. If not, clean each window by using specific optical cleaning tissues with the aid of Acetone. Use the torque-wrench to mount up the quartz windows by applying up to 85 lb.in torque.
3. Check if all the valves attached to the chamber are closed.

B.2.1.4 Schlieren system

Setup the Schlieren system components as follows:

1) Place the two spherical mirrors each one at 60 inches away from the centre of the spherical chamber opposite to each other in front of the 4.5 inches quartz windows. The two spherical mirrors and the centre of the chamber should be on a straight-line perpendicular to the quartz windows. Both mirrors should be placed at the same altitude by which the centre of each mirror is exactly on the same level of the spherical chamber centre.
2) Place the LED light source and the camera similarly as mentioned above for the spherical mirrors. Both the camera and the LED should be placed opposite to one another in front of the 5 inches quarts windows (on the right side and the left side, respectively, for both the camera and the LED). Maintain 45 inches between the first spherical mirror and the LED light source (45 inches is the focal point of the mirror). All components (the two spherical mirrors, LED light source, and the camera) should be on the same level. Turn on the LED light source power supply and adjust it towards the centre of the first spherical mirror. The light beam reflected from that mirror should be a circle of the same mirror diameter. It should coincide with the circular surface of the second mirror.

3) Connect the high-speed camera as follows: yellow cable at the Sync port, grey cable at the USB port, and the black cable to the power port. Then, turn on the high-speed camera and activate the IDT motion studio software on the control computer.
4) Adjust and align the second mirror towards the centre of the high-speed camera lens. At the focal point, set up the knife edge with a 60% cut-off. The camera should be 5 mm away from the knife. Note that the second mirror centre point, the knife edge, and the centre point of the camera lens all should be on the same straight line and the same level. Once the alignment is done, the IDT motion studio should show a circular light window surrounded by a dark area.

B.2.1.5 Pressure test

1. Close all the valves attached to the chamber.
2. Open the high-pressure air supply main valve
3. Open gradually the needle valve that connects the air supply to the chamber and start reading pressure on the operating desktop of the LABVIEW. Once the pressure reaches 80 psi, close the needle valve.
4. Record the pressure readings every 5 minutes.
5. In the case of no leakage, the pressure readings should be constant. In the case of leakage, the pressure readings will show a decreasing trend. In this case, using a liquid gas-leak detector, check all the 12 access ports on the chamber, the four windows, and the two electrode holders. Leakage is detected when bubbles form on the leaking spot or region.
6. Once leakage is detected, check the sealing of the leaking component. A cleaning process might be needed in some cases.

7. Redo the same steps until leakage is terminated.

B.2.1.6 Axial fans

1. Turn on the cooling fans by turning the red switch at the lower right side of the spherical chamber stand.
2. Turn on the fan control box (turn the selector to the right side).
3. Activate the operation by clicking on the Green Button.
4. Enable servomotors.
5. At the control panel of the LabVIEW user interface, select the Target RPM to the desired fan speed.
6. Click adjust voltage button on the LabVIEW user interface.

B.2.1.7 Vacuum pump check

1. Close all valves attached to the chamber
2. Turn on the vacuum pump.
3. Open the 0-15 psi pressure transducer valve that is connected to the chamber and start reading the pressure on the LabVIEW control panel.
4. Once 5 psi is reached inside the chamber, turn the vacuum pump off.
5. Pressure increase inside the chamber should not exceed 0.08 psi in 40 minutes (This is the reported pressure increase during the vacuum test in this thesis).

B.3. Experimental procedures

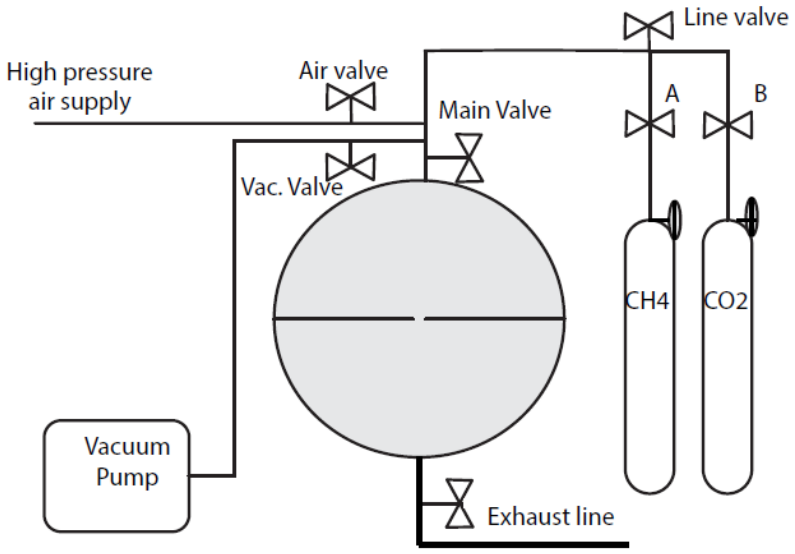

Figure B.1. Fuel supply system

1. Make sure all valves connected to the chamber are closed.
2. Open the main valve and the vacuum valve (Figure B.1) until the pressure inside the chamber reaches 5 psi. Close both the main and the vacuum valves.
3. Open methane cylinder valve then open both valves A (to control CH_4 flow) and the Line valve, then use the main needle valve connected to the chamber to gradually add methane according to its measured partial pressure. After the selected amount is added, close the main needle valve and valve A.
4. Open vacuum valve and vacuum the gas main supply line, and then close the line valve to make sure no residual gas is left in the line.
5. Redo step 3 for CO_2 gas cylinder then redo step 4.

6. Once CO_2 is added and then the gas line is vacuumed, open partially the high-pressure air valve, and then use the main needle valve to add air to the chamber until 14.7 psi is reached. Afterward, close the main needle valve and the air valve. At this stage, the chamber should contain biogas (CH_4 and CO_2) and air mixture according to the desired composition and equivalence ratios.
7. Turn on the axial fans to the desired fan speed and wait 10 minutes until turbulence generated inside the chamber reaches a steady state. Check section B.2.1.6 for more details.
8. Activate the spark ignition system. Check section B.2.1.2 for more details.
9. After flame propagation, turn off the fans and open the exhaust valve.
10. Flush the chamber by opening the air valve and the main needle valve for 10-20 minutes.

Appendix C – Error analysis

C.1 Formulation

The total uncertainty is measured based on two sources: the systematic uncertainty (bias) and random uncertainty (precision). The systematic uncertainty is the error caused by the applied methodology via its components and tools (e.g., high-speed camera, transducers, etc) which hence cannot be estimated by statistic methods. However, the random uncertainty is the error that can be determined by applying statistical methodologies of repeated measurements under the same conditions [105].

The systematic uncertainty (B_{St}) of the turbulent burning velocity is determined based on the following formula [106]:

$$B_{St} = \sqrt{\sum_{i=1}^{N} \left(\frac{\partial S_t(x_i)}{\partial x_i} B_i\right)^2} \quad \text{(C.1)}$$

where Bi is the elemental bias uncertainties generated by each component in the experiment (pressure transducers, thermocouples, Schlieren system), xi is any variable that turbulent burning velocity is dependent upon (pressure, temperature, equivalence ratio) and $\frac{\partial S_t(x_i)}{\partial x_i}$ is the sensitivity of turbulent burning velocity to these variables (p, T, Ø). Table C.1 provides the elemental bias uncertainties (B_i) provided from the datasheets for each instrument used in the methodology.

Similarly, the random uncertainty (P_{St}) is determined based on the following formula [105]:

$$B_{St} = \sqrt{\sum_{i=1}^{N} \left(\frac{\partial S_t(x_i)}{\partial x_i} P_i\right)^2} \quad \text{(C.2)}$$

where P_i is the elemental precision (random) uncertainty yielded by the measurement devices (Table C.1). The precision uncertainty is determined based on the standard deviation (Si) of N measurements (corresponding to v = N-1 degrees of freedom) obtained at the same conditions as: $P_i = \frac{s_i}{\sqrt{N}}$ (C.3)

Device	Elemental source of error	Bias (Bi)	Random (Pi)	Degree of Freedom (v)
Pressure Transducer (0-15 psi)	Combined non-linearity, hysteresis and repeatability	$\mp 0.1\%$		
	Display reading [psi]		0.001036	20
Pressure Transducer (0-150 gpsi)	Combined non-linearity, hysteresis and repeatability	$\mp 2\%$		
	Display reading [psi]		0.532602	20
Thermocouple K-Type	Accuracy [K]	2.2		
	Display reading [K]		0.077064	20
Schlieren system	Optical aberrations - spatial [cm]		0.005015	15
High-speed camera	Resolution [cm/pixel]	0.01197		
Experimental Setup	Experimental repeatability [cm/s]		2.023	4
Fans	Rotational fan speed [RPM]	1%		

Table C.1. Elemental uncertainties contributing to the total uncertainty [50]

The elemental bias uncertainties (B_i) of the pressure transducer and the K-type thermocouple were obtained from the manufacturer's technical data sheet, while for the high-speed camera, the image scale was calculated based on dividing the electrode length in cm by its corresponding length in pixels (cm/pixel). For the fans, a discrepancy of 1% in fan rotational speed (rpm) was determined. Moreover, the elemental random error (Pi) was calculated by a set of N measurements corresponding to the degrees of freedom (v) listed in Table C.1.

Afterward, the total uncertainty measurement is determined by applying the student`s multiplier for 95% confidence and v = 4 degrees of freedom (5 measurements) as follows:

$$(U_{St})_{95} = \sqrt{(B_{St})^2 + (t.P_{St})^2} \quad \text{(C.4)}$$

where t corresponds to 2.132, according to Table 2 of the appendix in reference [106].

However, to apply equations C.1 and C.2, a relationship between the turbulent burning velocity S_t and the variables affecting its measurement is required as follows:

$$S_t = f(\emptyset)\left(\frac{T}{T_0}\right)\left(\frac{P}{P_0}\right)\left(\frac{RPM}{RPM_0}\right) \quad \text{(C.5)}$$

where T and T_0 are the test and room temperatures, P and P_0 are the test and atmospheric pressures, RPM and RPM_0 are the test and the actual fan rotational speed, and Ø is the equivalence ratio of the fuel/air mixture. This relation between the turbulent burning velocity and the equivalence ratio is deducted from the 3rd order curve fits obtained from this study, each for its corresponding experimental conditions and fuel composition. For instance, the relation the turbulent burning velocity of 70% CH_4 biogas composition at 2200 RPM with the equivalence ratio is presented as:

S_t = - 102.32×∅^{3} – 8.0394×∅^{2} + 267.53×∅ - 110.01 (C.6)

Similarly, a relation between the turbulent burning velocity and the flame radius is formulated as:

$$S_t = -0.0002\times r^3 + 0.0245\times r^2 - 0.04629\times r + 45.492 \quad \text{(C.7)}$$

where r is the flame radius. The above equation is used in representing the uncertainty derived from the Schlieren and the high-speed camera errors.

Thus, by combining equation C.6 with the temperature, pressure and RPM parameters, a final formula representing the turbulent burning velocity with the corresponding parameters is expressed as:

$$S_t = [- 102.32\times\emptyset^3 - 8.0394\times\emptyset^2 + 267.53\times\emptyset - 110.01]\left(\frac{T}{T_0}\right)\left(\frac{P}{P_0}\right)\left(\frac{RPM}{RPM_0}\right) \quad \text{(C.8)}$$

C.2 Calculation

After establishing the turbulent burning velocity relation with the experimental parameters, equation C.1 is then applied for each elemental source of error as follows (applying partial derivative):

$$\frac{1}{S_t}\frac{\partial S_t}{\partial \emptyset}B_\emptyset = \frac{306.96\times\emptyset^2 - 16.0788\times\emptyset + 2.6753}{-102.32\times\emptyset^3 - 8.0394\times\emptyset 2 + 267.53\times\emptyset - 110.01}B_\emptyset \quad \text{(C.9)}$$

$$\frac{1}{S_t}\frac{\partial S_t}{\partial \mathrm{T}}B_\mathrm{T} = \frac{1}{T}B_\mathrm{T} \quad \text{(C.10)}$$

$$\frac{1}{S_t}\frac{\partial S_t}{\partial \mathrm{P}}B_\mathrm{P} = \frac{1}{P}B_\mathrm{P} \quad \text{(C.11)}$$

$$\frac{1}{S_t}\frac{\partial S_t}{\partial \mathrm{RPM}} B_{\mathrm{RPM}} = \frac{1}{RPM} B_{\mathrm{RPM}} \quad \text{(C.12)}$$

$$\frac{1}{S_t}\frac{\partial S_t}{\partial \mathrm{r}} B_{\mathrm{r}} = \frac{-0.0006\times r^2+0.049\times r-0.4629}{-0.0002\times r^3+0.0245\times r^2-0.04629\times r+45.492} B_{\mathrm{r}} \quad \text{(C.13)}$$

where $B_{\emptyset}$, B_T, B_p, $B_{RPM,}$ and B_r are the elemental bias uncertainties listed in table C.1

Then, the total bias and random uncertainty are calculated, respectively, as follows:

$$\left(\frac{B_{St}}{St}\right)^2 = \left(\frac{1}{S_t}\frac{\partial S_t}{\partial \emptyset} B_{\emptyset}\right)^2 + \left(\frac{1}{S_t}\frac{\partial S_t}{\partial \mathrm{T}} B_{\mathrm{T}}\right)^2 + \left(\frac{1}{S_t}\frac{\partial S_t}{\partial \mathrm{P}} B_{\mathrm{P}}\right)^2 + \left(\frac{1}{S_t}\frac{\partial S_t}{\partial \mathrm{RPM}} B_{\mathrm{RPM}}\right)^2 + \left(\frac{1}{S_t}\frac{\partial S_t}{\partial \mathrm{r}} B_{\mathrm{r}}\right)^2 \quad \text{(C.14)}$$

$$\left(\frac{P_{St}}{St}\right)^2 = \left(\frac{1}{S_t}\frac{\partial S_t}{\partial \emptyset} P_{\emptyset}\right)^2 + \left(\frac{1}{S_t}\frac{\partial S_t}{\partial \mathrm{T}} P_{\mathrm{T}}\right)^2 + \left(\frac{1}{S_t}\frac{\partial S_t}{\partial \mathrm{P}} P_{\mathrm{P}}\right)^2 + \left(\frac{1}{S_t}\frac{\partial S_t}{\partial \mathrm{RPM}} P_{\mathrm{RPM}}\right)^2 + \left(\frac{1}{S_t}\frac{\partial S_t}{\partial \mathrm{r}} P_{\mathrm{r}}\right)^2 \quad \text{(C.15)}$$

where $P_{\emptyset}$, P_T, P_p, P_{RPM} and P_r are the elemental uncertainties listed in table C.1.

As an illustrative example, both the bias and elemental random uncertainties are calculated at stoichiometric equivalence ratio $\emptyset = 1.0$ for 70% CH4 Biogas, 2200 RPM, room temperature (298 K) and atmospheric pressure (101.325 kpa). The measured turbulent burning velocity, St, under these conditions is 44.4 cm/s, while the radius, r, is taken at 3.5 cm. The bias and elemental random uncertainty equations are presented, respectively, as follows:

$$\frac{B_{St}}{St} = \sqrt{\left(\frac{293.55}{47.16}\times 0.001\right)^2 + \left(\frac{1}{298}\times 2.2\right)^2 + \left(\frac{1}{101.325}\times 0.02\right)^2 + \left(\frac{1}{2200}\times 22\right)^2 + \left(\frac{-0.298}{46.62}\times 0.01197\right)^2}$$

$$B_{St} = 0.6173\ cm/s$$

$$\frac{P_{St}}{St} = \sqrt{\left(\frac{293.55}{47.16}\times 0.001036\right)^2 + \left(\frac{1}{298}\times 0.077064\right)^2 + \left(\frac{1}{101.325}\times 0.5326\right)^2 + \left(\frac{-0.298}{46.62}\times 2.023\right)^2}$$

$$P_{St} = 0.3696\ cm/s$$

Then, by applying equation C.4 at 95% confidence, the total uncertainty of the measured turbulent burning velocity is:

$$(U_{St})_{95\%} = \sqrt{(0.6173)^2 + (2.132 \times 0.3696)^2} = 1.0009\ cm/s$$

Table C.2 shows the error calculations for 70% CH4 Biogas at turbulence intensity of 1.0 m/s and under room temperature (298K) and atmospheric pressure (101.325 Kpa) for a wide range of equivalence ratios.

Ø	B_{St} [cm/s]	P_{St} [cm/s]	U_{St} [cm/s]	St [cm/s]	Error %
0.6	0.2982	0.1536	0.4428	22.8	1.9423
0.8	0.5590	0.2869	0.8287	42.8	1.93
1.0	0.6173	0.3696	1.0009	44.4	2.2544
1.1	0.5648	0.3992	1.0215	36.39	2.8071
1.2	0.2609	0.2335	0.5620	11.579	4.8537
Average error %					**2.74**

Table C.2. Total uncertainty of 70% CH_4 Biogas turbulent burning velocity at turbulence intensity of 1.0 m/s, 298 K, and 101.325 Kpa.

Appendix D - Density ratio

Turbulent burning velocity measurement is highly dependent on the density ratio of the burned to unburned gases ($\frac{\rho_b}{\rho_u}$) as shown in the following turbulent burning velocity equation (section 2.4.2):

$$S_t = \left(\frac{1}{1.11}\right)\frac{\rho_b}{\rho_u}\frac{dR_{Sch}}{dt} \tag{2.10}$$

Thus, due to this linear relation between the density ratio and the burning velocity, lower density ratios lead to obtaining slower burning speeds while vice versa for higher density ratios. Therefore, an inaccurate measurement of the density ratio can result in significant discrepancies in the obtained turbulent burning velocities.

In the literature, the density ratio is obtained by applying the conservation of mass equation resulting in the following formula [65]:

$$\frac{\rho_b}{\rho_u} = \frac{n_u T_u}{n_b T_b} \tag{D.1}$$

Where n_u, n_b = mole numbers of reactants (unburned) and products (burned), T_u, T_b = initial and adiabatic flame temperatures. Thus, to obtain the adiabatic flame temperature, many thermodynamic equilibrium programs are used in the literature such as HPFLAME, GASEQ and CHEMKIN-PRO [39,66,98,99]. In this thesis, GASEQ software [107] is adopted (Appendix F). Results are shown in Figure D.1.

The difference in the density ratios between the three biogas compositions is not much significant over most of the equivalence ratios except for the rich conditions. Moreover, the smallest values are mainly located around the stoichiometric compositions, while the largest ones are pronounced by the lean mixtures than by the rich. These high values are due to the small amounts of fuel at lean mixtures which hence decrease the reactants density. However, although the large quantities of fuels at rich mixtures increase the reactants density, the produced burned gas exhibits an increase in the burned gas density as well, hence leading to a modest increase in the density ratio. Nevertheless, the density ratio of the three biogas compositions follows the same trend.

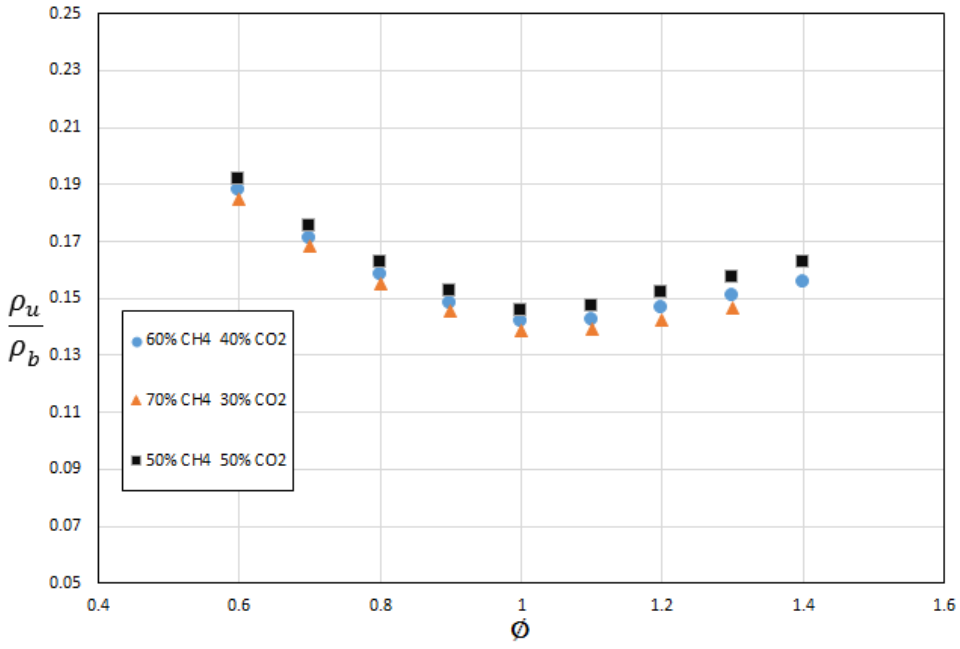

Figure D.1. Density ratio of Biogas compositions for a wide range of equivalence ratios

Appendix E – Spark electrode insulation

Figure E.1 shows the assembly of the spark electrode insulation. The main body is made from Nylon material (Part 5), while the hollow tube that holds in the spark electrode is made from Teflon (Part 3). Both materials have high dielectric resistance to insulate the 10 KV DC high-voltage signal from leaking into the spherical chamber.

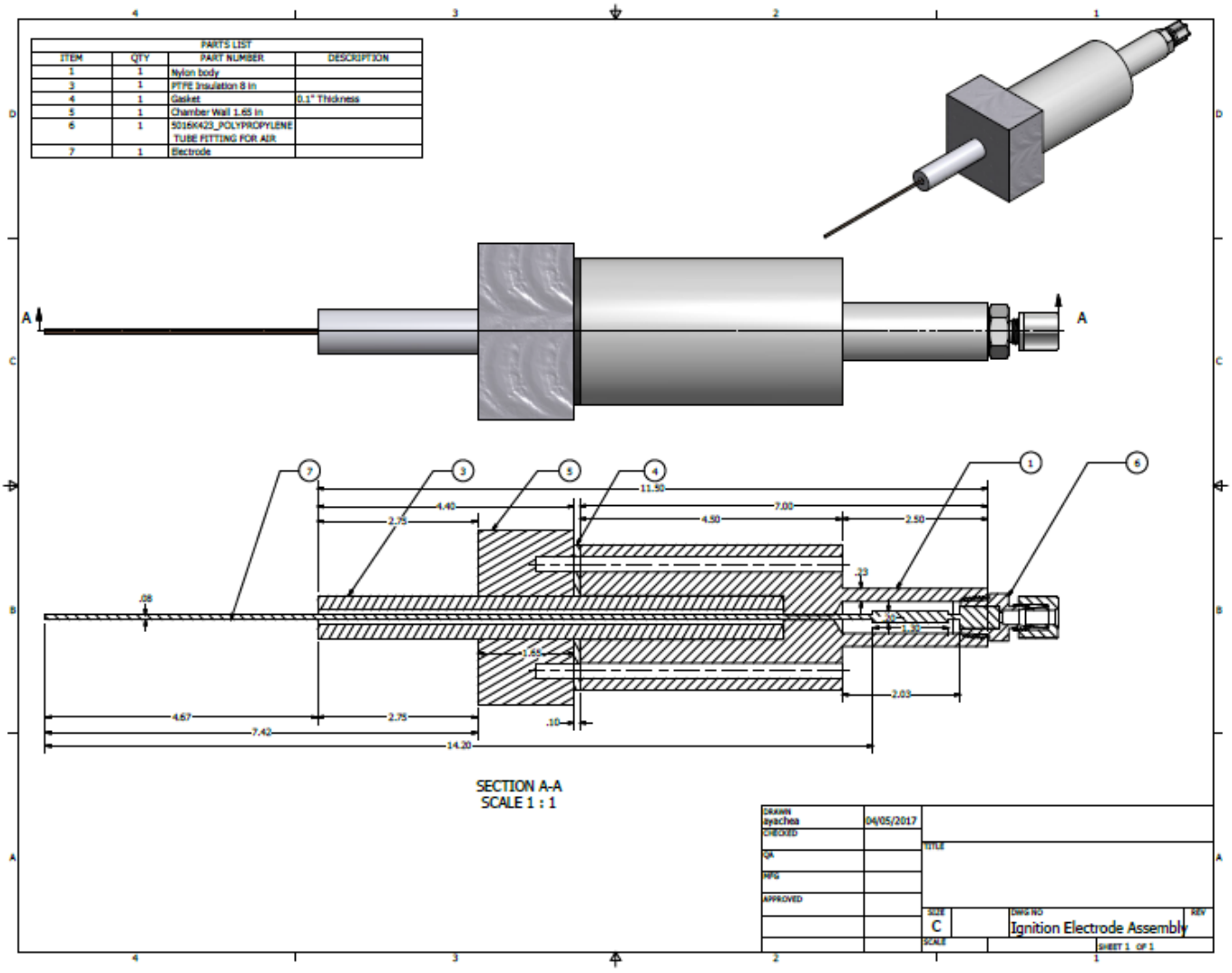

Figure E.1. Spark electrode insulation assembly

Appendix F – Gaseq Chemical Equilibrium Software

Gaseq is a chemical equilibrium program for windows established by Chris Morely [107]. It can calculate all chemical parameters of both the reactants and products such as adiabatic flame temperature, density, molecular weight, viscosity, etc. Figure F.1 shows a screenshot example of the Gaseq interface. Input can include equivalence ratio, reactants number of moles, temperature, and pressure.

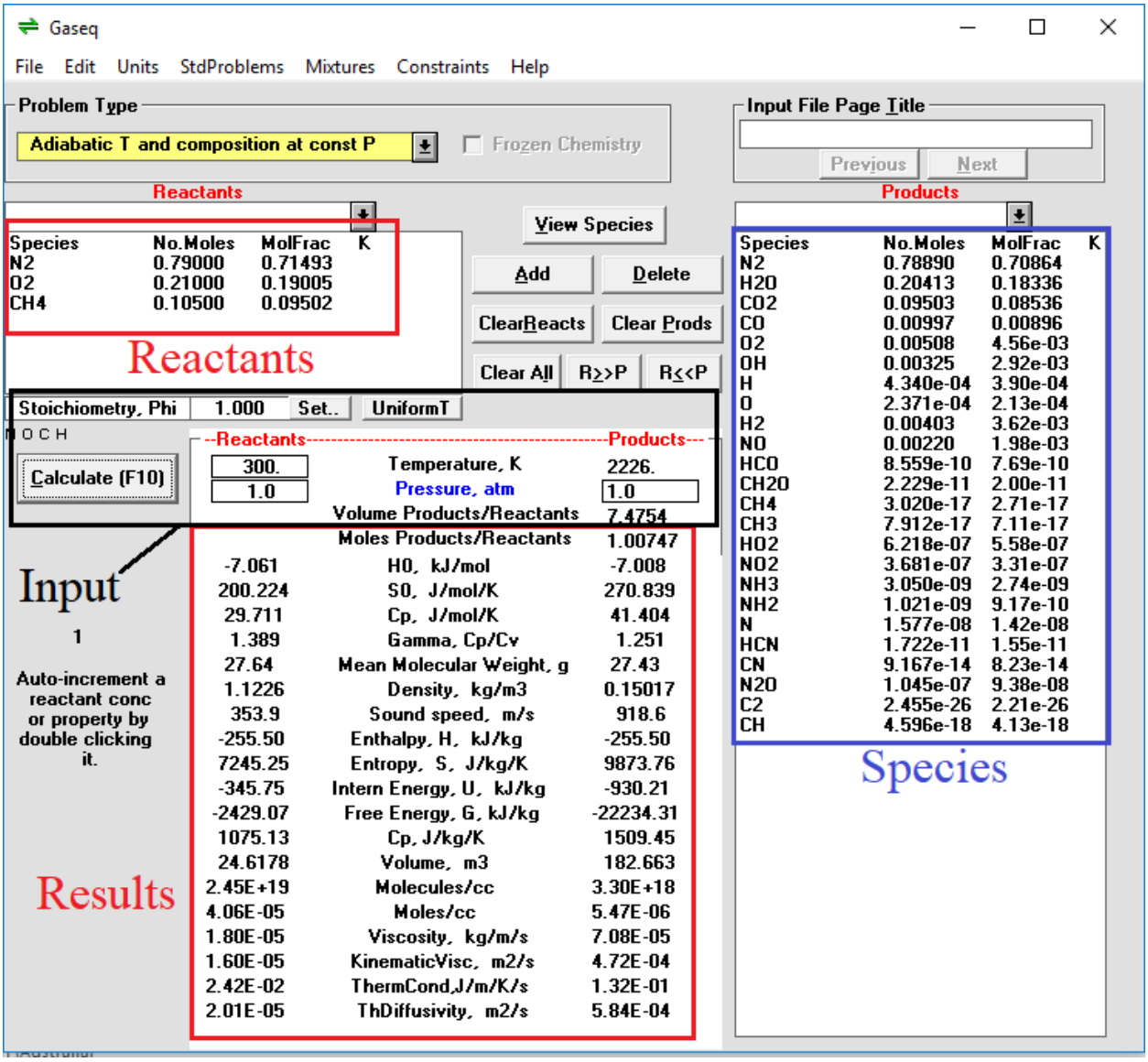

Figure F.1. Screenshot example of Gaseq interface showing reactants, species, input and results.